A Recovery Curve Based Method for Calculation of the Matrix-Fracture Mass Transfer in Naturally Fractured Petroleum Reservoirs

A DISSERTATION
SUBMITTED TO THE
CHAIR OF PETROLEUM AND GEOTHERMAL ENERGY RECOVERY
AND THE COMMITTEE ON GRADUATE STUDIES OF THE
UNIVERSITY OF LEOBEN, AUSTRIA,
IN PARTIAL FULLFILLMENT OF THE REQUIREMENTS FOR THE DEGREE OF
"DOKTOR DER MONTANISTISCHEN WISSENSCHAFTEN"

written by
Dipl.-Ing. Dipl.-Ing. Christoph Steiner
December 2017

Advisor: O.Univ.Prof. Dipl.-Ing. Dr.mont. Dr.h.c. Zoltán E. HEINEMANN

Affidavit

I declare in lieu of oath, that I wrote this work and performed the associated research myself, using only literature cited in this volume.

_____

Dipl.-Ing. Dipl.-Ing. Christoph Steiner
Leoben, 14. December 2017

Acknowledgments

First of all, I would like to thank O.Univ.-Prof. Dipl.-Ing. Dr.mont. Dr.h.c. Zoltán E. Heinemann for his advice and support throughout this work. Without his ideas and encouragement this work would have not been possible.

I also want to thank Univ.-Prof. Dipl.-Ing. Dr.mont. Herbert Hofstätter for his suggestions that vastly improved the quality of this thesis.

Special thanks also to Dr. Georg Mittermeir of Heinemann Consulting GmbH Leoben who not only supported me in the development of this work but also taught me invaluable reservoir engineering skills.

I also want to thank Professors Heinemann's Doctorate Group (PHDG), which provided generous scholarships and PHDG's proprietary software package H5, which was essential to the success of this dissertation.

I also want to express my gratitude to Dr. Pavle Matijevic Technologie und Forschungsimpulszentrum GmbH and PM Lucas Enterprises for providing office room and all necessary software packages.

Last but not least I want to thank my parents and my partner Lisa Bindhofer for their comprehensive support and encouragement throughout this work.

Abstract

This dissertations presents a method for the calculation of the matrix-fracture mass transfer in naturally fractured petroleum reservoirs based on the recovery curve concept, which was first introduced by Heinemann in 2004. This work extends previous efforts of research and development of Prof. Heinemann's research group by successfully defining practically usable techniques for scaling recovery curves and thereby improving the recovery curve method. Clear evidence for the correctness of this method is presented in this dissertation. The applicability of other transfer models is also assessed and demonstrated utilizing numerical experiments.

In 1960 Barenblatt, Zheltov and Kochina introduced the dual continuum concept and applied it to fractured reservoirs. In this concept a transfer term describes the interaction between the matrix and the fracture continuum. One of the most used and accepted methods for defining this transfer term is the transfer function introduced by Kazemi et al. in 1976. Using fine grid single matrix block calculations, the applicability of this type of transfer equation using shape factors is tested. It is evident that it is applicable in certain cases like single phase expansion, but not generally. Other concepts like Multiple Interacting Continua or Discrete Fracture Networks have been developed, but do not have industrial significance and are therefore not part of the investigations.

Following the principle of the recovery curve concept, numerically derived recovery curves are directly utilized for determining the matrix-fracture mass transfer, instead of matching fitting parameters of equations to the results of single matrix block calculation. It is proved that it is possible to utilize a single recovery curve, calculated at bubble point pressure, for all possible matrix pressure and saturation conditions by scaling it. The therefore required scaling consists of two parts, one for the recovery factor increment and the other for the ultimate oil recovery of the single matrix block. The significance of the presented scaling method is demonstrated on both small and large scale models. It is shown that for accurate and reliable results both scaling of the recovery curve increment as well as the ultimate recovery is necessary.

Kurzfassung

In dieser Dissertation wird eine Methode zur Berechnung des Matrix-Kluft Massenaustausches für geklüftete Kohlenwasserstofflagerstätten basierend auf der von Heinemann 2004 eingeführten Entölungskurvenmethode vorgestellt. Diese Arbeit führt vergangene Anstrengungen im Bereich der Forschung und Entwicklung von Prof. Heinemann's Forschungsgruppe weiter, indem praktisch anwendbare Techniken zum Skalieren der Entölungskurven zur Verbesserung der Entölungskurvenmethode definiert werden. Klare Beweise für die Richtigkeit der Methode werden in dieser Dissertation präsentiert. Die Anwendbarkeit anderer Massenaustauschmodelle wird diskutiert und anhand numerischer Experimente gezeigt.

1960 wurde von Barenblatt, Zheltov und Kochina das Dual-Kontinuum Konzept eingeführt und für geklüftete Lagerstätten eingesetzt. In diesem Konzept beschreibt ein Austauschterm die Interaktion zwischen dem Matrix und Kluft Kontinuum. Eine der meistverwendeten und akzeptierten Methoden um diesen Austauschterm zu bestimmen ist die Austauschfunktion, die von Kazemi et al. in 1976 eingeführt wurde. Mittels feingittrigen Einzelmatrixblockrechnungen wurde die Anwendbarkeit von diesem Typ von Austauschfunktion getestet. Es ist bewiesen, dass diese nur in bestimmten Fällen wie der Einphasenexpansion anwendbar ist, jedoch nicht allgemein. Andere Konzepte wie die Multiplen Interagierenden Kontinua oder Diskrete Kluftnetzwerke wurden entwickelt, aber sie haben bis heute keine Relevanz in der Industrie und sind deshalb auch nicht Teil der Untersuchungen.

Dem Prinzip der Entölungskurvenmethode folgend werden numerisch kalkulierte Entölungskurven direkt zur Bestimmung des Matrix-Kluft Massenaustausches verwendet, anstatt Parameter von Funktionen an das Ergebnis von numerischen Einzelmatrixblockkalkulationen anzupassen. Es ist bewiesen, dass es möglich ist eine einzelne Entölungskurve, berechnet am Blasendruckpunkt, für all möglichen Matrix Druck- und Sättigungszustände anzuwenden. Die dafür notwendige Skalierung besteht aus zwei Teilen, einem Teil für die Zuwachsrate des Entölungsgrades und einem anderen Teil für den Endpunkt der Entölungskurve eines Einzelmatrixblocks. Die Signifikanz der präsentierten Skalierungsmethode ist gezeigt an Modellen im kleinen und auch großen Maßstab. Es ist gezeigt, dass für akkurate und zuverlässige Ergebnisse sowohl das Skalieren der Zuwachsrate des Entölungsgrades als auch das Skalieren des Endpunktes der Entölungskurve notwendig ist.

Table of Contents

Chapter 4

Chapter 5

Chapter 6

List of Figures

List of Tables

Chapter 1

Introduction

1.1 Motivation of Work

1.1.1 Background

Naturally fractured reservoirs (NFRs) contain a significant amount of the world's oil and gas resources. They are highly complex due to the matrix-fracture interaction and to date the industry was not able to solve the issue of modeling them satisfactorily. The most challenging aspect regarding NFRs is describing the matrix-fracture fluid transfer. Heinemann (2004) introduced "The Recovery Curve Method" (RCM) to numerical reservoir modelling, providing a new approach for calculating this transfer. In this concept the fluid transfer between the fracture and matrix is determined utilizing numerically derived recovery curves (RC). The concept has then been applied to the dynamic modeling of NFRs and was topic of dissertations, master thesis and scientific papers. The RCM concept was later utilized for the development of a dual porosity material balance method by Mittermeir (2015). Gharsalla (2015) applied this method to a two-phase NFR. It was the first material balance calculation correctly considering the interaction between matrix and fracture.

1.1.2 Objectives

The objective of this work is to make the RCM approach generally applicable for the dynamic modelling of NFRs and to demonstrate, to the best knowledge of the author, its superiority over all previously applied solutions. This requires scaling of a RC, which was derived at constant pressure conditions, to the actual state of the matrix block in the numerical model and a correct determination of the mass transfer rates based on the scaled RC.

1.1.3 Relevance

A significant part of the world's oil resources is in NFRs. For determining the reserves, reservoir engineers have to develop a depletion plan, considering well placement, flow regimes, etc., leading to an estimate for the expected ultimate recovery. This estimate also considers parameters impacting the ultimate recovery that cannot be influenced, as they are given by nature (rock properties, fluid types, etc.) or by the surrounding world (oil price, taxes, etc.).

One of the most effective approaches for optimizing the development strategy and thereby maximizing the depletion and associated ultimate recovery, is deploying numerical reservoir simulation. NFRs are modeled by splitting them into two separate domains, matrix and fracture. In dynamic modeling this distinction is represented by utilizing dual porosity models, containing both a matrix and a fracture continuum. These continua are linked by a transfer term. Many attempts to model the mass transfer between the continua have failed or were only partially successful and led to significant overestimations of reserves and non-optimized project value. It is critical to realistically model the depletion of individual SMBs by an appropriate transfer term for obtaining justifiable results for the ultimate recovery factor. If already the ultimate recovery of the SMBs within the reservoir is wrong, then the one for the entire reservoir will reflect this error.

Therefore, an assessment of the available methods for determining the matrix-fracture mass transfer is necessary. It is already widely published that the RCM, utilizing the results SMB calculations, provides the most appropriate method for modeling the transfer term. To further improve this method, a scaling of the RC's has proven to be necessary and is presented in this work.

1.2 The Approach

1.2.1 Working Environment

The author was supported by Professor Heinemann's Doctorate Group (PHDG) and by the Chair of Petroleum and Geothermal Energy Recovery of the University of Leoben. In compliance with the rules of the PHDG, members do not claim "property right" for texts displaying the general understanding and knowledge within the group. In this thesis, these texts are inside ⟨ and ⟩ and are not claimed to be originally drafted by the author. Using these texts without adaptations is allowed and encouraged. Some of the sentences will be identical to ones written before, others will be changed to improve it. The author of this thesis does not claim to be the original creator of the concerned text parts and encourages others to use the written formulations.

⟨ The author wishes to state that he would not have been able to conduct and complete this complex research and development work entirely by himself. Although this dissertation has

been written by the author alone, it is the result of a close cooperation within PHDG, which has accumulated know-how, documentation, case studies and software tools on reservoir characterization and analysis. Members of this group include theoreticians, numerical analysts, computer experts and practicing reservoir engineers.

No author claims ownership for any produced written texts that are written within the working environment of the group. It is encouraged to use existing formulations, also for individuals outside of PHDG.

As a principle, all team members can use the collective knowledge of the group. Available formulations are not reformulated but used unchanged in subsequent documents, publications and in theses unless improvements in clarity and use of English can be achieved. The author of this dissertation makes use of the group's common knowledge, especially that which has not yet been published but only documented in internal reports, master's theses and PhD dissertations of former group members. All of these are referenced in general, but not attributed in every instance.

During this research, the author had access to proprietary information. Sources of such information are not referenced unless written permission, including the right of publication, has been provided by the source.

In order to clearly separate collegial contributions from the individual work of the author, the author's scientific ideas, achievements and his additions to future technology are explicitly indicated at the end of this chapter.)

1.2.2 Previous Related Works

The following works, which are originating from the PHDG, are listed thematically, instead of chronologically.

(Heinemann (2004) suggested in that instead of trying to estimate individual rock and fluid properties, the RCs should be determined and used directly in a numerical reservoir simulation model. The dimensionless RCs display the recovery factor as function of dimensionless time.

Heinemann and Mittermeir (2012) derived a general formulation of the Kazemi, Gilman and Elsharkawy (1993) shape factor, considering permeability anisotropies and all possible irregular matrix block shapes.

Pirker (2008) presented a more efficient numerical methods for calculating RCs for SMBs. She accounted for the fact that matrix blocks are not uniform and therefore RCs have to be calculated for classes of blocks. Subsequently, the individual RCs had to be consolidated by averaging according to the frequency of each class. The averaged curve was then assigned to a simulation cell.

Amiry (2014) suggested a method based on statistical analysis of matrix blocks in outcrops of

fractured formations. He showed that the RC was not influenced by the actual shapes of blocks and could be scalable with respect to the shape factor and apparent permeability. Additionally, he showed that under the same conditions, the results of the RCM and those of the classical conventional method were similar and the two approaches could be combined both in space and time.

Heinemann and Mittermeir (2016) published their approach for a numerical implementation of the RCM. It is based on the premise that from the recovery curve fracture-to-matrix injection rates will be calculated. Expansion of the fluids in the matrix is then handled with the conventional transfer function.

Ghaedi et al. (2014, 2015) investigated a possible application of recovery curves by determining the curves directly from historical production data. Based on the findings of the history matching fundamental rock properties such as wettability, capillary pressure and relative permeability functions are determined.

Mittermeir (2015) presented the first dual porosity material balance method that fully accounts for the matrix-fracture interaction by using recovery curves to determine the mass transfer between matrix and fracture. It fully accounts for expansion, capillary and gravitational driving forces, as they are already considered in the numerically derived recovery curves.

Gharsalla (2015) presented the first successful material balance application to a realistic dual porosity two-phase reservoir. The oil-water contact has been matched by adjusting the recovery curve for oil displacement by water.)

1.2.3 Utilitarianism

(Utilitarianism is one of the basic principles of the PHDG. The actual research and development was conducted in close connection with real field projects. The new developments are used in parallel with standard methods, whereas new ideas can be discarded if they do not satisfy the expectations of quality and efficiency, within the time constraints of the project. This dualism provides the possibility of close control and will quickly reveal if the standard method is not the best in each step.)

1.3 Software Tools

(The simulation software H5 is an alternative to other commercial simulators such as ECLIPSE. It is a proprietary software system developed by Professor Zoltan Heinemann and associates and is the fifth generation of research simulators developed under the supervision of Prof. Heinemann. The first generation was written in FORTRAN-IV in 1968. The development of the fifth generation began in 2006, using FORTRAN-1995 and C++ programing languages. The various "H"-versions served as the foundations for commercial software packages including

SIMULA, SURE, PRS-2012 and PRS-2015. Prior to version H4, the simulators were used as teaching and research tools at the Montanuniversität Leoben.

PhD candidates sponsored by PHDG have access to the H5 source code so they can experiment with the existing modules and can design and implement new procedures. Student researchers cannot make unsupervised modifications to the H5 code but can develop standalone modules or simply present detailed descriptions of suggested improvements and extensions to be implemented by professional programmers. Testing and benchmarking is the responsibility of the project author. H5 can operate on ECLIPSE input without any modifications, so identical runs can be made on ECLIPSE, H5 and PRS. These runs can be started in parallel and the results must either be close to each other or the differences must be explainable.

The author has greatly benefited from the H5 software and PHDG technical support which provided the opportunity to develop and test new concepts and procedures for reservoir simulation.)

1.4 Outline

Chapter 1 **Introduction**

This is the current chapter which contains a brief introduction to the objectives and contents of this dissertation. The scientific and technical achievements of the author are stated.

Chapter 2 **State of the Art of Modeling Naturally Fractured Reservoirs**

An overview over the dynamic modeling approaches for fractured reservoirs is given. This includes the dual continuum, the multiple interacting continua and the discrete fracture modeling approach for numerical models. Also current dual porosity material balance will be mentioned.

Chapter 3 **Matrix-Fracture Mass Transfer Concepts in Dual Continuum Models**

Three main types of transfer models are discussed: the analytical recovery curve approach, the transfer-equation and the RCM.

Chapter 4 **Verification of Mass Transfer Equations**

In this chapter a set of numerical SMB experiments is used to test dual continuum transfer models.

Chapter 5 **The Recovery Curve Method**

The principles of the approach are discussed and a method for applying recovery curves calculated at two-phase constant pressure conditions to a general case are discussed. The necessary scaling of RCs is described.

Chapter 6 **Verification of the Recovery Curve Method**

A column model with discretized SMBs is used for verifying the presented approach for the scaling of the recovery curves. The results will also be compared to the Kazemi et al. (1976) transfer function results.

Chapter 7 **Full Field Application**

A full field model with a realistic production scenario serves as a basis for three distinct numerical models, which differ in the matrix-fracture mass transfer model. The first utilizes the RCM with scaling, the second without scaling and the third the Kazemi et al. (1976) transfer equation. The results and the impact of the matrix-fracture transfer model on the production scenario are presented.

Chapter8 **Conclusions**

1.5 Scientific Achievements and Technical Contributions of the Author

1.5.1 Original Ideas Presented

- The author proposes a scaling of the RCs, which are determined at bubble point pressure, and then utilized as input for the RCM. Both speed and ultimate value of matrix oil recovery can be described as a function of the pressure and the individual pressure history of the matrix blocks.

- The author suggests to utilize numerical SMB models, operated at various pressure conditions, for determining scaling factors that can accurately correct the ultimate recovery to all pressure values.

1.5.2 Scientific Achievements

- The author's investigations on numerical SMB models gave clear evidence that the transfer equation after Kazemi et al. (1976) is applicable for single phase expansion and solutio-gas-drive only.

- The same SMB investigations also demonstrated that the mass transfer concept after Reiss et al. (1973) is not generally applicable, as it cannot account for changing drive mechanisms, pressure changes, etc.

- The author showed that it is possible to scale recovery curves, which are numerically derived at constant pressure conditions, to changing and different pressures. This is shown on a dual porosity column model where the results of the RCM based calculations are compared to results where the matrix is finely gridded.

- The author's investigations on the dual porosity column model proved that the correction of the recovery curves can be split into a scaling of the increment and one of the ultimate recovery value.

- The author derived an approach for the matrix-fracture mass transfer rates based on the Heinemann & Mittermeir approach also for non-uniform saturation conditions in the fracture based on theoretical considerations.

1.5.3 Technical Contributions

- The possibility of implementing the RCM including the scaling options into a multi-purpose reservoir simulator was proved.
- The author demonstrated a workflow for finding the recovery curve scaling factors, which is applicable to water and gas displacement of oil.

1.6 Publications of the Author

Steiner, C. and Mittermeir, G.M. 2017. Applicability of the shape-factor concept for naturally fractured reservoirs and an alternative approach. *Journal of Petroleum Science and Engineering* **154**: 60-75. https://doi.org/10.1016/j.petrol.2017.04.009

Mittermeir, G.M., Steiner, C., Gharsalla, M.M. and Heinemann, Z.E. 2016. Verification of Geological Models With One Single Simulation Run. Paper presented at the SPE Europec/EAGE Conference and Exhibition, Vienna, Austria, 30 May - 2 June 2016. SPE-180122-MS

In preparation:

Brand, J., Steiner, C. and Mittermeir, G.M. Naturally fractured reservoirs (NFR) recovery factors and development planning - A case study comparison of the Recovery Curve Method (RCM) and current industry practice. Paper prepared for the SPE Annual Technical Conference & Exhibition, to be held 24 - 26 September 2018, Dallas, Texas, USA.

Steiner, C. and Heinemann, Z.E. An Improved Recovery Curve Method for Modeling Naturally Fractured Reservoirs. Paper prepared for submission at the *SPE Journal*.

Chapter 2

State of the Art of Modeling Naturally Fractured Reservoirs

In this chapter current methods and practices for modeling NFRs are discussed. As all industry relevant approaches and also this work are based on the dual continuum modeling (DCM) approach, the focus of this chapter will be set on these methods. Discrete fracture modeling (DFM) will be mentioned only briefly, as no industry relevant application is known and it has no intersection with this work. Additionally, recent advances in the material balance calculation for NFRs will be discussed.

2.1 Characterization and Classification of Naturally Fractured Reservoirs

To design an appropriate development plan utilizing a dynamic reservoir model, one needs a credible reservoir description that includes fracture related properties such as (Heinemann and Mittermeir 2014):

- Size of the fractures,
- Number of fractures per length (called fracture count),
- Fracture orientation,
- Fracture aperture,
- Fracture porosity,
- Conductivity,
- Fracture connectivity,
- Fracture relative permeabilities.

For a full description of the reservoir also matrix properties have to be estimated. It should be noted that although some properties like porosity can be determined accurately, they are only known for an extremely small part of the reservoir. This measured data is then used in some form (stochastic modeling, kriging, interpolation, etc.) for estimating the properties throughout the reservoir. Creating an initial model, that encompasses well founded matrix and fracture

properties, is a crucial task in modeling NFRs. However, it is not in the scope of this work and will therefore not be discussed in more detail. One of the basic assumptions of this work is that there is already a possibility to find a reasonable starting point for matrix and fracture properties.

Based on the storage capacity and permeability ratio, NFRs can be classified. Nelson (1992) gave a classification based on both porosity and permeability (Figure 2.1), where four types are distinguished. Type I is a reservoir where both fluid flow and storage capacity is predominantly in the fracture and the matrix contribution is only minor. In type II the flow is also dominated by fracture flow with low matrix permeability, but the matrix also stores parts of the oil. Type III and type IV both have most of the storage capacity in the matrix. In type III the permeability is still largely in the fractures, whereas in type IV also the total permeability is matrix dominated.

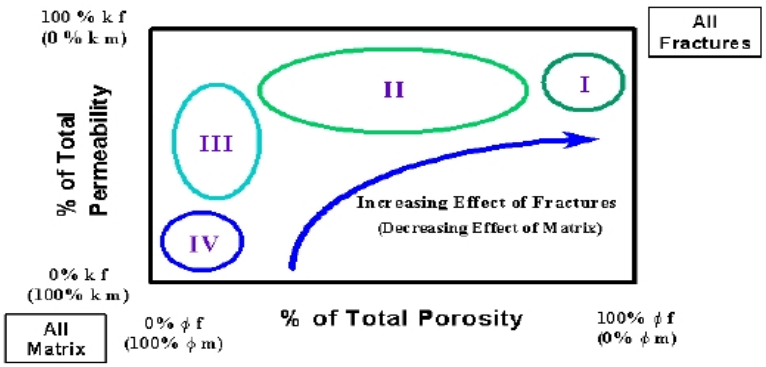

Figure 2.1: Classification of fractured reservoirs after Nelson (1992)

Another widely used classification is the one by Aguilera (1980), who defined three types of NFRs based on the ratio of storage capacity between matrix and fracture (Figure 2.2). Type A NFRs store most of the oil in the matrix, in type B neither matrix or fracture are dominant and in type C the oil is stored only in the fracture.

.

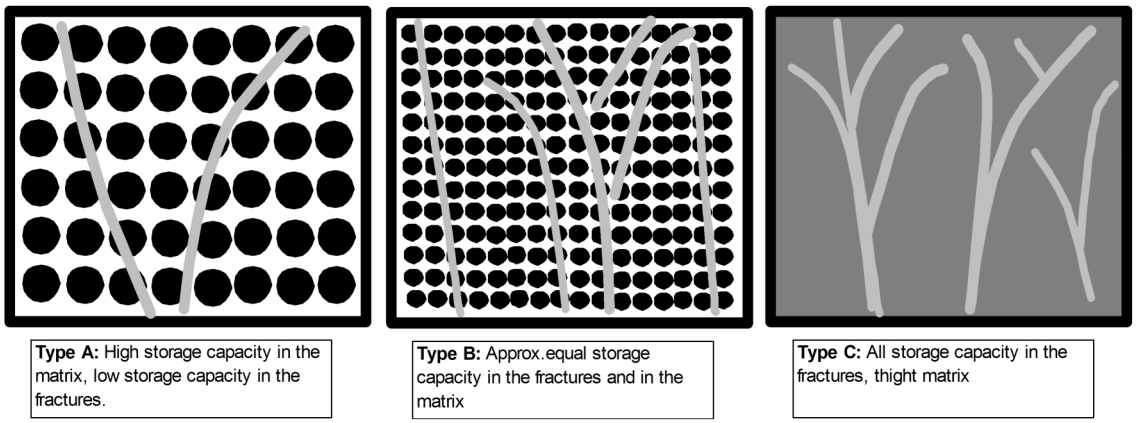

Figure 2.2: Classification of fractured reservoirs after Aguilera (1980) based on porosity distribution (McNaughton and Garb 1975)

2.2 Recovery Processes in Fractured Reservoirs

Oil recovery from NFRs is based on the same physical principles as in non-fractured reservoirs, namely (Heinemann and Mittermeir 2014):

1. Rock compressibility and compaction,
2. Single phase fluid expansion,
3. Solution gas drive,
4. Gravity drainage,
5. Capillary Imbibition,
6. Diffusion,
7. Viscous displacement.

However, there are significant differences in the exploitation of oil from fractured compared to non-fractured reservoirs. In most NFRs the matrix contains the majority of the oil and the fractures provide the main fluid flow pathways through the reservoir due to their much higher permeability. The described reservoir would be of type A according to Aguilera (1980) and of type II or III according to Nelson (1992). To produce the oil from the reservoir through wells, which drain from the highly permeable fractures, a fluid transfer between matrix and fracture must occur. The efficiency of this transfer process determines the recoverable oil and the production capacity.

The recovery processes 1-3 are purely pressure dependent, as transient effects can be neglected in nearly all instances. As the pressure in the fractures drops, the fluid in the matrix expands and flows out. When this happens in a saturated system, also solution gas liberates and expands.

Gravity drainage (4) is a mostly dependent on the saturation in the fracture. However, especially in the case of gas filled fractures, this driving force is also pressure dependent. This is because the compressibility of the gas in the fracture and the oil in the matrix is different, resulting in changing differences between the gravitational gradients.

(5) only depends on the saturation in the fracture and can therefore be seen as a purely time-dependent process.

(6) acts on light hydrocarbon components and can be considered only in a compositional formulation. Fluid flow in the fracture results in a pressure gradient along the matrix block, resulting in (7).

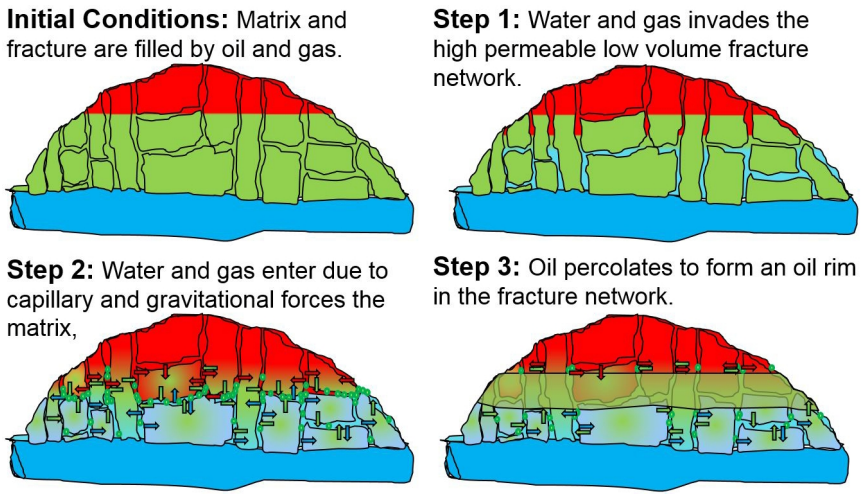

Figure 2.3: Recovery process in a dual porosity / dual permeability three phase reservoir (Heinemann and Mittermeir (2014))

Figure 2.3 is an illustration of the oil recovery process from a NFR. Initially, both the matrix and fracture are oil filled between the initial oil-water contact (OWC) and the initial oil-gas contact (OGC). When production starts, oil is removed from the fracture network and the equilibrium between matrix and fracture is disturbed. As pressure in the system drops, solution gas is liberated and the OGC moves downward. Water influx from the aquifer causes an upward movement of the OWC. As saturation and pressure in the fracture change, the resulting driving forces (expansion, capillary and gravitational forces) cause the displacing phase, gas or water, to enter the matrix and oil is expelled from it. The expelled oil forms an oil rim in the fracture domain, resulting in a possible oil resaturation of matrix regions that have previously been swept by water or gas.

2.3 The Dual Continuum Concept

The dual continuum approach is a mathematical concept which is widely used for modeling NFRs, where both matrix and fracture store oil and interact. In a NFR, where there is no interaction between matrix and fracture (e.g. tight matrix), this concept is not applied and these reservoirs can be regarded as single porosity reservoirs for the purpose of reservoir simulation.

Dual continuum models (DCMs) have been introduced into reservoir simulation by Barenblatt, Zheltov and Kochina (1960) and Warren and Root (1963). The basic concept is that two separate continua, fracture and matrix, are interacting. In the original dual continuum concept only the fracture cells are connected with each other and have one adjacent matrix cell. The matrix cells cannot communicate with each other (Figure 2.4).

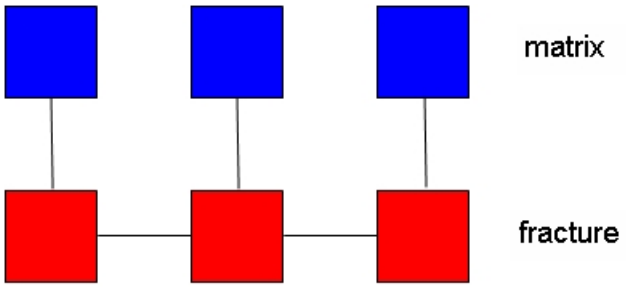

Figure 2.4: Dual porosity (single permeability) concept, only the fractures are continuous

Pseudo-steady state conditions are assumed for the mass transfer between fracture and matrix and only single-phase flow was considered. The transfer between fracture and matrix was calculated on equations of the form:

$$q_p^{mf} = \sigma \frac{\rho k}{\mu}(p_m - p_f), \tag{2.1}$$

where q is the mass transfer rate between fracture and matrix, σ is a constant shape factor, ρ is the fluid density, μ is the fluid viscosity, k is the permeability and p the pressure. The indices p denote the phase, m the matrix and f the fracture. With this transfer term the equation of mass conservation for two immiscible and compressible fluids can be written for the fracture continuum:

$$\nabla(\rho \vec{u})_{fp} - q_p^{mf} = -\frac{\partial}{\partial t}(\phi_f S_{fp} \rho_{fp}), \tag{2.2}$$

and for the matrix continuum:

$$\nabla(\rho \vec{u})_{mp} + q_p^{mf} = -\frac{\partial}{\partial t}(\phi_m S_{mp} \rho_{mp}), \tag{2.3}$$

where $\vec{u}$ is the filtration velocity, ϕ is the porosity and S is the saturation.

Kazemi et al. (1976) extended this to provide the original multiphase DCM leading to a transfer function for component *c* and a matrix cell volume *V*, considering the phase potential Φ:

$$q_{cmf} = V\sigma k_a \sum_p \frac{k_{rp}}{\mu_p B_p}(\Phi_{pf} - \Phi_{pm}). \tag{2.4}$$

When a transfer function is defined the balance equations for all three phases in a black oil formulation can be written:

$$\nabla\left[\frac{k_{rw}}{\mu_w B_w} k \nabla \Phi_w\right] + \tilde{q}_w \pm q_{wmf} = \frac{\partial}{\partial t}\frac{\phi S_w}{B_w} \tag{2.5}$$

$$\nabla\left[\frac{k_{ro}}{\mu_o B_o} k \nabla \Phi_o\right] + \tilde{q}_o \pm q_{omf} = \frac{\partial}{\partial t}\left(\frac{\phi S_o}{B_o}\right) \tag{2.6}$$

$$\nabla\left[\frac{k_{rg}}{\mu_g B_g} k \nabla \Phi_g + \frac{R_s k_{ro}}{\mu_o B_o} k \nabla \Phi_o\right] + \tilde{q}_g \pm q_{gmf} = \frac{\partial}{\partial t}\phi\left(\frac{S_g}{B_g} + \frac{R_s S_o}{B_o}\right) \tag{2.7}$$

As described by Gharsalla (2015): "Equation 2.5 to Equation 2.7 give the black oil balance equations considering three components in three phases (subscripts *w*, *o*, and *g* for water, oil and gas). Each continuum is a single porosity medium, therefore, the flow equations are identical for both continua. The only difference is that the transfer terms have the opposite sign: $^{+}/_{-}q_{wmf}$ for water, $^{+}/_{-}q_{omf}$ for oil and $^{+}/_{-}q_{gmf}$ for gas. *B* is the formation volume factor and $\tilde{q}$ is the volumetric source/sink term. Equivalent compositional and non-isothermal formulations are also well known. The balance equations have to be written for both continua.The last terms at the left hand side represent the rate of the mass transfer between the fracture and matrix continua."

When also matrix-to-matrix transmissibilities are considered, allowing flow in from one matrix grid cell to another, the model is called dual-permeability model (Figure 2.5). Dual continuum models of this type are useful when e.g. the matrix significantly contributed to fluid flow within the reservoir. However, when also matrix-to-matrix flow has to be calculated the linear equation system becomes larger and more CPU-time is required for a solution.

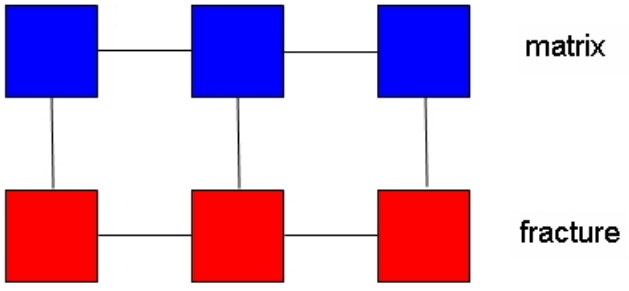

Figure 2.5: Dual porosity - dual permeability dual permeability concept

Multiple models exist for the determination of the transfer term. They will be discussed in Chapter 3 and the verification of the models can be found in Chapter 4 and Chapter 6.

2.3.1 Matrix Blocks and Simulation Cells

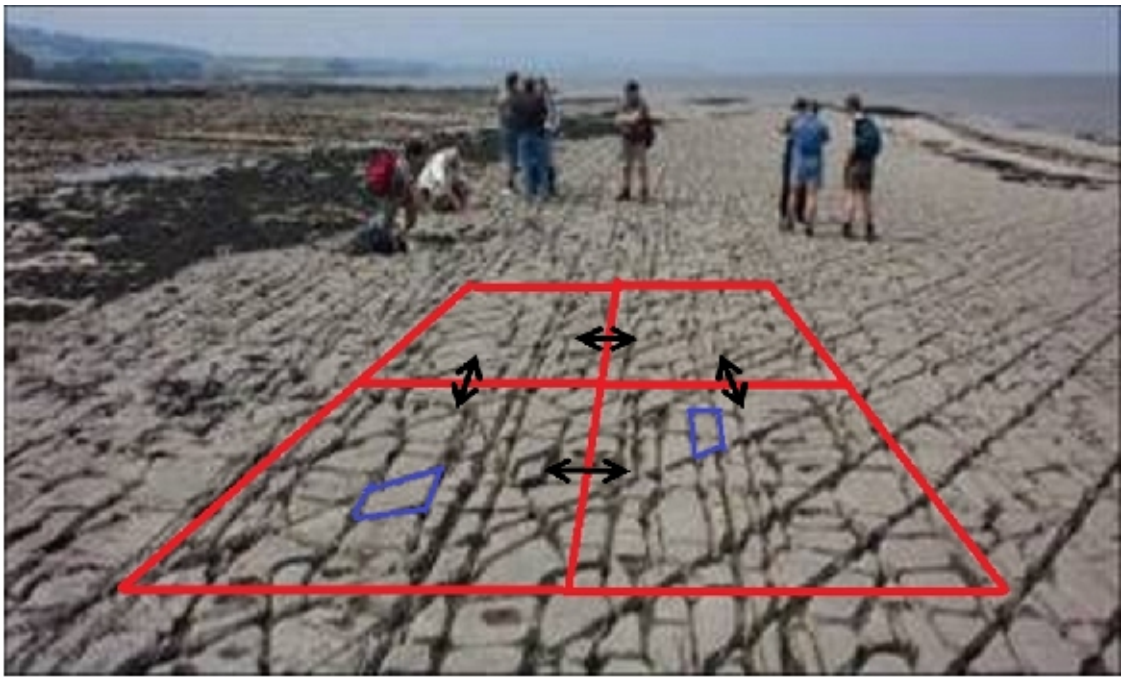

Figure 2.6: Fractured Rock, Matrix cell vs. matrix block, (Roxar training)

Heinemann and Mittermeir (2014) described the difference between matrix blocks and simulation cells in dual continuum models as follows:

(In order to calculate fluid flow within the dual porosity system numerically, Equation 2.5 to Equation 2.7 have to be discretized. To avoid ambiguities one should distinguish between *matrix blocks* and *simulation cells*. The red squares in Figure 2.6 (or cubes in 3D) represent the control volumes, in other words the "*simulation cells*". The dual continuum approach considers two simulation cells at each location (i.e. at the place of each red square); one is the "*matrix cell*" and the other is the "*fracture cell*". This divides the space into two identically-shaped domains: the "*matrix domain*" and the "*fracture domain*". The fracture domain, built by the fracture cells, commonly has a much higher permeability and less porosity than the matrix domain. This means that the fracture cells can exchange fluids easily with their neighboring fracture cells (along the black arrows in Figure 2.6). Matrix cells, may or may not be able to exchange fluids with their matrix neighbors resulting in dual permeability or dual porosity models, respectively. Figure 2.6 is the two dimensional outcrop of a naturally fractured formation. This figure explains the fundamental problems that should be overcome while modeling fluid flow in such a discontinuous domain. The fractures surrounding the blue-framed "*matrix blocks*" determine their boundary conditions, imposing how the hydrocarbon will be recovered from the matrix block. On the other hand, the matrix blocks serve as the internal mass source and sink for the

fracture system.)

This clear distinction is important to avoid ambiguities and therefore this nomenclature is also followed in this thesis.

2.4 Subgridding of Matrix Blocks

Saidi (1983) presented at method, where the matrix is gridded into vertical cylinders (Figure 2.7). After evaluation of the pressure in the fracture and the individual matrix blocks the phase potential is determined for all grid cells, also accounting for capillary forces. The transmissibility between fracture and matrix is then distributed to the grid cells based on open matrix boundary area. It is possible to define sealing boundaries, for example to restrict flow from the bottom and top of the matrix blocks. Using this method the Iranian Haft-Kel field was history matched.

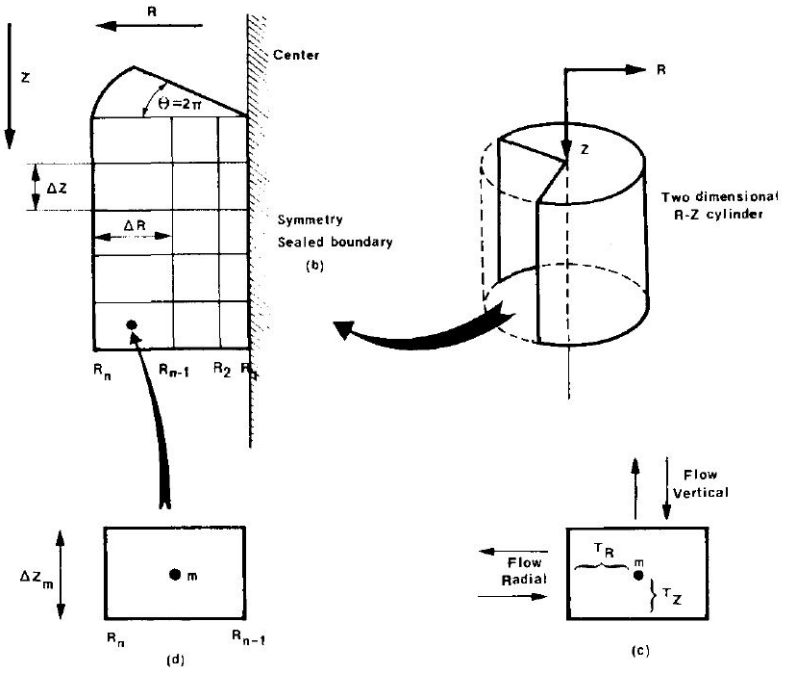

Figure 2.7: Matrix element with grid block definition (Saidi 1983)

The Multiple Interacting Continua (MINC) concept was introduced by Preuss and Narasimhan (1985). In this method, the matrix cells are discretized into nested elements with surfaces parallel to the nearest bounding fracture (Figure 2.8). This is done because it is assumed that the condition at a certain point in space of the matrix primarily depends on its distance to the fracture plane. The fracture provides a uniform boundary condition to the outermost matrix element. It is clear that this assumption is never fully valid, because within the fracture potential gradients or a non-uniform saturation could exist. In their presented method, the flow is

restricted into the outwards direction from matrix to fracture.

Preuss and Narasimhan (1985) describe a three-step procedure for defining a MINC mesh:

1. Creation of the primary mesh. This mesh considers the general geometry and parameters of the reservoir.
2. Defining elemental volumes, interface areas, nodal distances and volume fractions of the individual discrete elements.
3. Applying scaling laws to consider that the in a typical matrix cell more than one SMB is located.

A verification of this method was done by Wu and Pruess (1988) by comparing MINC results with one of a model with discretized matrix blocks bounded by a uniform fracture. Generally, high CPU time of the MINC method is problematic. Naimi-Tajdar et al. (2006) therefore implemented the MINC method in a 3D, compositional reservoir simulator that using parallel computing. By using 16 processors instead of 1 the calculation time of their test model was decreased by a factor of over 10.

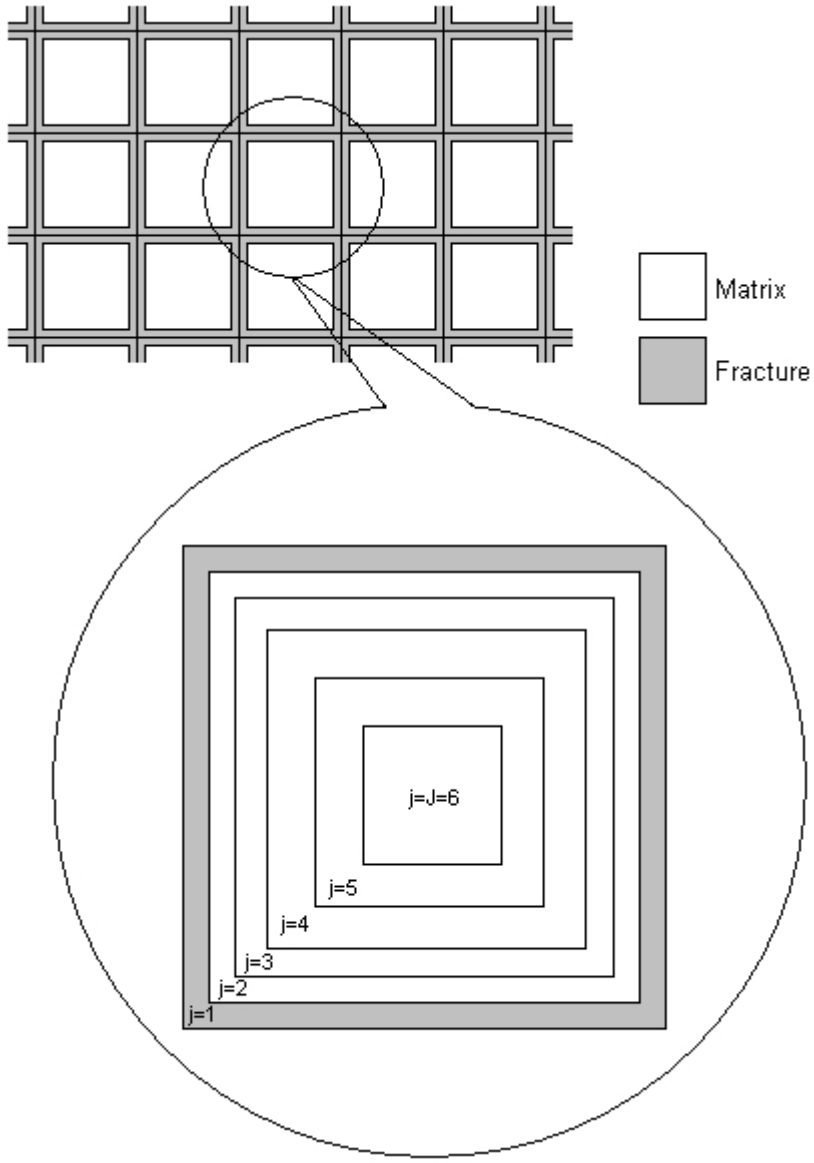

Figure 2.8: The MINC discretization (Preuss and Narasimhan (1985))

Gilman and Kazemi (1988) presented a method for subgridding the matrix blocks, similar to the MINC method. They showed two options for dividing the matrix blocks (Figure 2.9), one with stacked blocks in vertical direction and one with nested blocks similar to the one used in MINC. Vertically stacked matrix blocks allow for the modeling of phase segregation within matrix blocks. As this is a strict dual-porosity approach, no fluid transfer can happen between matrix blocks of different grid cells. For the matrix-fracture mass transfer still the transfer equation Equation 2.4 is used, with possibly different shape factor values for the individual matrix grid blocks that are connected to the fracture. Naturally, also the matrix subdivided cells communicate with each other. Problematic is the increased CPU time, which is stated by Gilman and Kazemi (1988) to be between 20 and 80%.

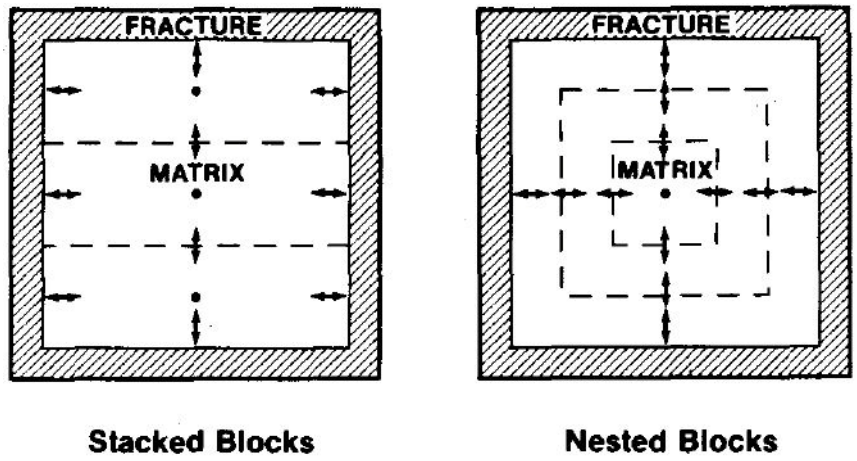

Figure 2.9: MINC-type method after Gilman and Kazemi (1988)

2.5 Discrete Fracture Modeling

In the last decades many efforts, mostly of academic nature, have been undertaken to create Discrete Fracture Models (DFM) and make them applicable for reservoir simulation. In this concept the fractures are considered explicitly as discretized entities and therefore they rely heavily on unstructured grids. The discretization method used can be either finite element (e.g. Karimi-Fard and Firoozabadi 2003), control-volume finite element (e.g. Fu, Yang and Deo 2005) or control-volume finite difference (e.g. Karimi-Fard, Durlofsky and Aziz 2004). Figure 2.10 shows how fracture are represented in a DFM, in this case a control-volume finite element one. Hoteit and Firoozabadi (2006) also developed a compositional formulations for DFM.

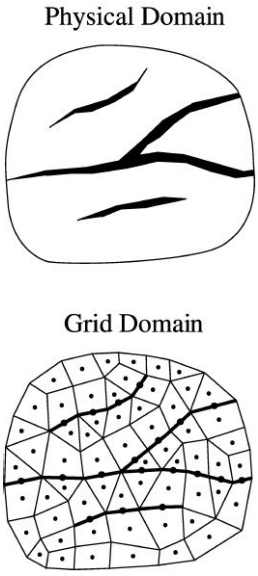

Figure 2.10: Representation of fractures in a DFM using control-volume finite elements (Karimi-Fard, Durlofsky and Aziz 2004)

Drawbacks of DFMs are the high computational cost (Geiger et al. 2009) as well as the complex and challenging grid generation for such models (Moinfar et al. 2014). The grid has to represent the modeled fractures. If parameters like the fracture density or length of fractures is adapted during the modeling process, it is required to generate a new grid for each manipulation. Thus, an application to a full field with multiple geological realizations is time consuming and expensive. Most of the models applied are small in scale, with one of the most often used being a Bristol Channel outcrop (Figure 2.11). The author of this work asserts that models dealing with such scales are not directly connected to the objective this thesis.

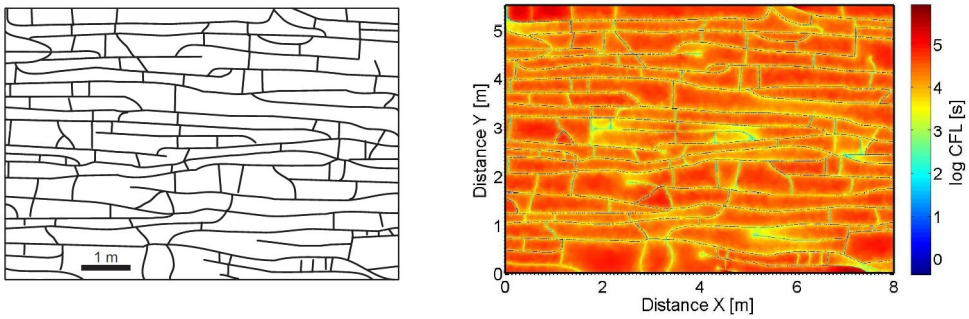

Figure 2.11: Bristol Channel fracture pattern (left) and corresponding DFM model (right) (Geiger et al. 2009)

Recently, Embedded Discrete Fracture Modeling (EDFM), which is a hybrid method between DFM and DCMs emerged. Li and Lee (2008) were proposed such a method where based on stochastic modeling of fracture networks the fractures are divided into classes of different fracture lengths. Shorter fractures are accounted for by manipulating the matrix permeability, longer ones are explicitly modeled. The transfer between the larger fractures and the matrix is calculated using a transfer equation based on Peaceman's well equations. Moinfar et al. (2014) improved this method by including the possibility to model fractures of different orientations, whereas the Li and Lee (2008) only considered fractures perpendicular to layers. A geometrical representation of an EDFM grid can be seen in Figure 2.12.

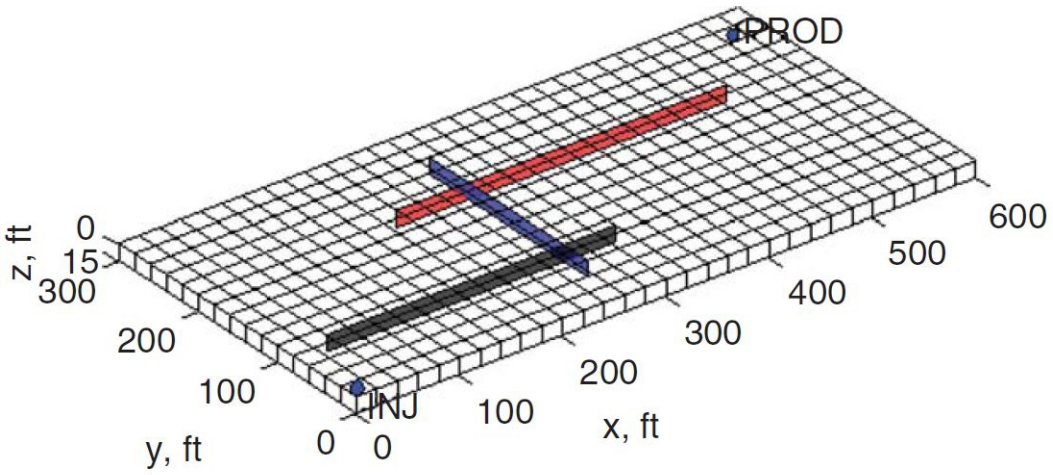

Figure 2.12: Geometrical representation of an EDFM grid with discrete fractures (Moinfar et al. 2014)

2.6. Single Matrix Block Modeling

SMB models have been used to investigate the oil recovery from SMBs since decades. Whereas in the dual continuum formulation only averaged pressure and saturation is considered, fine grid SMB models can model all non-uniformities within the matrix associated with the recovery process. However, on a reservoir scale it is not feasible to discretize the matrix into individual fine grid SMB models. Approximations like the MINC by Pruess and Narasimhan (1985) or Gilman and Kazemi (1988) to this fine grid SMB models for full field simulation have been mentioned above.

The following two paragraphs, providing a brief historical overview, is taken from Steiner and Mittermeir (2017):

„Historically Yamamoto et al. (1971) were the first to perform calculations on a SMB model, followed by Kleppe and Morse (1974). Both used two-dimensional models, surrounded by narrow fractures. Later authors also used 3D models. The following have to be mentioned in this context: Thomas et al. (1983), Rossen and Shen (1987), Coats (1989), Fung and Collins (1991), Kazemi et al. (1992), Chen et al. (1995), Gurpinar and Kossack (2000), Famy et al. (2005), Kossack (2006). Balogun et al. (2007). Practically all possible recovery mechanisms, under various model setups were considered. The available literature clearly demonstrates the continuous efforts to capture the parameters influencing the flow behavior of any matrix block assembling the reservoir body.

One of the widely discussed properties of a SMB is its shape, which may be approximated by

various geometrical bodies like cubes or cylinders. Barker (1985) identified that the flow behavior of the model depends on its *surface-to-volume ratio* and not its shape. Thus, if these ratios of two matrix blocks of different shapes are the same, the matrix-fracture mass change rate will be the similar, as long as the driving forces are the same. The forces to consider are the compressional, capillary, gravitational and viscous ones. The first two act uniformly on the block, but the latter two are influenced by the extension of the block in the direction of the pressure gradient in the bounding fractures. Considering gravity drainage means that the flow behavior is the same if the heights of the matrix blocks are identical. Wuthicharn and Zimmerman (2011) concluded that for an expression of the shape factor considering only a surface to volume ratio, it is possible to predict shape factors for irregular shaped matrix blocks with an error of less than 10%. Consequently, for all practical s the shape of matrix blocks can be disregarded as long as the surface to volume ratio is correct, since a determination of the matrix block shape in a real reservoir is in any case impractical. Therefore, although the blocks in Figure 2.13 have a different shape, as long as they have the same surface-to-volume ratio and the same height, they are equivalent.)

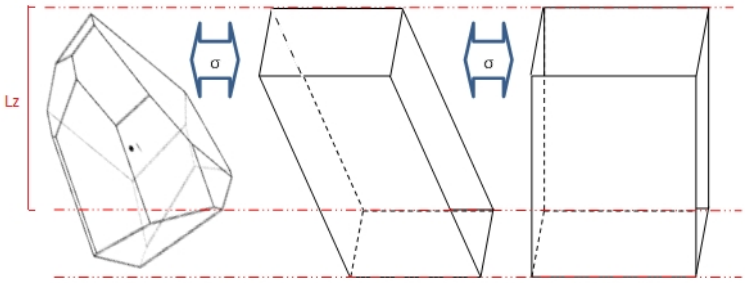

Figure 2.13: Different matrix block shapes with the same shape factor and flow behavior (Heinemann and Mittermeir 2016)

The SMB model, which is used in this work was already used by Pirker, Mittermeir and Heinemann (2007) and since then used for many scientific and technical works. Gharsalla (2015) proved that a grid dimension of 7x7x21 for a quarter model, as shown in Figure 2.14, is generally applicable. Because of symmetry reasons it is only necessary to calculate on a quarter model, although the herein used reservoir simulator H5 also offers the possibility to use a full block.

The user of the SMB model can manipulate input parameters for modeling the desired matrix block. Rock properties that can be changed are the porosity and the permeability, which can be different in x, y and z direction. The size of the SMB is chosen explicitly by defining the vertical and horizontal extension or alternatively by providing only the vertical extension together with a shape factor. Naturally, also the saturation dependent rock functions and PVT data can be changed.

The initial pressure of the SMB is based on an input pressure, which will be assigned to the central matrix layer. The pressures above and below that are then set according to the present fluid density. This gravitational gradient is generally different for matrix and fracture. Therefore, initially the average pressure is the same for fracture and matrix, but the system is

not necessarily in equilibrium. The initial saturation of the SMB depends on if oil recovery or oil resaturation should be calculated. In case of oil recovery, the initial saturations are: $S_w = S_{wi}$, $S_g = 0$, $S_o = 1\text{-}S_{wi}$. For oil resaturation this depends on what beforehand occurring recovery mechanism is assumed. For oil resaturation after waterdrive the initial saturations are: $S_o = S_{orw}$, $S_g = 0$, $S_w = 1\text{-}S_{orw}$ and after gasdrive they are: $S_o = S_{org}$, $S_w = S_{wi}$, $S_g = 1\text{-}S_{org}\text{-}S_{wi}$. Expansion and solution-gas drive are modeled by filling and re-filling the fracture with oil, which has a slightly higher bubble point than the one in the matrix.

The fracture planes, which can be seen as the grey grid cells in Figure 2.14, are used to set the boundary condition for the matrix block. They can be either on all sides of the matrix block or only vertically bounding. The hydrostatic pressure distribution in the fracture imposes the pressure boundary condition for the matrix. It is also possible to model fluid movement in the fracture by setting a viscous pressure gradient in the fracture. During the calculation all fracture parameters, like fluid content, pressure, and pressure gradient can be changed. The fracture volume is high, so that the saturation changes during a time step do not have an influence on the calculation. At the end of every time step the from the matrix expelled fluid is removed and the saturation is set back to the desired boundary condition.

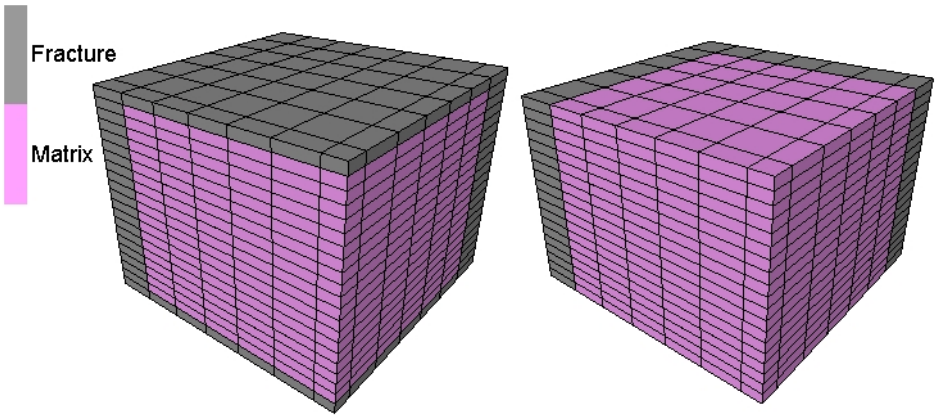

Figure 2.14: Quarter of a SMB model, fully surrounded by fractures (left) and with vertical fractures only (right). (Heinemann and Mittermeir 2016)

2.7 Dual Porosity Material Balance

Material balance (MB) calculation was first introduced into reservoir engineering by Schilthuis (1936) and later well known formulations are by Tarner (1944) and Muskat and Taylor (1946). Until reservoir simulation emerged, MB calculation was the only reservoir engineering method for determining drive mechanisms and making predictions on a field level.

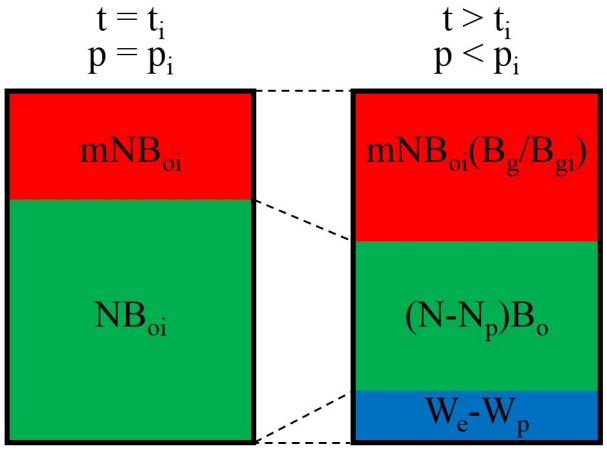

Figure 2.15: The scheme of the material balance of an oil reservoir

Figure 2.15 shows the principal of material balance calculations. Initially (left) the reservoir is at pressure p_i, and the oil phase occupies a reservoir volume of NB_{oi}, where N is the original oil in place and B_{oi} the original oil formation volume factor. Additionally, a gas cap with the volume mNB_{oi} is present, where m is the gas cap factor. After some time and an oil production N_p and a water production W_p, the pressure drops. The volume of the reservoir remains constant and therefore the gas cap expands and water influx W_e from an aquifer occurs. It can be seen that this classical material balance, when applied to a NFR, does not provide any indication of if the fluids are in the fracture or the matrix and does not consider the fracture-matrix interaction.

Efforts to make the MB suitable for NFRs have been made by distinguishing between fracture and matrix. One approach was to consider the different pore compressibility of the fracture and the matrix (Penuela et al. 2001, Sandoval Merchan et al. 2009, Bashiri and Kasiri 2011). However, such methods still do not consider any interaction between the matrix and the fracture.

Based on the Heinemann (2004) concept of using recovery curves directly for determining fracture-matrix fluid transfer, Mittermeir (2015) developed the first dual porosity MB method which accounts for the interaction and mass transfer between fracture and matrix and considers capillary, gravitational and viscous forces. Instead of the single approach of the classical MB, two barrels are used, one representing the matrix and the other the fracture volumes. The fluid transfer is determined directly from oil recovery curves, which could be gained from fine grid SMB experiments. The schematic of such a MB model can be seen in Figure 2.16. In Zone 3, water enters the matrix and displaces oil, after the oil water contact has risen. In this zone the fluid transfer is determined by a waterdrive recovery curve. Zone 1, where the fracture is filled

only by oil, expansion is the sole driving force and therefore no recovery curve is applied. In zone 2, the fracture is gas-filled and displaces oil from the matrix and the fluid transfer is determined by a gasdrive recovery curve.

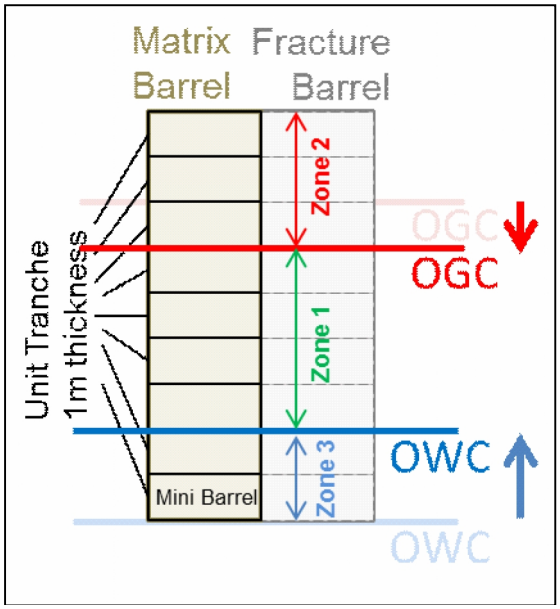

Figure 2.16: Dual porosity MB model with moving phase contacts (Mittermeir 2015)

Chapter 3

Matrix-Fracture Mass Transfer Concepts in Dual Continuum Models

This chapter summarizes the different approaches for modeling the mass transfer between matrix and fracture in DCMs. Available experimental evidences are also briefly discussed and it will be shown that a verification of the matrix-fracture mass transfer concepts cannot be done based on these experiments.

3.1 Experimental Evidences of Matrix Oil Recovery

This section is taken from Steiner and Mittermeir (2017) without major modifications. The review of published experimental evidences was done at the end of 2016 and can therefore be considered to be up to date.

Authentic results of experiments dealing with the recovery of oil from the matrix would require representative matrix blocks (rock-type, size), reservoir fluids and physical conditions (temperature, pressure) as well as an appropriate time of investigation. At a minimum the most important driving forces (capillary imbibition, gravity drainage, solution gas drive) should be considered.

Up to now, no experimental work is known which would fully satisfy these requirements. The experiments were made on small plugs, mostly on Berea sandstone cores or artificial compacted packs (often using Al_2O_3 powder). The Berea samples will be signed by *BS* in the following.

Most experiments focus solely on the driving force of **capillary imbibition**. Mattax and Kyte (1962) have published the first experimental evidences for the capillary imbibition results. They conducted six experiments for both linear and three-dimensional oil displacement from cylindrical samples and recorded the recovery factors as a function of time. The sizes of the samples ranged between 2.8 to 11 cm in length and from 2.54 to 5 cm in diameter. For the creation of the samples for linear displacement Al_2O_3 powder was used, for the three-dimensional displacement a sandstone was used.

Kleppe and Morse (1974) used *BS* for the creation of cylindrical samples (10.16 cm diameter, 121.92 cm length) for their experiments. The cylinder was mounted vertically in a tube with 2.5 mm annular space, representing the surrounding fracture. Capillary pressure curves as well as relative permeability have been determined experimentally. The results have been documented as cumulative oil production from the core as a function of cumulative water injection.

Kazemi and Merrill (1979) conducted experiments on both cylindrical (2.54 cm diameter, 7.62 cm length) and rectangular block (5.08 x 10.16 x 10.16 cm) samples made of *BS* with a single artificial fracture. The artificial fracture cut the matrix in two halves, creating two separate matrix blocks. Injection and production was done only through the fracture. For one of the samples also capillary pressure measurements using the centrifuge method were performed.

Hamon and Vidal (1986) used Fontainebleau sandstone and Al_2O_3 samples with lengths ranging from 10 to 85 cm and a diameter of 7.6 cm. A total of 18 imbibition and waterflood experiments have been conducted.

Morrow et al. (1994) used 21 cylindrical samples of *BS* (3.8 cm diameter, 6.2 - 7.2 cm length) for imbibition and waterflooding (forced imbibition) experiments.

Zhang and Morrow (1996) conducted imbibition experiments on 13 cylindrical samples (3.81 cm diameter, 1.17 - 10.24 cm length) from *BS.* Zhoue, Morrow and Ma (2000) performed imbibition and waterflood experiments on 41 *BS* plugs. The cylindrical samples were 3.8 to 3.82 cm in diameter and 6.4 to 7.8 cm long.

The issue of co-current vs. counter-current imbibition was examined by Bourbiaux and Kalaydjian (1990) with parallelepiped shaped sandstone samples (6.1 x 2.1 x 29 cm). Oil recovery rates from co-current imbibition, modeled by opening top and bottom of the sample, was much faster compared to counter-current imbibition, where the fracture was open only on one side. In addition, Pooladi-Darish and Firoozabadi (2000) experimented with co-current vs. counter-current imbibition. Cubic Kansas chalk (6 x 18.75 x 30.48 cm) and *BS* (14.71 x 14.71 cm x 60.47 cm) samples have been used. Co-current imbibition was modeled as a slowly advancing water level surrounding the matrix block, showing a faster oil recovery compared to a fully immersed block.

Rangel-German and Kovscek (2002) studied the capillary imbibition process on cubic *BS* samples with X-ray CT using mostly water and air as fluids. Injection and production took place from a single fracture located at the bottom of the sample. It was found that for very high matrix-fracture transfer rates the recovery scales linearly with time and in the case of lower transfer rates and finer fissures the recovery scales with the square root of time. Le Guen and Kovscek (2006) conducted experiments with the same technique as Rangel-German and Kovscek (2002) with cylindrical cores of 9 cm length and 2.5 cm diameter and found that at core scale the capillary imbibition process is a non-equilibrium process. However, due to the different scale and timeframe of laboratory core investigations these results cannot be seen as evidence for the field scale (Hirasaki 1980).

To consider the **gravity drainage** driving force in addition to the capillary imbibition would require samples with heights representative of the reservoir conditions, which is far beyond any

experiment found in literature. Kyte (1970) presented experiments including gravity drainage using centrifuges to scale the potential difference due to gravitational forces. However, as already stated by Hassler and Brunner (1945), it is not possible to exactly scale gravitational forces with a centrifuge. The acceleration on the sample is not constant over the entire length leading to a non-linear apparent gravity gradient. For the experiments, cylindrical samples from preserved cores were used with matrix block heights of 4.9 cm and 9.8 cm and diameters of 1.88 and 3.76 cm, respectively.

Li et al. (2000) used two cylindrical *BS* cores with lengths of 24.45 cm and 48. 74 cm and a diameter of 10.16 cm. The timeframe of investigation was 30 days for the smaller core and 18 days for the larger one. Recovery curves (RC) for both cores have been determined. However, the cores have been artificially fractured in different positions and therefore both cores do not act as a SMB.

Rangel-German and Kovscek (2002) demonstrated the influence of gravity drainage by testing water displaced by air with a fracture on top of the core-sized matrix block, in contrast to their other experiments that had the fracture at the bottom. However, the scale dependency of the gravity drainage driving force was not further investigated.

Laboratory experiments dealing with **single-phase expansion** and **solution gas drive** are described e.g. in Morel et al. (1992), Sahni et al. (2001) or Bayon, Cordelier and Nectoux (2002). Experiments both on cores as well as on outcrop samples with live oil under reservoir conditions have been conducted. Pressure drawdown was achieved by producing oil from the bottom of the sample and gas from the top.

To summarize, it was not possible to find experimental results representative of a full-size SMB at reservoir conditions. Most experiments deal with the capillary imbibition only and do not model other driving forces simultaneously.

3.2 Approach with Analytical Recovery Functions

Reiss, Bossie-Codreanu and Lefebvre Du Prey (1973) presented a method for determining three-dimensional multi-phase mass transfer rates in dual-porosity models for NFRs. Their transfer model uses RCs for the determination of the matrix-fracture transfer rate. They presented 7 numerical models of varying complexity and scale, including a SMB one. It is suggested to use the SMB calculation for evaluating the RCs used for determining the matrix-fracture mass transfer.

Initially, matrix and fracture are oil saturated. When production commences the pressure in the fracture drops and oil is flowing fro the matrix into the fissures based on fluid/rock expansion and solution gas drive. (When the matrix block is reached by the water-oil or gas-oil contact, the depletion of the matrix is caused by capillary and gravity effects. This depletion process is modeled as a function of the elapsed time after water (or gas) comes in contact with the matrix block via the surrounding fractures. The phases are completely segregated in the fissures and

the matrix block is completely surrounded by water or gas. The matrix-fracture exchange will be represented by time-dependent source or sink functions, also named as recovery functions or RCs. Rossen (1977) used the same approach with semi-implicit handling of the source terms.)

After the phase contact arrival and the application of the purely time-dependent transfer functions, the fluid and rock compressibility as well as the fracture viscous flows are not considered for the matrix-fracture mass transfer. Although Reiss, Bossie-Codreanu and Lefebvre Du Prey (1973) claimed that this is not restrictive for usual field applications, this assertion is not proven or acknowledged in the literature, as mentioned by Heinemann and Mittermeir (2014).

With their CFRAC numerical model, which is a SMB with a surrounding fracture, Reiss, Bossie-Codreanu and Lefebvre Du Prey (1973) presented a tool for creating the RCs. Another possibility for deriving such time functions would be laboratory experiments, where the work of Mattax and Kyte (1962) must be mentioned. Based on their experiments, Kazemi, Gilman and Elsharkawy (1992) showed that for water imbibition the RC can be approximated by using an exponential equation as already suggested by Aronofsky (1958):

$$E_R(t) = E_{R,\,max}(1. - e^{-\lambda t}) \tag{3.1}$$

Many other equations have been suggested for estimating the RC of a SMB by either superimposing multiple exponential functions (Kazemi, Gilman and Elsharkawy 1992) or using early and late time functions (Rangel-German and Kovscek 2002).

3.3 The Transfer Function Approach

The transfer function (TF) approach, goes back to Barenblatt, Zheltov and Kochina (1960) and Warren and Root (1963), as already described in Chapter 2. Warren and Root (1963) derived their transfer equation based on the sugar cube model, an idealized model of a NFR (Figure 3.1). After the extension to multi-phase flow by Kazemi et al. (1976) the TF became the most widely used method for determining the matrix-fracture mass transfer.

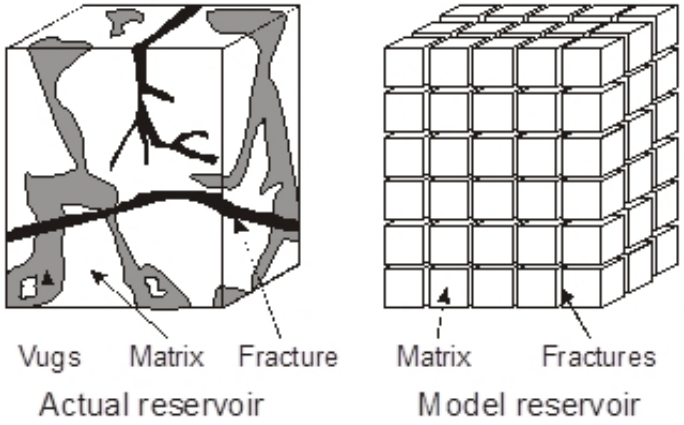

Figure 3.1: Idealization of a fractured reservoir (after Warren and Root 1963)

Their transfer function with the obligatory shape factor will be discussed:

$$q_{cmf} = V_{cell}\sigma k_a \sum_p \frac{k_{rp}}{\mu_p B_p}(\Phi_{pf} - \Phi_{pm}) \quad , p = w, o, g, \tag{3.2}$$

where V_{cell} is the pore volume, index p denotes the phase, k_a is the apparent matrix permeability, μ the viscosity, B the formation volume factor, k_r the relative permeability and Φ the phase potential in the fracture (f) and in the matrix (m). The shape factor (SF), σ, is a characteristic value of the matrix block considering its geometry.

For the application of the TF it is critical to find suitable values for the SF. Warren and Root (1963) proposed an equation for determining the SF:

$$\sigma = 4N \cdot \frac{(N+2)}{L^2} \tag{3.3}$$

where N is the number of fracture sets and L is the dimension of the cubic matrix block.

Kazemi et al. (1976) derived a SF for their transfer equation, which is widely accepted and used:

$$\sigma = 4\left(\frac{1}{L_x^2} + \frac{1}{L_y^2} + \frac{1}{L_z^2}\right). \tag{3.4}$$

Kazemi, Gilman and Elsharkawy (1992) then provided a more general expression for the shape factor as:

$$\sigma = \frac{1}{V}\sum_s \frac{A}{d}, \tag{3.5}$$

where V is the matrix block volume, A is the surface area open to flow at surface s, and d is the distance from the open surface to the center of the matrix block.

Heinemann and Mittermeir (2012) gave the most general version for the shape factor as:

$$\sigma = \frac{1}{V_m} \sum_{j=1}^{N} A_j \frac{\left| \bar{\bar{k}}' \vec{n}_j \right|}{\left| \vec{d}_j \right|}, \tag{3.6}$$

where V_m is the volume of the matrix block, $\bar{\bar{k}}$ is the normalized permeability tensor, subscript j denotes the sno. and N the total number of surfaces A towards the surrounding fracture network. $\vec{n}$ is the unit normal vector and $\vec{d}$ is the distance vector to these surfaces. Heinemann and Mittermeir (2012) showed that Equation 3.6 contains all other forms of shape factors introduced earlier. Heinemann and Mittermeir (2012) also showed that the general shape factor definition is only valid for pseudo-steady-state conditions, a linear potential gradient and uniform matrix saturation.

(Numerous efforts for finding an improved shape factor can be found in the literature. They are either derived from theoretical considerations, laboratory or numerical experiments. Derivations can be found in Thomas et al. (1983), Barker (1985), Ueda et al. (1989), Coats (1989), Kazemi and Gilman (1993), Chang (1993), Zimmerman et al. (1993), Lim and Aziz (1995), Gilman (2003), Gerke and van Genuchten (1996) and Lewandowska et al. (2004). In all of the mentioned publications shape factors are derived, that are either smaller or greater than the one by Kazemi et al. (1976), but still constant.) In Chapter 4 it is shown that for a general case it is not possible to find a constant shape factor value.

Recognizing the problem with constant shape factors, some researchers developed time-dependent shape factors (Penuela 2002, Rangel-German and Kovscek 2003, Su et al. 2013), although the shape of the matrix block is not changing. Therefore, this can be seen as a band-aid for correcting a fundamentally flawed approach.

A more detailed review of the development of the shape-factor concept as well as the derivation of the generalized shape factor can be found in Heinemann and Mittermeir (2012). As the shape factor concept is widely applied and in many cases useful despite its flaws, Steiner and Mittermeir (2017) conducted a thorough analysis of the applicability of the shape factor concept, which can also be found in Chapter 4.

Another difficulty is the determination of the potential differences in Equation 3.2. Generally, the potential difference comprises capillary, gravitational and compressional forces and can be written for the three phases water (w), oil (o) and gas (g):

$$\Phi_{wm} - \Phi_{wf} = p_{om} - p_{of} - P_{cwom} + P_{cwof} + P_{hwom} - P_{hwof} \tag{3.7}$$

$$\Phi_{om} - \Phi_{of} = p_{om} - p_{of} - P_{hwom} + P_{hwof} \tag{3.8}$$

$$\Phi_{gm} - \Phi_{gf} = p_{om} - p_{of} + P_{cogm} - P_{cogf} + P_{hgom} - P_{hgof} \tag{3.9}$$

where Φ is the potential, subscripts m and f denote "matrix" and "fracture", p is the pressure, P_c the capillary pressure and P_h the hydrostatic pressure. For the pressure only the average pressure

of the cell can be considered, the pressure at the midpoint of the matrix block is not known. The capillary pressure is based on a capillary pressure curve, which is a function of saturation. In this case the known saturation is the average saturation of the matrix cell, which is also assumed to be the average saturation of the matrix blocks inside the cell. The general assumption is that this average saturation is uniformly distributed. Efforts to account for the non-uniformity of the saturation distribution can be found in commercially available simulators (Schlumberger ECLIPSE, BeicipFranlab PumaFlow) by adjusting the capillary pressure curve. For the determination of the differences in hydrostatic pressure multiple models exist. The most widely used ones are the one by Gilman and Kazemi (1988) and Quandalle and Sabathier (1989).

3.3.1 Efforts to Find an Improved Transfer Function

This brief literature review on the efforts to find an improved version of the transfer function is taken from Steiner and Mittermeir (2017), as it is up to date and fits the objective of this work:

Many attempts have been made for improving the Kazemi et al. (1976) transfer equation or finding alternative transfer functions. Viscous forces and gravity drainage was included into the model by Gilman and Kazemi (1983), Gilman (1986) and Gilman and Kazemi (1988).

Quandalle and Sabathier (1989) separated horizontal and vertical flow. This makes it possible to consider anisotropy and different shape factors in horizontal and vertical direction. For this method an estimation of the apparent fluid density is required for the horizontal flow. Because this is done explicitly, the numerical stability is reduced and smaller time steps may be required. Abushaikha and Gosselin (2008) suggested that based on their SMB investigations the Quandalle and Sabathier (1989) gravity drainage model is more suitable when gravity is the dominant driving force, as is the case in gas-oil gravity drainage cases.

Zimmerman et al. (1993) modified the transfer equation for the single-phase case to account for the early time transient flow behavior within the matrix. The results were compared with MINC-type (Pruess and Narasimhan 1985) simulations, showing good agreement.

A different approach without shape factors was chosen by Di Donato et al. (2007) and Lu et al. (2008), who decomposed the overall mass transfer into multiple rates from different physical processes, called “Generalised Transfer Function”. Each of these processes is described in a functional form. Corrections for early and late time behavior are used. This non-shape factor based method was “validated” by comparing it against the results of numerical fine grid models of SMBs. Independently, this method was also compared with SMB results by Abushaikha and Gosselin (2008). They concluded that the match with SMB results is good for early times, but the speed of recovery is overestimated for later times. Geiger et al. (2013) presented a higher order multirate model, but calibrating the individual transfer functions is difficult also for their approach.

Abushaikha and Gosselin (2009) developed the so-called “SubFace Transfer Function”. Similar to the Quandalle and Sabathier (1989) approach, the vertical and horizontal flow is separated, where the vertical part is again divided based on the matrix saturation.

Su et al. (2013) used fine grid SMB calculations for calibrating time-dependent shape factors. With these time dependent shape factors they were able to match the results of the fine grid SMB calculations using a dual continuum formulation. In contrast to the SMB model used in this work, Su et al. (2013) did not include capillary pressure and dissolved gas in their calculations.

None of the above-mentioned methods was experimentally validated.

3.4 Application of Numerical Recovery Curves

Heinemann (2004) suggested, that instead of using numerical SMB experiments for validating or correcting transfer equation, to use them directly for determining the matrix-fracture mass transfer in dual-porosity models of NFRs. The principle of this concept is the separation of driving forces into pressure and saturation dependent ones and that their impact can be superposed.

Expansion and solution-gas drive are purely pressure dependent processes and can be modeled with a transfer equation like the Kazemi et al. (1976) one. If no pressure change happens in the system then this part does not contribute to the oil recovery. Water or gas displacement of oil are mostly saturation dependent and therefore primarily time-dependent and only to a lesser degree pressure dependent. This should be modeled using numerically derived RCs, similar, but more general than the Reiss et al. (1973) approach. The RC already contains information about the capillary and gravitational forces. The capillary driving force is purely saturation dependent and can be modeled with a time-function. The gravitational driving force is a function of block geometry and fluid density. The information about block geometry is exactly given in the RC, the information about fluid density is also given, but only for a certain pressure at which the RC was calculated. The changes in the gravitational force can be considered, as will be shown in this thesis.

Pirker (2008) presented an implementation of the RCM, where the applicability was shown in a two-phase water-oil example. Matrix blocks of different sizes within one single simulation grid cell were modeled using so-called lumped RCs. These are "averaged" RCs from a number of SMB calculations. It should be noted, that this is not the same as using RCs of averaged matrix sizes and properties.

Amiry (2014) introduced to concept of RC regions, where input RCs are assigned on a gridcell basis. This is necessary for heterogeneous reservoirs with strongly varying matrix block parameters.

Heinemann and Mittermeir (2016) later introduced the first type of scaling to a RC based on its pressure and saturation condition. The applicability of their implementation of the RCM including the scaling of the RC increment was shown on a dual continuum single matrix cell.

The next step in the development of this method is presented in Chapter 5 of this dissertation.

Chapter 4

Verification of Mass Transfer Equations

Some of the herein described SMB experiments have already been published by Steiner and Mittermeir (2017). Parts of the text have been reused for this chapter without modification (with the consent of the co-author of the publication), other parts have been rewritten, re-ordered or extended. Thus, the level of detail and the structure of this chapter is significantly higher than the one of Steiner and Mittermeir (2017). Results of experiments, which were omitted in Steiner and Mittermeir (2017) will be shown and discussed.

4.1 Experimental SMB Setups

A SMB model setup with 20% porosity and 10^{-4} Darcy permeability is the basis for all experiments. The model has a size of 10x10x10 m, which yields a shape factor of 0.12 m^{-2} when using the KGE shape factor definition. All calculations were performed for a period of 15 years. The matrix can be bounded at all sides or only in vertical direction with fractures, where either a constant pressure or a constant pressure drop rate is imposed as boundary conditions. Viscous forces are neglected to enable calculations on a quarter-block model.

Two PVT data sets, presented in Table 4.1, and two sets of rock-functions are used. Each rock-function set consists of capillary pressure- and relative permeability data. Figure 4.2 shows the data for rock region no.1, which is strongly oil wet. Rock data set no.3. is water wet and is shown in Figure 4.3. Rock data sets no.9 and 10 have the same relative permeability functions as the sets no.1 and 3, but the capillary pressures are equal to zero. Different combinations of PVT and rock-function sets are considered.

The calculated setups are summarized in Table 4.2. Differences are in ROCK and PVT region, in fracture configuration, in the initial pressure and in allowing phase segregation or not. The pressure decline rate, if defined, is constant 0.05 or in one case -0.01 bar/day, which means that the pressure is increasing. Setups 1 to 8 deal with expansion and solution gas drive. Setups 9 to 24 test oil displacement by water or gas for different conditions with regard to pressure decline rates, initial pressure, phase segregation and fracture configuration. Setups 25 to 28 have changes of drive mechanisms, displacing oil with water from previously gas-flooded matrix

blocks and vice versa.

For all cases the apparent shape factor was calculated.

Table 4.1: Fluid properties of the 1st and 2nd PVT data set

Property	PVT data 1	PVT data 2
Reservoir Temperature [°C]	93.3	44.2
Bubble Point Pressure, p_b [bar]	276.8	155
Water Density [kg/m^3]	1037.5	1094
Oil Density [kg/m^3]	786.5	793.8
Gas Density [kg/m^3]	1.025	0.788
Reference Pressure, p_{ref} [bar]	330.9	168.9
Water Viscosity at p_{ref} [cP]	0.31	0.854
Water Formation Volume Factor at p_{ref} [rm^3/sm^3]	1.0213	1.01
Water Compressibility at [1/bar]	4.51E-05	2.35E-06
Oil Viscosity at p_b [cP]	0.51	0.4819
Oil Formation Volume Factor at [rm^3/sm^3]	1.695	1.259
GOR at pb [sm^3/sm^3]	214.6	111.4
Gas Viscosity at pb [cP]	0.0268	0.0181
Z-factor at pb [-]	0.9799	0.717

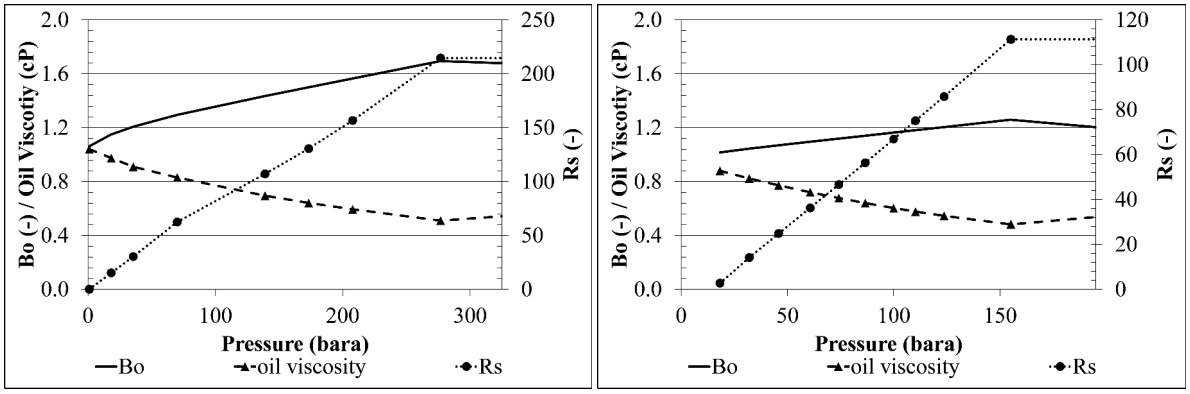

Figure 4.1: Oil formation volume factor (B_o), oil viscosity and solution gas ratio (R_s) for PVT data set 1 (left) and PVT data set 2 (right)

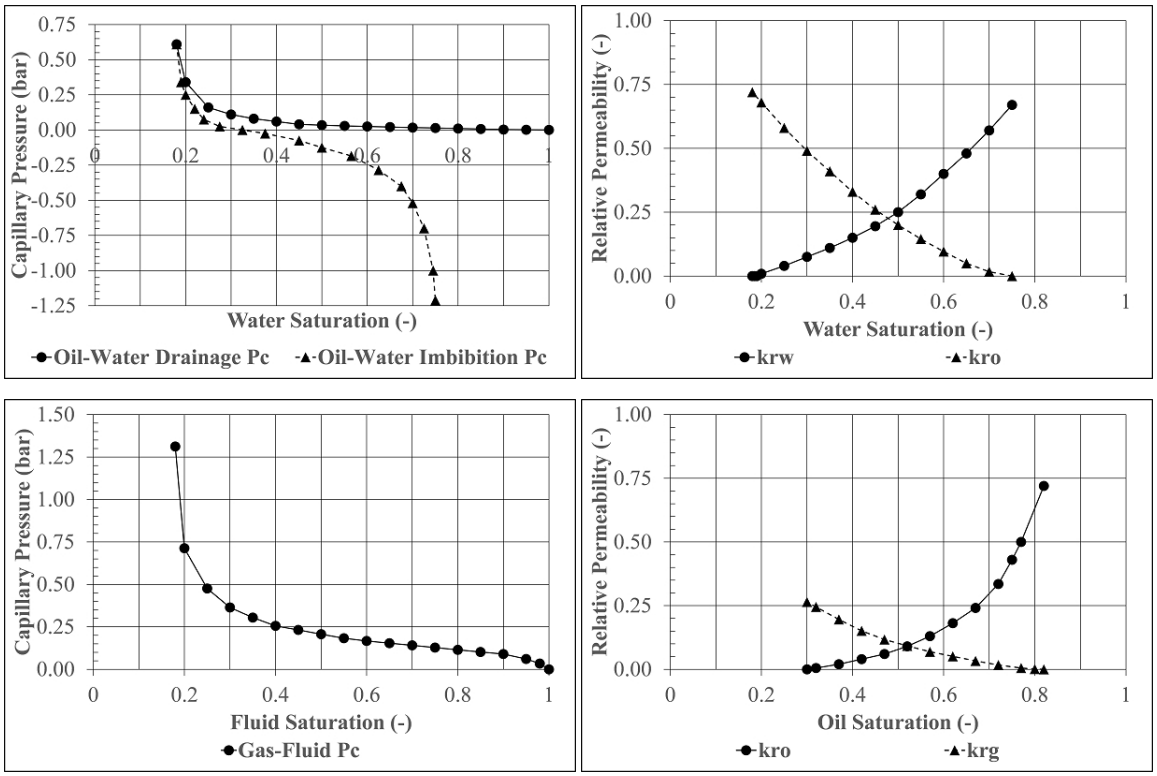

Figure 4.2: Capillary pressure and relative permeability functions of the oil wet data set no. 1. (Steiner and Mittermeir 2017)

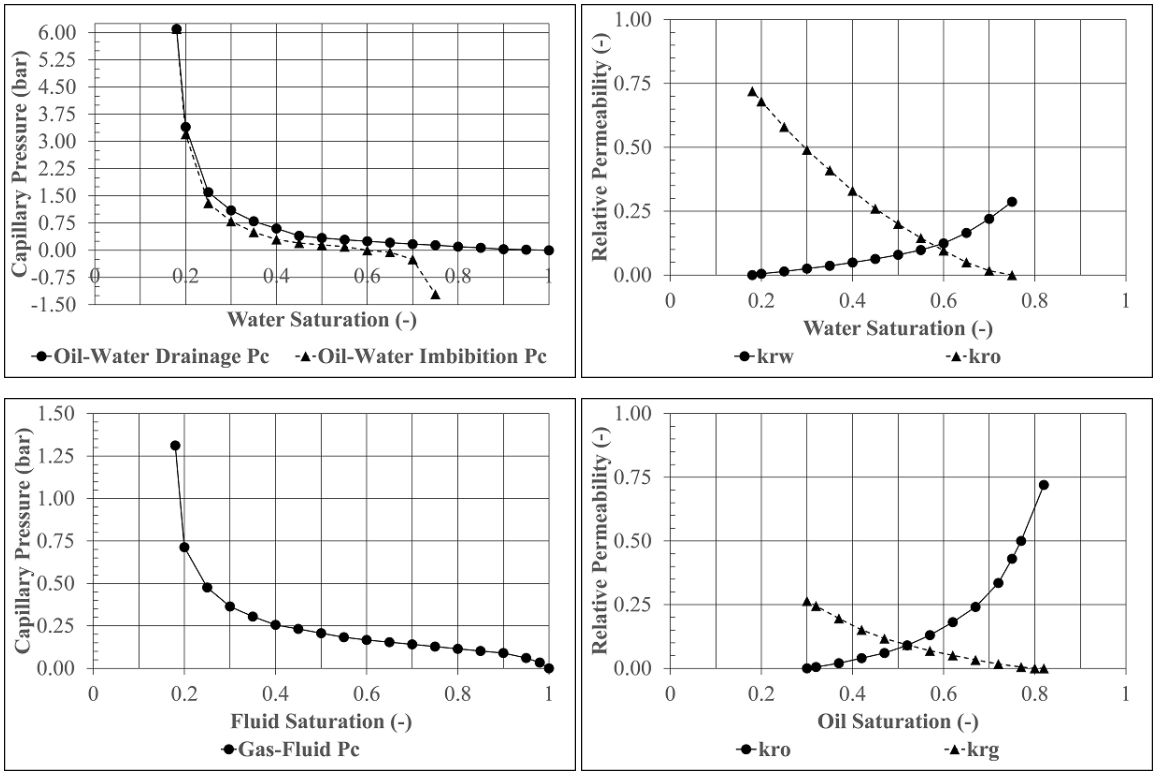

Figure 4.3: Capillary pressure and relative permeability functions of the water wet data set no. 3. (Steiner and Mittermeir 2017)

Table 4.2: SMB Setups

Run Sno.	Rock Reg. Sno.	PVT Region Sno.	Capillary Pressure	Wettability	Drive Mechanism	Fracture Configuration	Phase Segregation	Initial Pres. (bar)	Pres. Decline Rate (bar/day)
1	1	1	N	n.a.	E	VO	Y	330	0.05
2	1	1	N	n.a.	E	VO	N	330	0.05
3	1	1	N	n.a.	E	AS	Y	330	0.05
4	1	1	N	n.a.	E	AS	N	330	0.05
5	1	2	N	n.a.	E	VO	Y	280	0.05
6	1	2	N	n.a.	E	VO	N	280	0.05
7	1	2	N	n.a.	E	AS	Y	280	0.05
8	1	2	N	n.a.	E	AS	N	280	0.05
9	1	1	N	n.a.	W	AS	Y	330	0.00
10	1	1	N	n.a.	G	AS	Y	277	0.00
11	1	1	Y	ow	W	AS	Y	277	0.00
12	1	1	N	n.a.	G	AS	Y	277	-0.01
13	3	1	N	n.a.	W	AS	Y	330	0.00
14	3	1	N	n.a.	G	AS	Y	330	0.00
15	3	1	Y	ww	W	AS	Y	330	0.00
16	3	1	Y	ww	G	AS	Y	330	0.00
17	1	1	N	n.a.	W	AS	Y	330	0.05
18	1	1	N	n.a.	G	AS	Y	330	0.05
19	1	1	Y	ow	W	AS	Y	330	0.05
20	3	1	Y	ww	G	AS	Y	277	0.05
21	3	1	N	n.a.	W	AS	Y	330	0.05
22	3	1	N	n.a.	G	AS	Y	330	0.05
23	3	1	Y	ww	W	AS	Y	277	0.05
24	3	1	Y	ww	G	AS	Y	330	0.05
25	3	1	Y	ww	E/W	AS	Y	330	0.05
26	3	1	Y	ww	E/G	AS	Y	330	0.05
27	1	1	Y	ow	W/G	AS	Y	330	0.05
28	1	1	Y	ow	G/W	AS	Y	330	0.05

Abbreviation	Meaning
Sno.	serial number
Y	yes
N	no
n.a.	not applicable
ww	waterwet
ow	oilwet
E	expansion drive
W	water drive
G	gas drive
VO	vertical only
AS	all side

4.2 The Reiss at al. Approach

Kazemi at al. (1992) stated that the exponential constant λ in the equation of Aronofsky (1958):

$$E_R(t) = E_{R,\,max}(1. - e^{-\lambda t}) \tag{4.1}$$

should be considered purely as a curve fitting parameter and no physical meaning should assigned to it. Another potentially useful empirical function other than Equation 4.1 for fitting cumulative recovery data was suggested by Kazemi, Gilman and Elsharkawy (1992) also:

$$E_R(t) = E_{R,\,max} - E_{R1}e^{-\lambda_1 t} - E_{R2}e^{-\lambda_2 t} - \ldots \tag{4.2}$$

where $E_{R,\,max} = E_{R1} + E_{R2} + \ldots$

One parameter is valid for a given single recovery process. Therefore, such a function cannot be used to model complex schemes as e.g. water-alternating-gas.

For SMB setup 1 parameters E_{Rmax} and λ for matching the RC cannot be determined. As can be seen in Figure 4.4, the ultimate recovery is correct but it is impossible to find a constant λ for matching the recovery factor for all times before the ultimate recovery is reached.

For SMB setup 19 two exponential functions have been determined, one describing the early and the other one the late time behavior (Figure 4.5). For the early time the pressure is still above the bubble point pressure and parameters can be found that result in a good fit. When the pressure further drops also solution gas drive occurs and this cannot be described with the early time match. A second function for this part is able to match the late time behavior, but it underpredicts the early time speed of recovery.

Also for SMB setup 24 two functions, one for the early and the other one for the later part can be found (Figure 4.6). However, as for setup 19, the early time matched function is not suitable to estimate the speed of recovery for the late time and vice versa.

The results of the SMB calculation show, that it is not possible to define the recovery factor as a function of time, e.g. using an exponential function (Aronofsky, 1958) or a square root function (Rangel-German and Kovscek 2000). Also, as shown by Rangel-German and Kovscek (2002) the oil recovery function has a different shape, ranging from a linear function to a square root function, depending e.g. on matrix-fracture fluid transfer rate and fracture aperture.

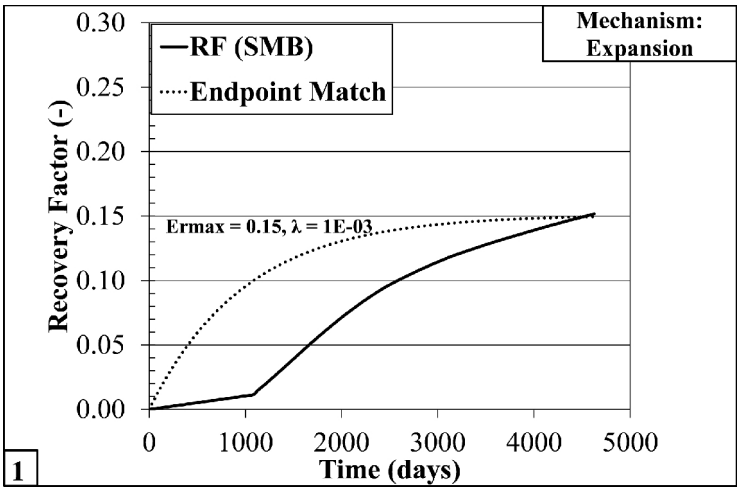

Figure 4.4: Expansion Drive, Setup 1

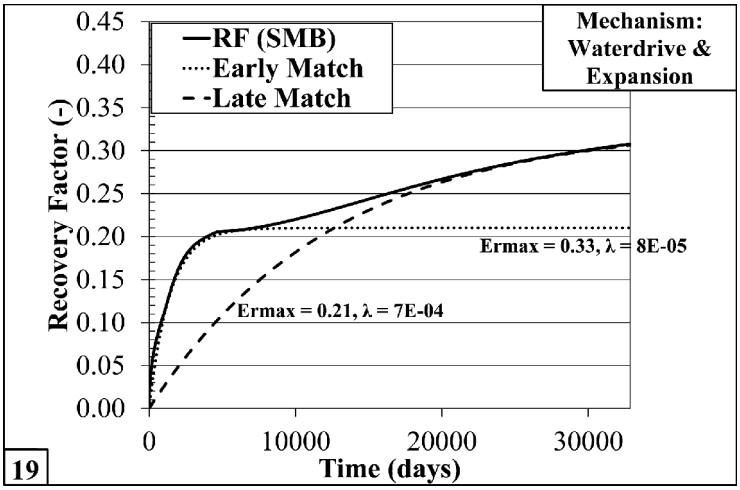

Figure 4.5: Waterdrive with expansion, Setup 19

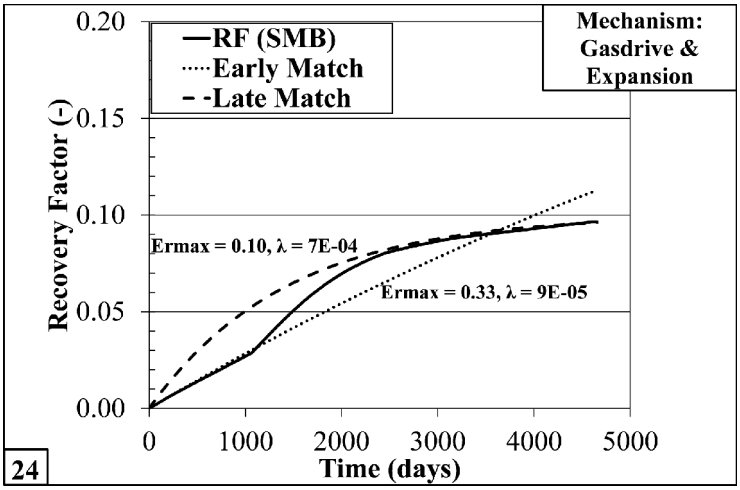

Figure 4.6: Gasdrive with expansion, Setup 24

4.3 The Kazemi et al. Approach

Based on the derivation of the shape factor by Heinemann and Mittermeir (2012), the Kazemi et al. (1976) transfer equation

$$q_{cmf} = V_{bulk}\sigma k_a \sum_p \frac{k_{rp}}{\mu_p B_p}(\Phi_{pf} - \Phi_{pm}) \quad , p = w, o, g \,, \tag{4.3}$$

is valid and the shape factor is a constant if the following conditions are assured: (1) the matrix block is homogenous and the saturation in it is uniform, (2) the pressure distributions between the midpoint and the side surfaces are linear (3) the average pressure in the matrix block is a good approximation for its midpoint pressure, (4) the fracture pressure at the matrix block boundaries are uniform (identical).

It must be clear that these conditions can only be more or less, but never completely satisfied. Therefore, the applicability of the transfer equation for specific cases would need experimental verification. What the literature provides in this respect is more than limited. In any case, the feasibility of relevant experiments is questionable. An overview of the available literature can be found above.

Theoretically, the shape-factor is dependent on the geometry of the matrix block, but independent of time or recovery process. Consequently, after establishing pseudo-steady state flow conditions, constant shape factors are the prerequisite when the Kazemi et al. (1976) transfer function is applied. In lack of experimental results representative of reservoir matrix blocks in terms of size and time of evaluation, numerical experiments on a fine grid SMB model are the only option for testing the applicability of the transfer function.

The SMB calculation provides the matrix mid-point and the average pressures, the average matrix saturations and therefore also the average relative permeabilities. The average oil rate from the matrix are calculated for every time point:

$$q_{omf} = \frac{RF(t + \Delta t) - RF(t - \Delta t)}{2\Delta t} \cdot OOIP \,. \tag{4.4}$$

Based on matrix properties, the apparent shape factor is calculated by rearranging the fracture-matrix transfer equation:

$$\sigma = \frac{\mu_o B_o q_{omf}}{V_{bulk} k_a k_{ro} (\Phi_{om} - \Phi_{of})} \,, \tag{4.5}$$

where the viscosity μ and the formation volume factor B_o are evaluated at the average matrix pressure and the relative permeability k_r at the average saturation. The potential difference is calculated as follows:

$$\Phi_{om} - \Phi_{of} = p_{om} - p_{of} + P_{c,ow} + P_{c,og} + \kappa P_{hwof} + \kappa P_{hogf} \tag{4.6}$$

where κ is ¼ and the terms P_{hwof} and P_{hogf} are the potential differences stemming from difference of the pressure gradients in the fracture and in the matrix. $P_{c,ow}$ and $P_{c,og}$ are the potential differences originating from the capillary pressures for the oil-water and oil-gas case, respectively. When the fracture is filled with gas P_{howf} and $P_{c,ow}$ is zero and when it is filled with water P_{hogf} and $P_{c,og}$ is zero. For evaluating the potential difference, there are two possibilities: firstly, using the midpoint and secondly the average matrix pressure. Average and midpoint matrix pressures are usually different, unless the SMB model is operated at constant pressure.

4.3.1 Results

4.3.1.1 Summary

For all cases the apparent SF was calculated as function of time based on Equation 4.5 using both the midpoint and the average matrix pressures. The results are summarized in Table 4.3, which informs about minimum, maximum and average values.

Setups, where only expansion and solution gas drive occurs, show a similar apparent shape factors. When calculated using the center point pressure, the value is also near the theoretical value of 0.12 m^{-2}, when calculated with the KGE definition. For all other drive mechanisms and combinations of them, the shape factors are never constant and also not at the nominal value of 0.12 m^{-2}.

A detailed description of all results can be found below.

Table 4.3: Results of the SMB calculations

Run Sno.	Shape Factor (Avg. Matrix Pres.) [m^{-2}]			Shape Factor (Matrix Pres. at Center Point) [m^{-2}]			Drive Mechanism
	minimum	maximum	average	minimum	maximum	average	
1	0.205	0.233	0.211	0.110	0.115	0.114	E
2	0.205	0.233	0.211	0.101	0.115	0.114	E
3	0.258	0.275	0.269	0.126	0.138	0.135	E
4	0.204	0.206	0.205	0.101	0.115	0.114	E
5	0.207	0.211	0.209	0.112	0.116	0.115	E
6	0.207	0.211	0.209	0.109	0.116	0.115	E
7	0.277	0.316	0.289	0.138	0.146	0.140	E
8	0.205	0.207	0.206	0.109	0.116	0.115	E
9	0.040	0.061	0.050	0.040	0.066	0.052	W
10	0.040	0.085	0.063	0.041	0.095	0.067	G
11	0.039	0.085	0.048	0.035	0.095	0.043	W
12	0.041	0.131	0.085	0.041	0.156	0.094	G
13	0.040	0.062	0.051	0.040	0.069	0.054	W
14	0.039	0.074	0.054	0.039	0.079	0.056	G
15	0.010	0.022	0.012	0.010	0.022	0.012	W
16	0.037	0.048	0.043	0.036	0.048	0.042	G
17	0.020	0.082	0.043	0.013	0.066	0.033	W
18	0.048	0.124	0.098	0.045	0.087	0.074	G
19	0.011	0.127	0.028	0.007	0.123	0.022	W
20	0.013	0.075	0.028	0.008	0.059	0.022	G
21	0.020	0.082	0.043	0.014	0.067	0.033	W
22	0.048	0.124	0.098	0.045	0.087	0.074	G
23	0.001	0.118	0.006	0.001	0.086	0.006	W
24	0.012	0.061	0.029	0.009	0.048	0.024	G
25	0.003	0.275	0.080	0.003	0.136	0.042	E/W
26	0.003	0.275	0.143	0.002	0.136	0.075	E/G
27	0.011	0.127	0.028	0.009	0.123	0.023	W/G
28	0.013	0.118	0.030	0.009	0.109	0.025	G/W

4.3.1.2 Expansion Drive

All expansion drive examples with sno. 1-8 show nearly constant shape factors throughout the calculation. When the bubble point pressure is reached slight deviation of less than 0.03 m^{-2} can be seen for examples 1, 2, 3, 7 and 8. When considering the midpoint pressure, the average shape factor values vary between 0.114 m^{-2} for sno. 1, 2 and 4 and 0.140 m^{-2} for sno. 7. The differences between the numerically derived SF and the nominal value of 0.12 mm^{-2} calculated with the KGE definition is caused by the slight non-linearity of the matrix pressure distribution.

Otherwise the following conditions, requested by the Heinemann and Mittermeir transfer model, are nearly perfectly satisfied (Heinemann and Mittermeir 2014):

- (*Uniform boundary conditions:* The fracture is filled by oil and no flow takes place in it. Therefore, the potential in the boundary is uniform.

- *Uniform properties:* The matrix contains a single movable fluid and so the fluid and rock parameters are within the matrix uniform

- *Semi-state-flow:* The pressure in the boundary will be reduced, inducing pressure drop within the matrix. The matrix pressure is initially uniform therefore at the beginning the flow is transient. The length of the transient period depends on the matrix block size and on the permeability. This is shown in Section 4.3.2. After the transient period the flow is semi-steady state and the matrix-fracture pressure difference becomes nearby time independent.

- *Linearity in potential gradient*)

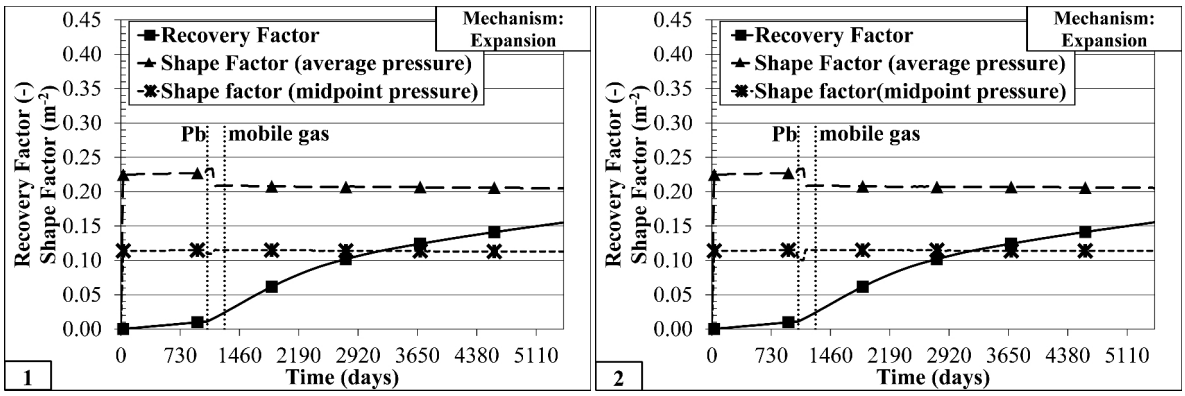

Figure 4.7: SMB experiments 1 (left) and 2 (right) (Steiner and Mittermeir 2017)

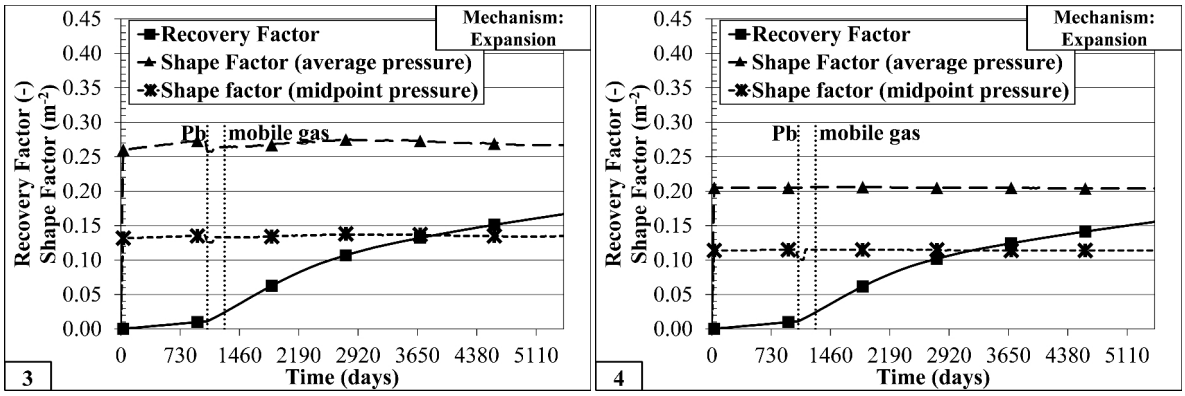

Figure 4.8: SMB experiments 3 (left) and 4 (right)

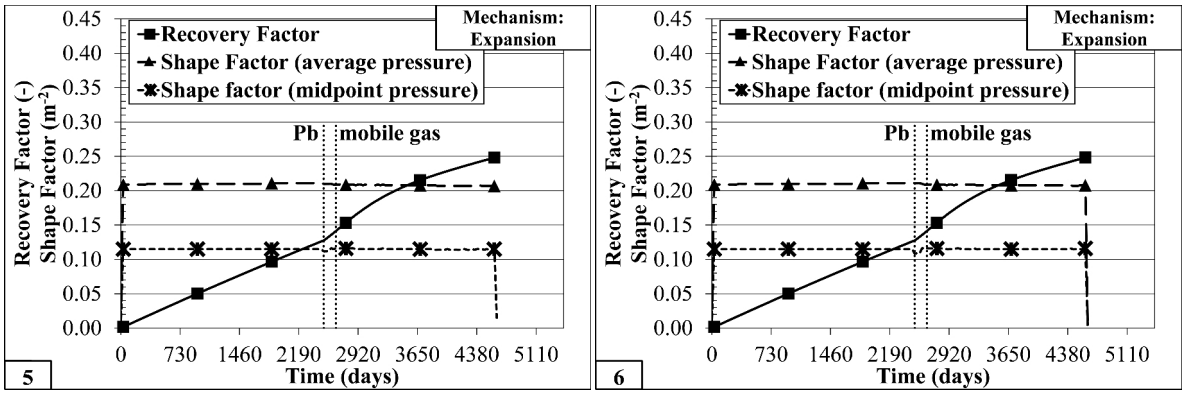

Figure 4.9: SMB experiments 5 (left) and 6 (right) (Steiner and Mittermeir 2017)

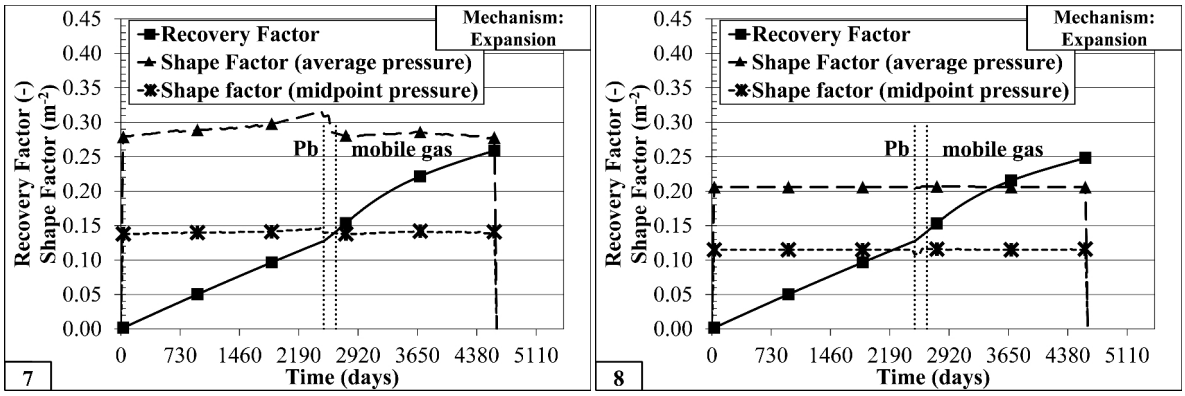

Figure 4.10: SMB experiments 7 (left) and 8 (right)

The KGE shape factor can be reproduced using the SMB calculation when the midpoint pressure is used, but it is approximately double when the average pressure is used for the calculation. When implemented in a DCM, only the average pressure is determined and the midpoint pressure is unknown. Aso in the literature publications deriving increased shape factors can be found. Zimmerman et al. (1993), Chang (1993), Kazemi and Gilman (1993) and Lim and Aziz (1995) analytically derived that the coefficient of 4 in the shape factor definition of Kazemi et al. (1976) should be replaced by π^2, which is an increase by more than a factor of two.

4.3.1.3 Gas- or Waterdrive at Constant or With Increasing Pressure

Setups 9 and 10, shown in Figure 4.11, are waterdrive and gasdrive at constant pressure and without considering capillary pressure. For both cases the recovery factor increases nearly linearly and also the SF is increasing. It can also be seen that the SF values are different for waterdrive and gasdrive. As the difference between average pressure and pressure at the midpoint is only very small, the SF based on average and midpoint pressure are also nearly identical. The average pressure is only slightly different to the midpoint pressure because the phases distributed non-uniformly within the SMB and therefore the pressure gradient within the SMB is also not symmetrical around the center cell.

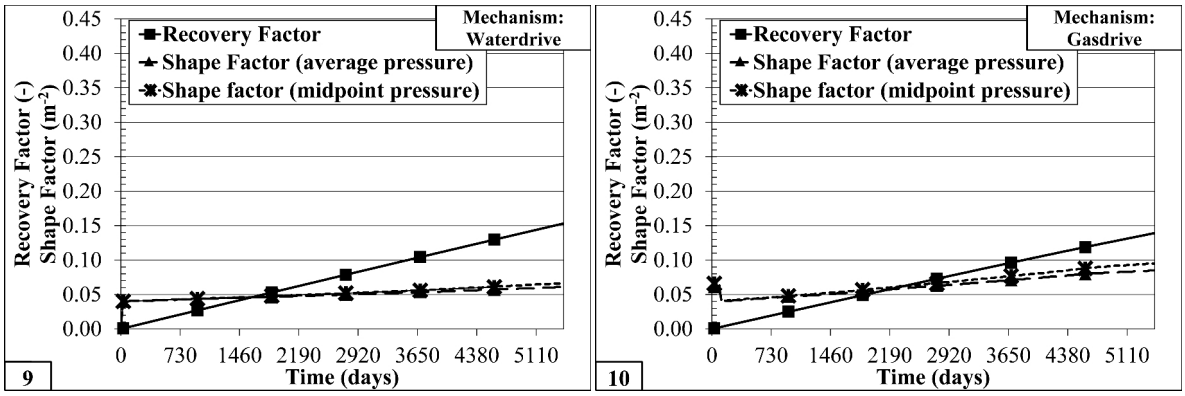

Figure 4.11: SMB experiments 9 (left) and 10 (right) (Steiner and Mittermeir 2017)

Setup 11 (Figure 4.12, left) is identical to setup 9, but capillary pressure is considered. The development of the RF is not linear but approximates the shape of a square-root function. The calculated SF are high in the beginning and then decreasing strongly. In the late time the SF starts to slowly increase again. Again there is nearly no difference between average pressure and midpoint pressure based SF, since the pressure remains constant. Setup 12 (Figure 4.12, right), which is identical to setup 10, but with increasing pressure, shows again a linear increase of the RF. The SF increases during the calculation and this increase is stronger than in setup 10.

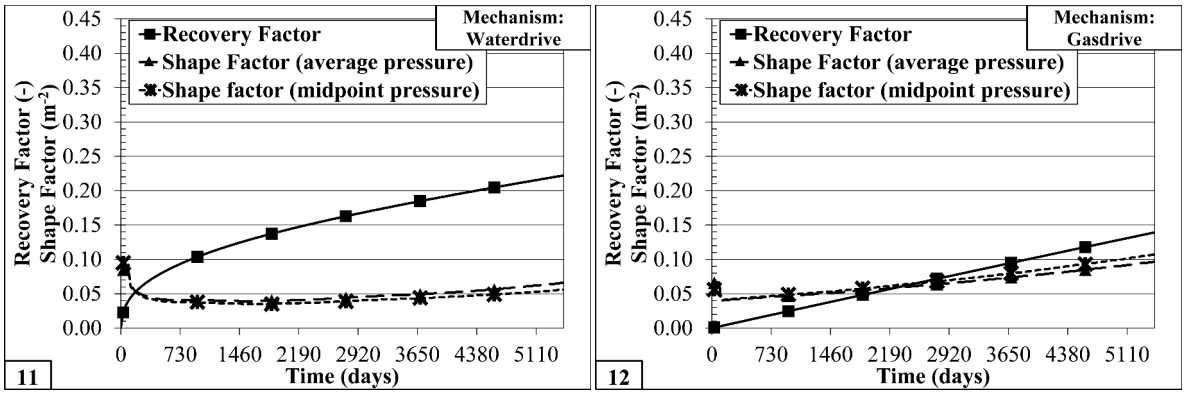

Figure 4.12: SMB experiments 11 (left) and 12 (right) (Steiner and Mittermeir 2017)

In setups 13 and 14 (Figure 4.13) the matrix is considered to be water-wet and the pressure is constant. In both cases the RF and SF show a nearly linear increase from the start until the end.The two setups are identical with the exception of the driving force. The SF values are similar for waterdrive and gasdrive, but not identical.

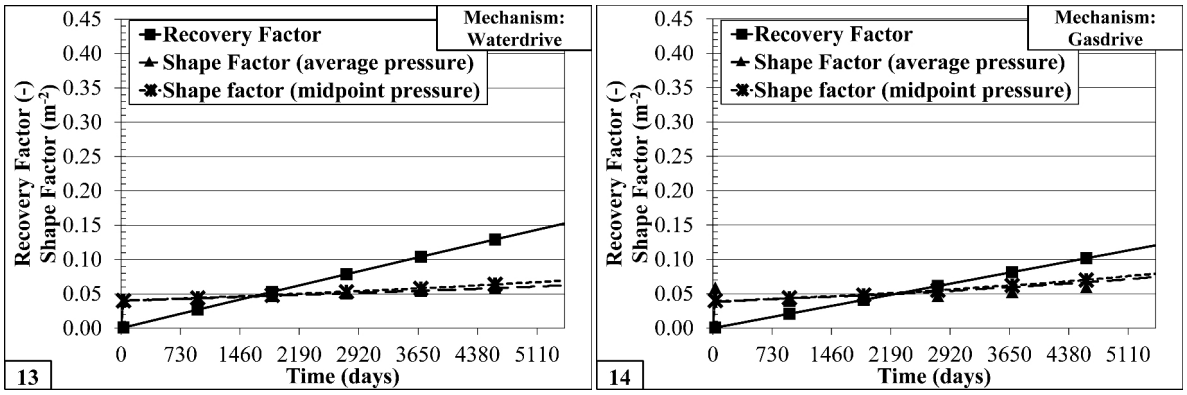

Figure 4.13: SMB experiments 13 (left) and 14 (right) (Steiner and Mittermeir 2017)

Setups 15 and 16 (Figure 4.14) are identical to setups 13 and 14, but capillary pressures are considered. For waterdrive this results in a RC that is not linear. The SF for setup 15 is much lower than for setup 13, which is without capillary forces. In setup 16 the SF is also not constant and does not exhibit the slight increase over time as seen in setup 14. At late time the SF decreases for setup 16, resulting in a SF of approximately half the SF of setup 14 at the end of calculation.

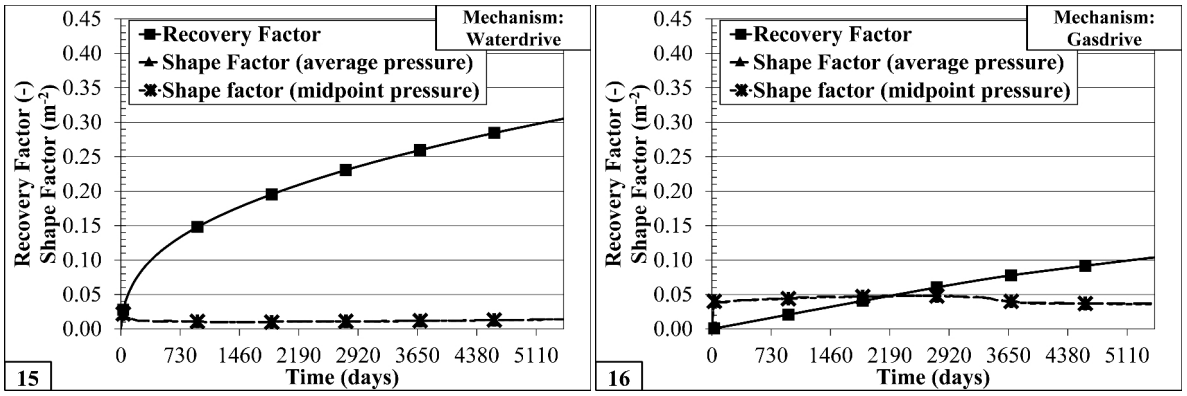

Figure 4.14: SMB experiments 15 (left) and 16 (right) (Steiner and Mittermeir 2017)

Generally, for constant pressure or slightly increasing pressure water- or gasdrive, the calculated SFs are neither equal for waterdrive and gasdrive nor constant.

4.3.1.4 Gas- or Waterdrive With Decreasing Pressure

Setups 17 and 18 (Figure 4.15) are identical, with the exception of the driving force. It can be

seen, that as long as the bubble point pressure P_b is not reached, both setups show a similar behavior than the ones where the pressure is constant. After reaching P_b the slope of the RC increases instantaneously. The SF also increases at the same time, but not identically for waterdrive and gasdrive. In setup 17 the SF decreases afterwards, whereas in setup 18 this cannot be observed. Also the difference between the SF based on midpoint and average pressure is significant for both setups and more distinct in setup 18.

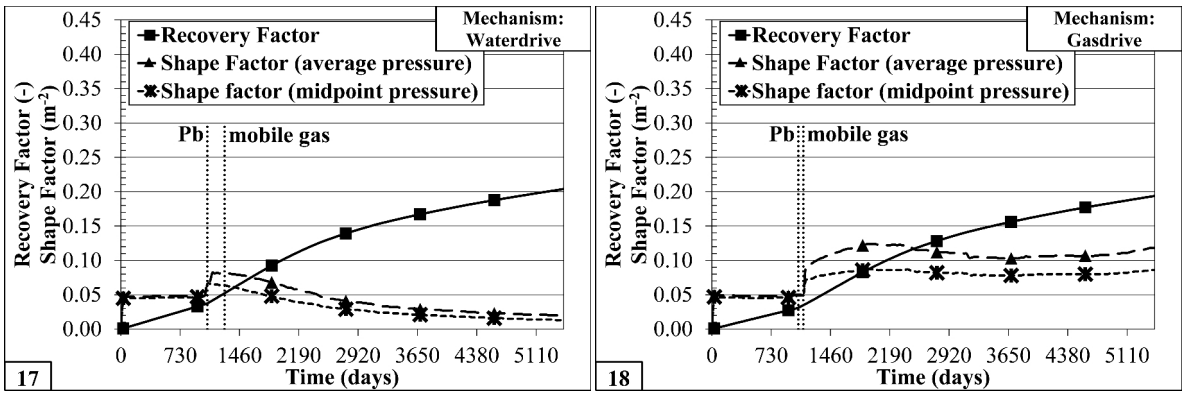

Figure 4.15: SMB experiments 17 (left) and 18 (right) (Steiner and Mittermeir 2017)

Setup 19 (Figure 4.16, left), which is waterdrive using oil-wet rock data, has a RC that is neither linear nor has a square-root function shape. The SF decreases rapidly in the early time and remains relatively constant until the P_b is reached. After the average gas saturation in the SMB is higher than the critical gas saturation, the SF starts to constantly decrease until the end of calculation. Setup 20 (Figure 4.16, right), which is gasdrive and is considering capillary pressure, starts its calculation at P_b, therefore the time when P_b is reached is not shown in the figure. The SF decreases until approximately day 2000 and then increases slightly until the end of calculation. The SF based on average pressure and midpoint pressure shows differences until day 2000.

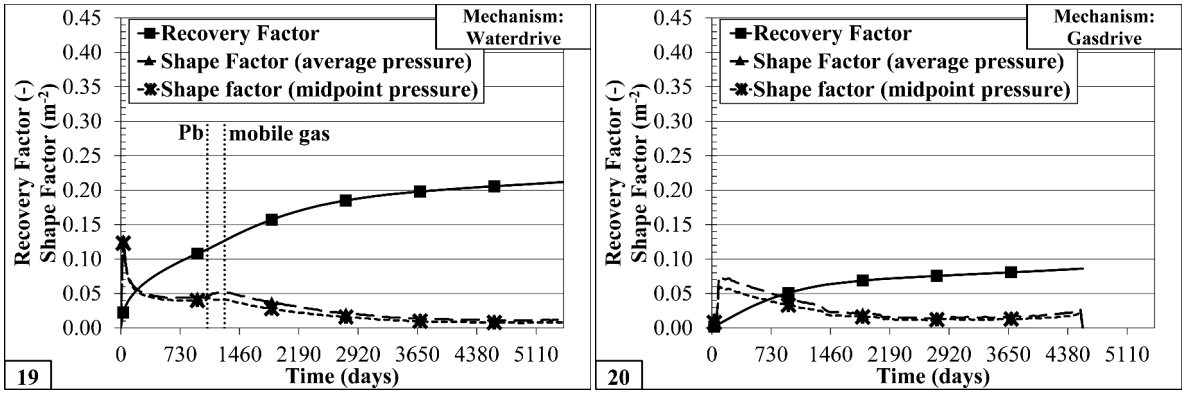

Figure 4.16: SMB experiments 19 (left) and 20 (right) (Steiner and Mittermeir 2017)

Setups 21 and 22 (Figure 4.17) are identical, except for the drive mechanism. It can be seen that for both setups the slope of the RC changes significantly when the bubble point is reached. Because of the combination of solution gas drive with water-/gasdrive the RC is not linear

afterwards, even tough no capillary forces are considered. When P_b is reached the SF increases instantaneously and the SF based on average and midpoint pressure separate for both setups. However, for setup 21 the SF decreases afterwards, for setup 22 it remains relatively constant.

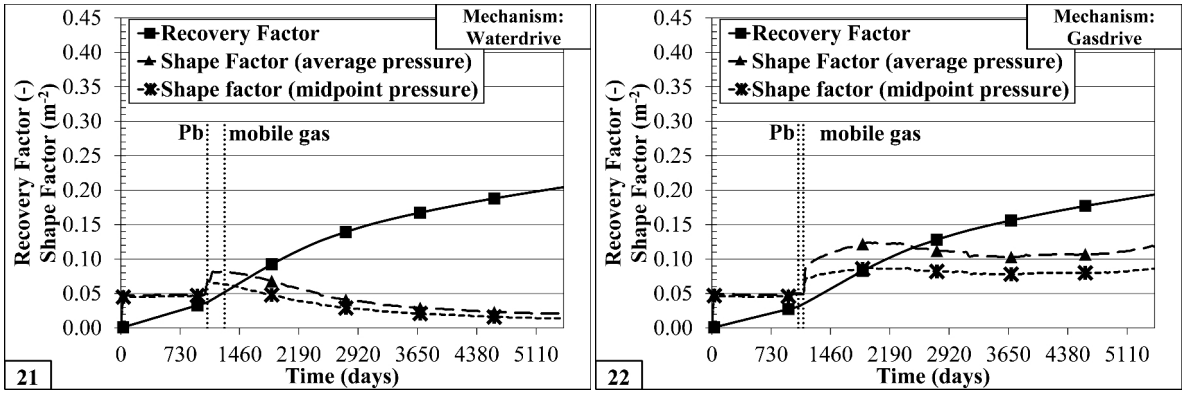

Figure 4.17: SMB experiments 21 (left) and 22 (right) (Steiner and Mittermeir 2017)

Setup 21 (Figure 4.18, left) uses the water-wet rock data and starts directly at Pb, therefore Pb is not marked in the figure. In this case the RC shows the form of an exponential function. The SF drastically decreases in the beginning at remains at a very low level throughout the calculation. Setup 22 (Figure 4.18, right) also uses the water-wet rock data, but the calculation starts above bubble point and the driving mechanism is gasdrive. Until Pb is reached, the RF increases linearly and the SF remains nearly constant. After PB is reached the slope of the RC changes and it is not longer linear. The SF decreases and shows differences between the midpoint and average pressure after the average gas saturation in the matrix is above the critical gas saturation.

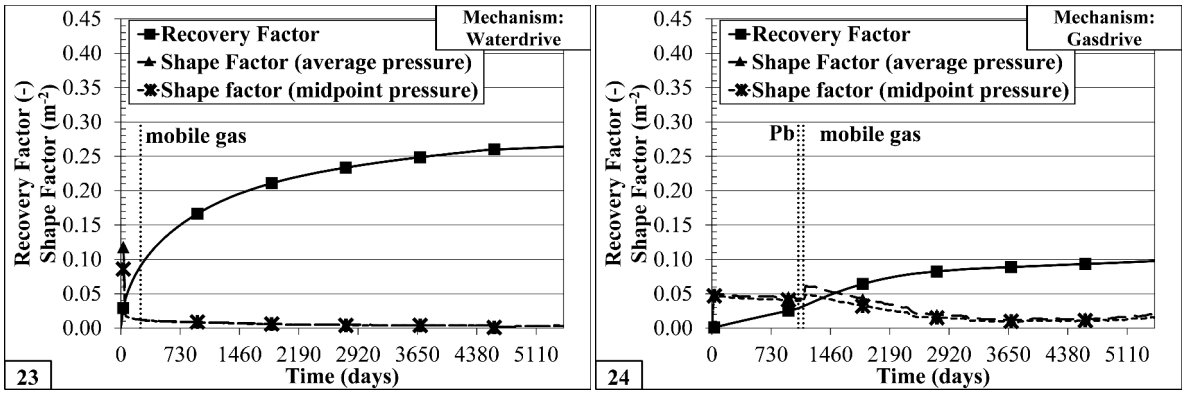

Figure 4.18: SMB experiments 23 (left) and 24 (right) (Steiner and Mittermeir 2017)

Generally, for the scenarios of combined expansion or solution-gas drive with water-/ or gasdrive, the SF is neither constant nor at the nominal value of 0.12 m-2. Also differences between the average and midpoint pressure based SF arise. The deviation from a constant SF value is also not the same for all experiments, which would make a common correction for all driving mechanisms in form of a time-dependent shape-factor impossible.

4.3.1.5 Changing Drive Mechanisms

Setup 25 (Figure 4.19, left) is expansion and solution-gas drive followed by waterdrive using the water-wet rock data. Three phases can be identified. In the first on only expansion occurs without above Pb. In this phase the RF increases linearly and the SF based on midpoint pressure is approximately equal to the nominal value of 0.12 m-2. In phase two, between the time when Pb is reached and the time when waterdrive starts, solution-gas drive occurs and the slope of the RC increases. For a short time also the SF shows a fluctuation but then remains constant again at the nominal value. Phase three starts with the beginning of the waterdrive. This is marked by a sharp increase in the slope of the RC and a strong decrease of the SF value.

Setup 26 (Figure 4.19, right) is identical to setup 25, with the exception that instead of waterdrive gasdrive is activated after expansion and solution-gas drive. Until gasdrive starts also the RC and the SF is identical to setup 25. However, as soon as gasdrive starts, the slope of the RC decreases. The SF decreases, but not as much as for the change to waterdrive.

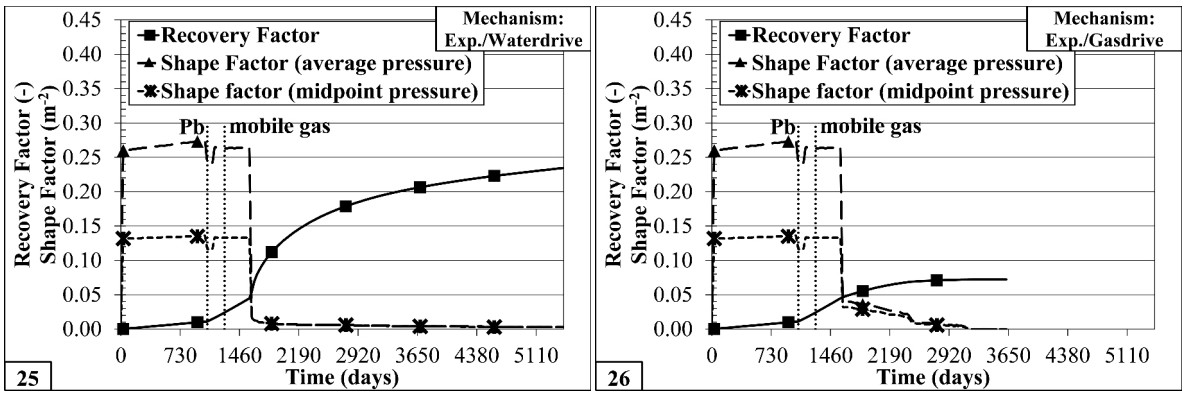

Figure 4.19: SMB experiments 25 (left) and 26 (right) (Steiner and Mittermeir 2017)

Setup 27 (Figure 4.20, left), is waterdrive followed by gasdrive in combination with expansion and solution-gas drive. In this case the oil-wet rock data is used. The drive-mechanism changes after 1612 days, where a decrease in the slope of the RC can be observed. The SF decreases in the beginning and remains roughly constant until the drive mechanism changes.

Setup 28 (Figure 4.20, right) is identical to setup 27, but in this case gasdrive is followed by waterdrive. The change in drive-mechanism occurs also after 1612 days, where an increasing slope of the RC can be seen and a spike in the calculated SF.

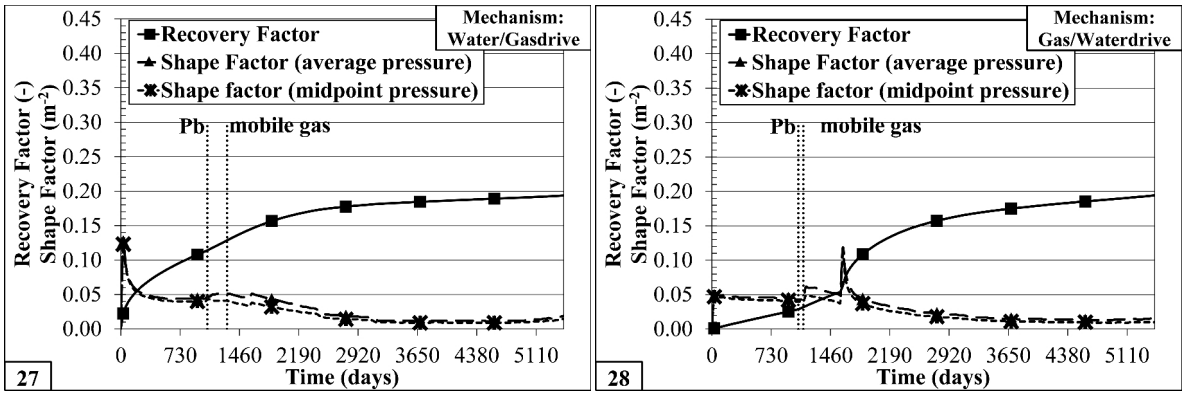

Figure 4.20: SMB experiments 27 (left) and 28 (right)

4.3.2 Transient Effects

Transient effects can be observed in the calculation when either the temporal resolution is very high or the speed of the recovery process is very low, which can be achieved with a low permeability. To show the impact of the permeability on the calculated shape factor SMB experiments with permeabilities varying between 10-9 D to 10-4 D are created. PVT data set no. 1 and the ROCK functions no. 1 are used, the matrix block has a dimension of 10x10x10 m and the drive mechanism is expansion only. The initial pressure is 380 bar and with a constant decline rate of 0.04 bar/day the pressure reaches the defined minimum pressure of 280 bar after 2526 days. The results of the experiments can be seen in Figure 4.21. The apparent shape factor, which is calculated using the midpoint pressure of the matrix, is expected to be constant during the calculation. For very low permeabilities (10^{-9} D, 10^{-8} D, 10^{-7} D) the shape factor is not constant due to transient effects. For permeabilities greater than 10^{-6} D the transient effects cannot be observed and are negligeable.

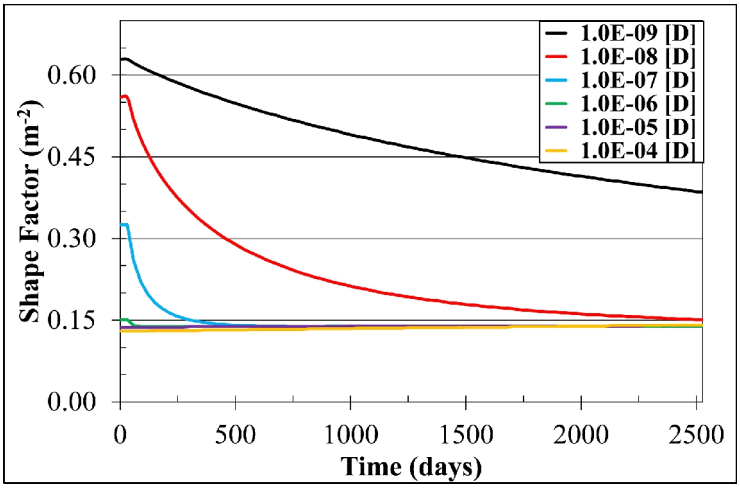

Figure 4.21: Impact of matrix permeability on the shape factor

The transient pressure behaviour inside the SMB can be seen in Figure 4.22. There the

horizontal pressure distribution for the case with a permeability of 10^{-7} D is shown for different times. It is evident that the distribution is not linear. Figure 4.23 shows for the same SMB model a plot of shape factor and pressure decline rate at the matrix midpoint versus time. As long as the pressure decline is in the transient phase the shape factor is not constant. When the pseudo-steady state regime, marked by a constant pressure decline rate also at the midpoint, starts, the shape factor is constant from this point forward.

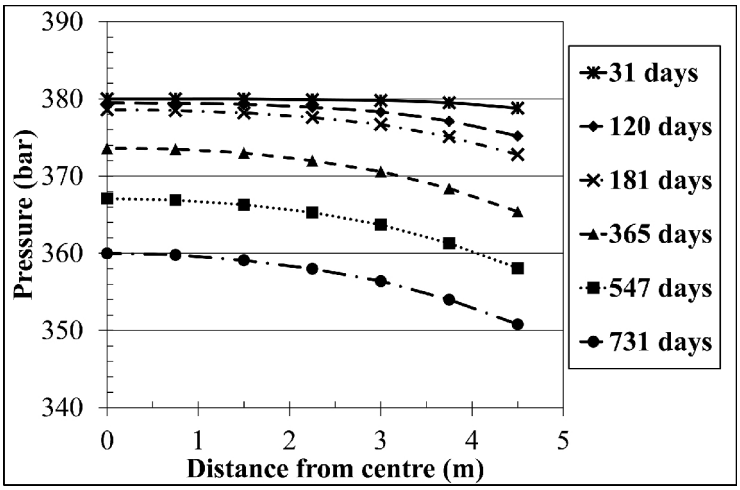

Figure 4.22: Horizontal pressure distribution at different times (10^{-7} D permeability) (Steiner and Mittermeir 2017)

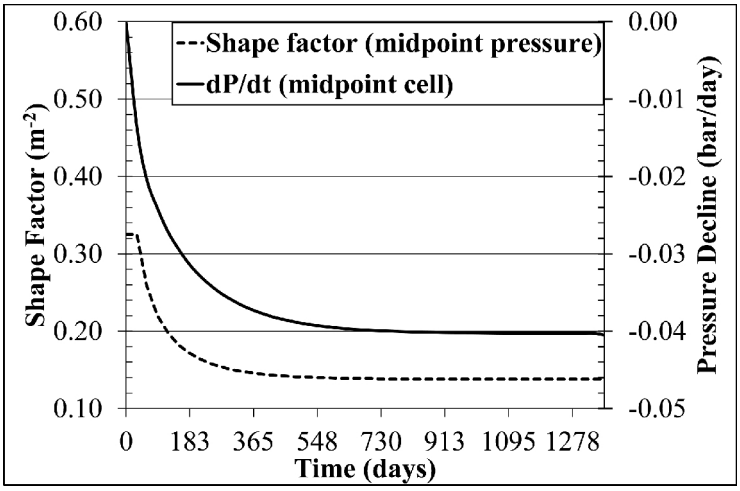

Figure 4.23: Pressure-time derivative and shape factor as a function of time. (Steiner and Mittermeir 2017)

Chapter 5

The Recovery Curve Method

The Recovery Curve Method (RCM) is based on the concept suggested by Heinemann (2004). Since then this concept has been applied to material balance calculations (Mittermeir 2015) and also numerical models (e.g. Pirker 2008, Heinemann and Mittermeir 2016). In this chapter a RCM, used for numerical models will be presented, which uses scaled RCs for the determination of the matrix-to-fracture mass transfer. Also non-uniform saturation boundary conditions and oil-resaturation will be discussed.

5.1 Inter-Porosity Molar Flux

Generally, the inter-porosity molar flux of component *c* for one cell is:

$$q_{cmf}^{n+1} = \tau_{mf} \sum_{p=1}^{P} (\lambda_p D_p x_{pc})_{mf}^{n+1} (\Phi_{pm} - \Phi_{pf})^{n+1} + \delta_{mf} \sum_{p=1}^{P} [D_{pc} (S_p D_p)_m^{n+1} (x_{pcm} - x_{pcf})^{n+1}] \tag{5.1}$$

where *n* denotes the sno. of the time step, λ_p is the phase mobility, Φ_p is the phase potential, x_{pc} is the mole fraction of component c in phase p, D_p is the specific mole density, τ_{mf} is the interblock transmissibility, δ_{mf} is the matrix-fracture transmissivity and S_p is the phase saturation. When the RCM is applied, the term $q_{p,fm}$ is calculated using the RC time derivative, providing the injection rate for phase *p*. The phase potentials Φ_{pm} and Φ_{pf} do not consider capillary pressures or gravitational forces, as they are already accounted for in the RC. Diffusion is already included in the RC:

$$q_{cmf}^{n+1} = \tau_{mf} \sum_{p=1}^{P} [(\lambda_p D_p x_{pc})_{mf}^{n+1} (\Phi_{pm} - \Phi_{pf})^{n+1}] - \sum_{p=1}^{P} (D_p x_{pc} q_{p,fm})^{n} \tag{5.2}$$

5.2 Determination of the Recovery Factor Increment

The general procedure to apply RCs to numerical models, as described by Heinemann (2004) and Mittermeir (2015), starts with obtaining RCs from SMB models, considering a single displacing phase (either water or gas) in the fracture. (The situation when using and changing these curves is equivalent to the assumption that the recovery factor resulting from both the water and gas drive curves remains valid independently from the recovery history.)

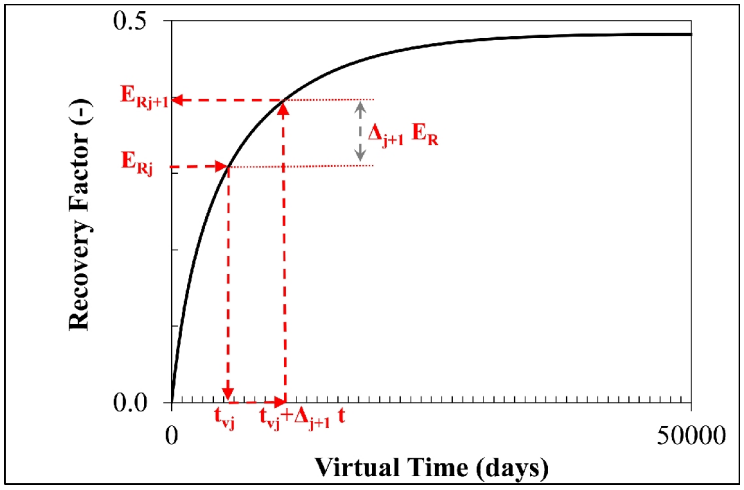

Figure 5.1: Schematic of a RC. Determination of recovery increment based on virtual time.

As Heinemann and Mittermeir (2014) described, Figure 5.1 "shows a schematic of a RC which will be given for water and gas drives and oil resaturation after water and gas displacement. Let E_R be the cell recovery factor at time t_j after any possible displacement history. The recovery factor values of E_R^w and E_R^g correspond to the virtual times t_v^w and t_v^g on the water and gas RCs respectively. Adding now an arbitrary time step $\Delta_{j+1}t$ and reading the normalized recovery factors at the new virtual time on the RCs

$$t_{vj+1}^w = t_{vj}^w + \Delta_{j+1}t; \tag{5.3}$$

$$t_{vj+1}^g = t_{vj}^g + \Delta_{j+1}t \tag{5.4}$$

results in the recovery factor increments for grid cell *k*:

$$\Delta_{j+1}E_{Rk}^w = (E_{Rk}^w(t_{vj+1}^w) - E_{Rk}^w(t_{vj}^w)); \tag{5.5}$$

$$\Delta_{j+1}E_{Rk}^g = (E_{Rk}^g(t_{vj+1}^g) - E_{Rk}^g(t_{vj}^g)). \tag{5.6}$$

This recovery factor increment is then used for determining the phase rates after it has been scaled in both the time (increment) and RF (ultimate recovery) axis".

5.2.1 Manual Scaling of the Recovery Curve

It is possible to manually scale RCs. This type of scaling was already introduced for the dual porosity material balance by Mittermeir (2015). These factors are used for matching the phase contact history of the reservoir.

The two factors are the RC scaling factor α and the time-scaling factor β. α is used for scaling the RC on the vertical axis, β stretches or compresses the time-axis.

The virtual time t_v^w is determined on the RC, which is scaled with α. Let E_{Rk} be the RF of cell k, then the virtual time is read for a scaled RF of E_{Rk}/α. The time step $\Delta_{j+1}t$ is then multiplied with the time scaling factor β:

$$t_{vj+1}^w = t_{vj}^w + \beta^w \Delta_{j+1} t; \tag{5.7}$$

$$t_{vj+1}^g = t_{vj}^g + \beta^g \Delta_{j+1} t. \tag{5.8}$$

The recovery factor is then determined for t_{vj+1}^w and multiplied with the scaling factor α:

$$\Delta_{j+1} E_{Rk}^w = (E_{Rk}^w(t_{vj+1}^w) - E_{Rk}^w(t_{vj}^w)) \cdot \alpha^w \tag{5.9}$$

$$\Delta_{j+1} E_{Rk}^g = (E_{Rk}^g(t_{vj+1}^g) - E_{Rk}^g(t_{vj}^g)) \cdot \alpha^g . \tag{5.10}$$

Figure 5.2 shows the schematic when the factors α and β are used. Firstly, the virtual time for the scaled recovery factor E_R/α is determined. The time increment is then multiplied with the timescale factor β and the new value of E_R/α is determined. The increase in E_R/α of the input RC is determined and then multiplied with α to obtain the actual applied increase in E_R.

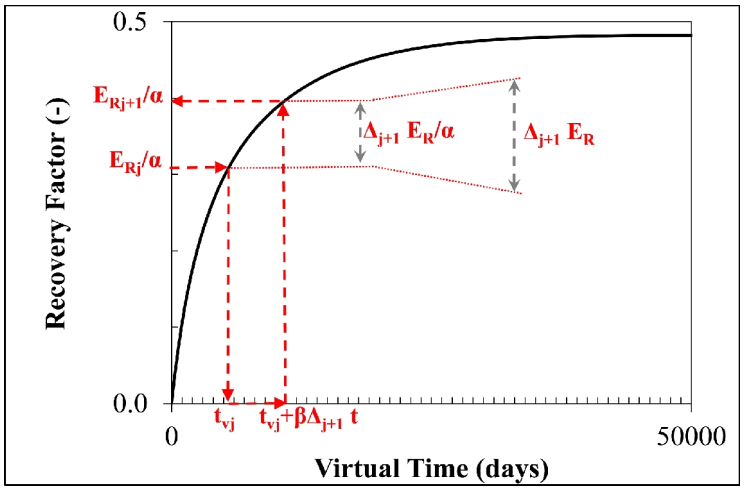

Figure 5.2: Schematic of a RC and determination of the increment when recovery curve- and timescale factors are used.

5.3 Determination of the Oil, Gas and Water Rates for the Constant Pressure Case

The fracture-to-matrix flux depends on the boundary condition for the cell provided by the fracture. The matrix-to-fracture mass transfer can comprise all mobile phases within the matrix block. At all times for a single cell at constant pressure conditions the in- and outflowing phase volume rates q_p are equal:

$$\sum_{p\,=\,o,\,g,\,w} q_{p,\,fm} \;=\; \sum_{p\,=\,o,\,g,\,w} q_{p,\,mf}. \tag{5.11}$$

Note, that the index *fm* and *mf* indicate the flow direction. Index "*mf*" indicates matrix-to-fracture, "*fm*" fracture to matrix flow. Based on this volumetric balance the matrix-fracture and fracture-matrix transfer rates resulting from the RC increment can be determined for waterdrive, gasdrive and also for non uniform fracture saturations.

5.3.1 Waterdrive and Gasdrive

When the drive mechanism is waterdrive or gasdrive, the matrix and fracture cells are filled with oil or gas, as shown in Figure 5.3 and Figure 5.4.

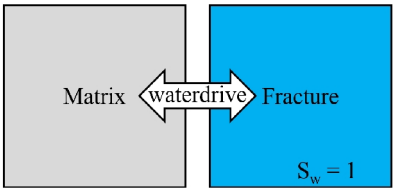

Figure 5.3: Fully water-filled fracture: waterdrive

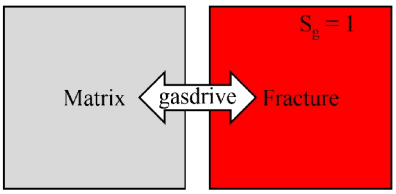

Figure 5.4: Full gas-filled fracture: gasdrive

From the RC the net flux of the oil phase

$$q_o \;=\; q_{o,\,mf} - q_{o,\,fm} \tag{5.12}$$

can be determined. In case of waterdrive or gasdrive $q_{o,fm}$ is zero and therefore the matrix-to-fracture oil phase rate $q_{o,mf}$ can be determined directly from the RC for the displacing

phases p, which is water (w) or gas (g). Let $\Delta_{j+1}E_R^p$ be the oil recovery increment from water or gas drive for the time step interval $\Delta_{j+1}t = t_{j+1}$-t_j then the volumetric oil matrix-to-fracture rate is:

$$q_{o,\,mf}^{p} = \frac{OOIP}{(1-x_{og})D_o} \cdot \frac{\Delta_{j+1}E_R^p}{\Delta_{j+1}t}, \text{ with } p = w,g \tag{5.13}$$

where $OOIP$ is the original molar oil in place, x_{og} is the mole fraction of the gas component in the oil phase and D_o is the specific molar density of the oil phase. The injecting phase must replace all volumes leaving the matrix. When the RCM is applied the phase potentials in Equation 5.1 only consider the pressure difference, since the capillary pressures and gravitational forces are already incorporated into the RC. Therefore, the differences of the potential (Φ) between matrix and fracture for all phases are identical:

$$\Phi_{om} - \Phi_{of} = \Phi_{gm} - \Phi_{gf} = \Phi_{gm} - \Phi_{gf} = p_m - p_f \tag{5.14}$$

For expansion the phase matrix-to-fracture transfer can be expressed as a linear relationship of the fracture-matrix potential difference (as in conventional transfer equations), as shown in Steiner and Mittermeir (2017). Therefore, using the mobility (λ) of the oil phase and the transmissibility τ:

$$q_{o,\,mf} = \tau_{mf}\lambda_o(p_m - p_f) \tag{5.15}$$

Separating the variables into phase dependent variables to the left side and phase independent variables to the right side:

$$\frac{q_{o,\,mf}}{\lambda_o} = \tau_{mf}(p_m - p_f) \tag{5.16}$$

Using Equation 5.16 Equation 5.11 can be rewritten, where the unkowns $q_{w,mf}$ and $q_{g,mf}$ are eliminated:

$$\sum_{p\,=\,g,\,w} q_{p,\,fm} = \sum_{p\,=\,o,\,g,\,w} \frac{\lambda_p}{\lambda_o} \cdot q_{o,\,mf} \tag{5.17}$$

For a water filled fracture and gas filled fracture the injection rates are:

$$q_{w,\,fm} = \sum_{p\,=\,o,\,g,\,w} \frac{\lambda_p}{\lambda_o} \cdot q_{o,\,mf}^{w}, \tag{5.18}$$

$$q_{g,\,fm} = \sum_{p\,=\,o,\,g,\,w} \frac{\lambda_p}{\lambda_o} \cdot q_{o,\,mf}^{g}, \tag{5.19}$$

where the superscript g (gasdrive) and w (waterdrive) denote the RC that is used for determining the oil matrix-to-fracture rate.

5.3.2 Oil Resaturation

From the RC (or resaturation curve) the net volumetric flux of the oil phase

$$q_o = q_{o,fm} - q_{o,mf} \tag{5.20}$$

can be determined. In case of oil resaturation $q_{o,fm}$ is not zero. Therefore, from the RC net oil flux q_o and not only the matrix-to-fracture oil flux is determined:

$$q_o = \frac{OOIP}{(1-x_{og})D_o} \cdot \frac{\Delta_{j+1}E_R^o}{\Delta_{j+1}t}. \tag{5.21}$$

The volumetric rate balance can then be written as

$$q_o = q_{o,fm} - q_{o,mf} = q_{w,mf} + q_{g,mf}. \tag{5.22}$$

The net oil flux is always positive for oil resaturation as the amount of oil in the matrix increases during this process. When the oil is injected into the matrix and the pressure must be constant, the volume that is injected as oil phase must come out of the matrix as water and gas phase. Outflowing oil must not be considered since it is already included in the net oil flux. Therefore, the water rate can determined with the matrix phase mobilities:

$$q_{w,mf} = \frac{\lambda_w}{\lambda_w + \lambda_g} \cdot q_o \tag{5.23}$$

and the gas rate with:

$$q_{g,mf} = \frac{\lambda_g}{\lambda_w + \lambda_g} \cdot q_o. \tag{5.24}$$

In Equation 5.23 and Equation 5.24 the denominator does not include the oil mobility, since the calculated rate can only be replaced by water or gas. Therefore, the term "total mobility" is omitted in this instance.

5.3.3 Non-Uniform Fracture Saturation

Both sides of Equation 5.17 are dependent on the fracture boundary condition. The left side directly, and for the right side $q_{o,mf}$ is different for different drive mechanisms, since the RCs for waterdrive and gasdrive are generally not identical. Theoretically possible boundary conditions comprise one, two or even three mobile phases in the fracture cell. When complete phase segregation is assumed in the fracture cell, the matrix-fracture pair can be imagined as shown in Figure 5.5 to Figure 5.8. It should be noted that in reality cases where all three mobile phases exist around the same matrix block in significant amounts would only occur if OWC and OGC would be approaching each other very closely.

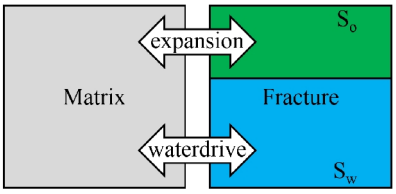

Figure 5.5: Fracture partially filled by oil and water

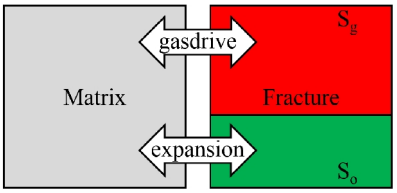

Figure 5.6: Fracture partially filled by oil and gas

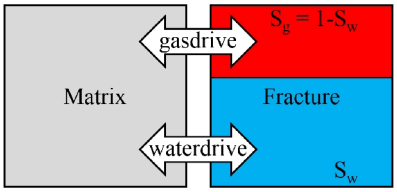

Figure 5.7: Fracture partially filled by gas and water

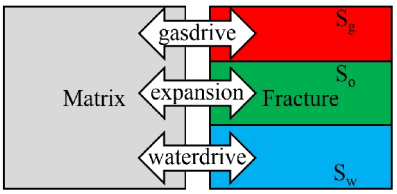

Figure 5.8: Fracture partially filled by oil, gas and water

Based on the boundary condition a weighting of the contribution of the recovery mechanisms with the fracture saturations can be done. This allows, when considering phase segregation within the fracture, to model different drive mechanisms within one grid cell that contains

multiple SMBs. When $q_{t,fm}$ represents the total fracture to matrix flow rate Equation 5.17 can be rewritten as:

$$q_{t,fm} = \sum_{p=o,g,w} \frac{\lambda_p}{\lambda_o} \cdot q_{o,mf} \quad . \tag{5.25}$$

The weighting of which type of recovery curve is used can be done by using the fracture saturations S_{pf}:

$$q_{o,mf} = S_{wf} \cdot q^{w}_{o,mf} + S_{gf} \cdot q^{g}_{o,mf}, \tag{5.26}$$

where the superscript w (waterdrive) and g (gasdrive) denotes the type of RC used for determining $q_{o,mf}$. Inserting Equation 5.26 into Equation 5.25:

$$q_{t,fm} = \sum_{p=o,g,w} \frac{\lambda_p}{\lambda_o} \cdot (S_{wf} \cdot q^{w}_{o,mf} + S_{gf} \cdot q^{g}_{o,mf}) \tag{5.27}$$

The water injection rate can then be expressed as:

$$q_{w,fm} = \sum_{p=o,g,w} \frac{\lambda_p}{\lambda_o} \cdot (S_{wf} \cdot q^{w}_{o,mf}) \tag{5.28}$$

and the gas injection rate:

$$q_{g,fm} = \sum_{p=o,g,w} \frac{\lambda_p}{\lambda_o} \cdot (S_{gf} \cdot q^{g}_{o,mf}) \,. \tag{5.29}$$

5.4 Scaling of the Recovery Curve

When an input RC, calculated for a matrix block at bubble point pressure in a two-phase condition, is used for matrix blocks at different conditions, scaling of the RC is necessary. Parameters like absolute permeability, matrix saturation or pressure influence the speed of recovery and the ultimate recovery factor. Similar to the introduced scaling factors α and β, also for an automatic scaling based on the matrix block condition, it can be distinguished between scaling of the increment (time-axis) and the ultimate recovery (vertical axis).

It should be noted, that this scaling of the RC is fundamentally different to the one implemented in the commercial reservoir simulator PumaFlow of Beicip-Franlab. In a letter received from Jean-Marc Gueri, the regional account manager of Beicip-Franlab from 2014, the correction is described:

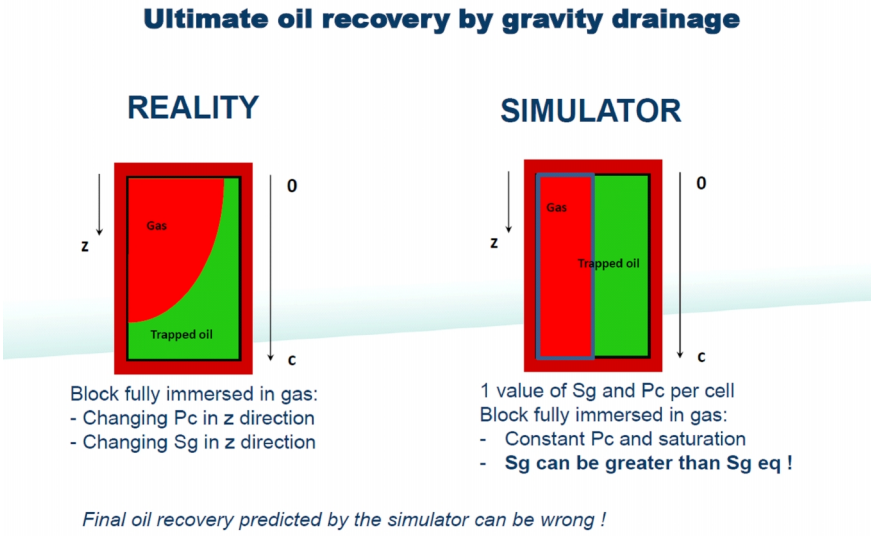

Figure 5.9: Explanation of the PumaFlow $E_{R,max}$ correction (Beicip-Franlab 2014)

"Rf [recovery factor] is computed internally by the software in each cell based on the capillary pressure curve, block height c and fluid densities. To do this, we can analytically express equilibrium saturation as a function of the depth z within one block (Pc(z) + gravity(z) = 0). As a result the average saturation in the block is the integral of saturation*dz with z between 0 and c, divided by c. We can do a change of variable in the expression to switch from dz to dPc and since we know the capillary pressure curve we can finish the computation. Then, during the simulation, the software will not accept values of gas or water saturation greater than this theoretical maximum value. (...) As a result, PumaFlow is “less wrong” than other simulators that will sometimes overestimate final recovery by allowing gas or water saturation to go above this theoretical maximum. In fact, we have made tests to compare with Eclipse and VIP (CMG was not tried). (...) The reference solution is obtained by very finally [sic] meshing a matrix block initially filled with oil and putting it in contact with fracture cells constantly filled with gas or water (...)".

Schlumberger's ECLIPSE 100 offers a similar correction, called "integrated capillary pressure option". Also in this case the capillary pressure function is manipulated to account for the non-uniform saturation distribution within the single matrix blocks and the resulting incorrect final recovery value.

This correction in PumaFlow for $E_{R,max}$ is not necessary for the RCM, since the input RC already accounts for the situation that the saturation has a vertical variation within the SMB, since it is derived by fine grid SMB calculation.

5.4.1 Correction of the Increment

A factor, scaling the speed of recovery similarly to the manually input time-scale factor β, can be determined based on the condition of the matrix block. The input RC is determined at a specific condition, at bubble point pressure, at a defined absolute permeability. Since the pressure and saturation condition changes in time and the absolute permeability from grid cell to grid cell, a scaling of the input RC is required.

5.4.1.1 Absolute Permeability

The absolute permeability changes the speed of the recovery process in, as can be clearly seen in e.g. the multiphase Darcy equation. Therefore, it is possible to scale the RC calculated at a effective permeability k_b to any other value of effective permeability k_k for grid cell k by stretching or compressing the time-axis of the RC. Generally, the effective permeability k_{eff} takes into account lateral and vertical permeability:

$$k_{eff} = \sqrt[3]{k_x k_y k_z}. \tag{5.30}$$

The values on the virtual time axis of the RC calculated at reference conditions, t_{vb}, is then scaled to the scaled virtual time t_{vk} of the RC for grid cell k with:

$$t_{vk} = t_{vb} \cdot \frac{k_b}{k_k}. \tag{5.31}$$

This mean, when the permeability is higher, the scaled virtual time is lower.

Because it is desired to use one RC and apply it to many different permeability values, it more convenient to scale only the timestep and not the entire virtual time. To scale the timestep $\Delta_{j+1}t$, it has to be considered that the timestep is applied to the reference virtual time of the input curve:

$$\Delta_{j+1} t_{vk} = \Delta_{j+1} t_{vb} \cdot \beta_k \tag{5.32}$$

where the time-scaling factor β_k is:

$$\beta_k = \frac{k_k}{k_b}. \tag{5.33}$$

It should be noted that in this case k_k is in the numerator and k_b in the denominator because the scaling of the timestep is applied to the input RC. This means that when k_k is higher than k_b, the timestep on the virtual time axis for cell k $\Delta_{j+1}t_k$ will be increased.

Figure 5.10 illustrates the simple stretching and compressing of the time-axis. A SMB model, where only the uniform and isotropic permeability was changed was calculated. The time to reach a RF of 0.4 is also indicated for each RC. When the case with 1.0 md is considered as the reference case, it must be possible to determine the times required to reach a RF of 0.4 also for the other permeability values with the scaling factor β_k. Let t_1 = 5630 days be the time required to reach a RF of 0.4 for the case of 1 mD. For 2 mD β_k = 2, therefore the actual virtual time is t_1/β_k = 2815 days, for 0.5 mD β_k = 0.5 and t_1/β_k = 11260 days and for 0.2 mD β_k = 5 and t_1/β_k = 28150 days. This is within numerical errors of the calculated days as shown in Figure 5.10.

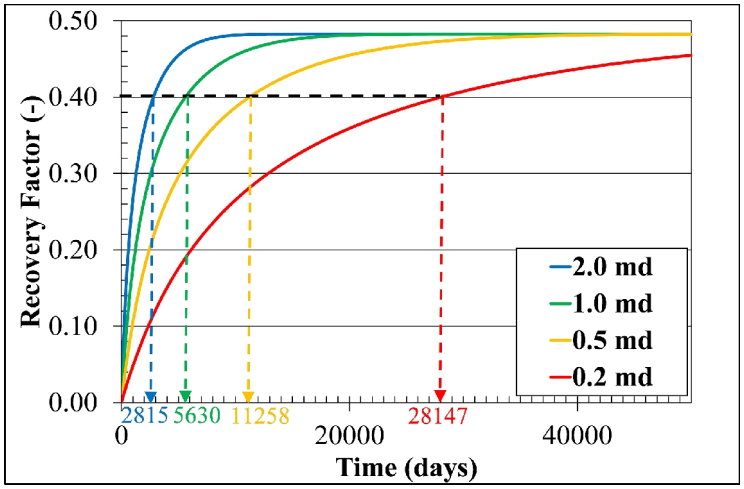

Figure 5.10: Recovery curves and time to reach RF = 0.4 for four permeabilities.

5.4.1.2 Pressure and Saturation Dependent Variables

Gharsalla (2015), Mittermeir (2015) and Heinemann and Mittermeir (2016) showed that it is possible to scale the RC increment during timestep $\Delta_{j+1}t$ with regard to the pressure and saturation dependent variables for the displacing phase p:

$$\frac{\Delta_{j+1}E_R^p(p)}{\Delta_{j+1}t} = \left(\left(\frac{k_{ro}(S_o)}{\mu_o(p)B_o(p)}\right)\Big/\left(\frac{k_{ro}(S_{ob})}{\mu_{ob}B_{ob}}\right)\right)\frac{\Delta_{j+1}E_R^p(p_b)}{\Delta_{j+1}t} \tag{5.34}$$

where the index b denotes the reference pressure of the RC, k_{ro} is the relative permeability of

oil, μ_o is the oil viscosity, S_o is the oil saturation and p is the average matrix block pressure.

5.4.2 Correction of the Endpoint

A factor can be determined or defined, which scales the value of ultimate recovery. This is similar to the RC scaling factor α, but not purely based on manual input but automatically changing to the condition present in the grid cell.

5.4.2.1 Changing Gravitational Driving Force

In a constant pressure scenario, the ultimate recovery of a matrix block is determined either by the point at which these two driving forces are in equilibrium or by the minimum mobile oil saturation. In a two-phase system the minimum mobile oil saturation as well as the capillary pressures are pressure independent, as long as it is constant. Although mostly a function of the saturation in the fracture, the gravitational force is also a function of pressure. The pressure dependence comes from the different phase compressibilities and the changing oil composition and is especially expressed when the fracture is gas filled. This can shift the equilibrium point and alter the ultimate recovery. Therefore, this correction is only necessary when negative oil-water capillary pressures are defined or when a gas-fluid capillary pressure is applied.

Gas Filled Fracture

To show this effect for gas filled fractures, four numerical SMB experiments are created. PVT data set no.1 and the rock data set no. 1 from Section 4.1 is used. The matrix has an isotropic permeability of 2 mD, a dimension of 10x10x10 m and fractures on all sides. Setup 1 is operated at bubble point pressure and setup 2 at 200 bar, setup 3 at 150 bar and setup 4 at 100 bar. Table 5.1 shows the oil and gas densities as well as the resulting ultimate recovery and average residual oil saturation in the matrix for all setups. The water saturation is constant at $S_{wi} = 0.18$ for all cases.

Table 5.1: SMB Setups for gas drive

#	$P_{fracture}$ [bar]	ρ_o [kg/m^3]	ρ_g [kg/m^3]	$\rho_o - \rho_g$ [kg/m^3]	μ_o	B_o	$E_{r,max}$	S_{or}
1	276.8	593.8	225.1	368.7	0.510	1.695	0.428	0.470
2	200.0	608.1	162.7	445.4	0.611	1.543	0.473	0.432
3	150.0	620.6	122.1	498.5	0.678	1.455	0.489	0.419
4	100.0	641.7	81.50	560.2	0.770	1.357	0.509	0.402

The resulting RCs for the setups can be seen in Figure 5.11. It can be seen that for using the constant pressure RCs calculated at P_b at another pressure, the curve has to be scaled, not only increment but also the endpoint.

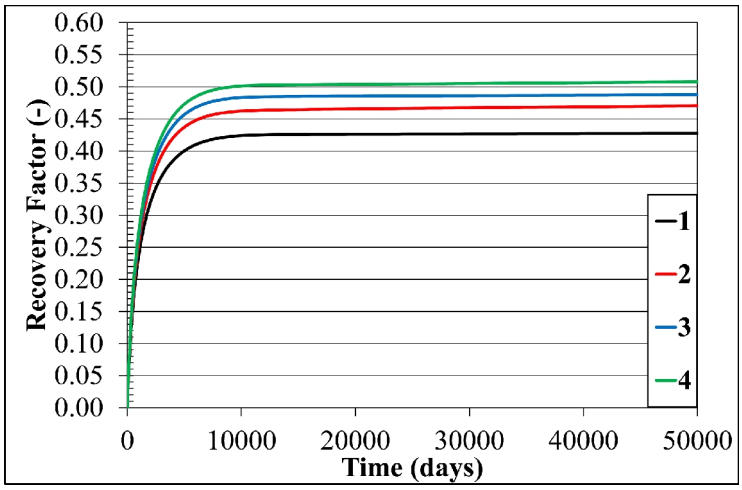

Figure 5.11: Recovery curves for setups 1 - 4.

It is possible to find a factor for scaling the RC endpoint. Using the ratio between the endpoints of two curves ($E_{R1,max}$ and $E_{R2,max}$) the values for the recovery factor of curve 1 can be adjusted (*adj*) to ensure a fit of the endpoints:

$$E_{R,\,adj}(t) = \frac{E_{R2,\,max}}{E_{R1,\,max}} \cdot E_{R1}(t). \tag{5.35}$$

With Equation 5.34 also the speed of recovery can be adjusted for the different viscosity μ_o and B_o. The value of k_{ro} does not need to be considered for this example since it will be the same for both curves, as the pressure does not change and therefore a constant relationship between S_o and E_R exists. From Equation 5.34 follows that the speed of recovery in curve 1 can be adjusted for by defining a adjusted time $t_{adf}(t)$ with:

$$t_{adj}(t) = t \cdot \frac{B_{o1}\mu_{o1}}{B_{o2}\mu_{o2}}, \tag{5.36}$$

resulting in:

$$E_{R,\,adj}(t_{adf}(t)) = \frac{E_{R2,\,max}}{E_{R1,\,max}} \cdot E_{R1}(t_{adf}(t)). \tag{5.37}$$

The using Equation 5.37 adjusted RCs of setup 2-3 can be seen in Figure 5.12, exhibiting a good match with the RC calculated at bubble point pressure. It can be seen that it is possible to find a factor for scaling the RC and account for the changes in the gravitational driving force.

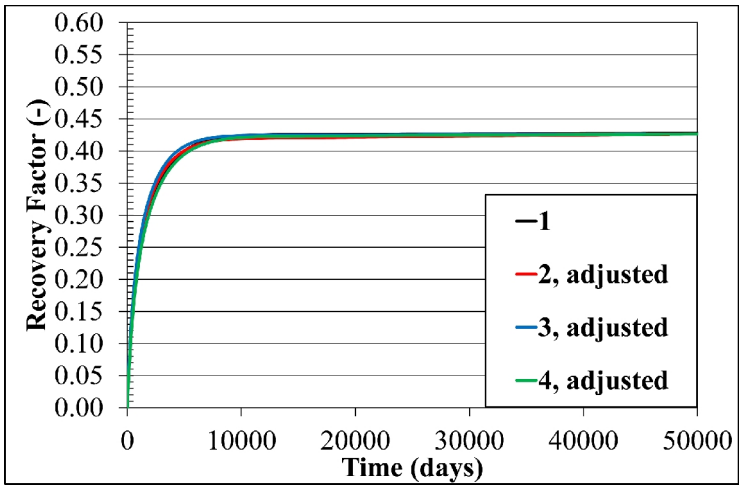

Figure 5.12: Recovery curves for of setups 2-4 adjusted to setup 1.

If the at bubble point pressure calculated RC is to be used for a DCM, the ultimate recovery is now known for all possible pressure scenarios and Equation 5.37 cannot be used for such cases. It is suggested to find this factor for a certain pressure using numerical SMB calculation. With a linear relationship between this factor and pressure the endpoints can then be adjusted for any pressure with good accuracy.

As an example, setup 3, calculated at 150 bar, can be used to estimate the ultimate recovery for setup 2 and 4. This is done with a linear equation used for interpolation and extrapolation between and beyond the data points:

$$E_{R,\,max}(p) \;=\; 1 + \left(\frac{E_{R3,\,max}}{E_{R1,\,max}} - 1 \right) \cdot \frac{p - p_1}{p_3 - p_1} \,. \tag{5.38}$$

This leads to estimated endpoints of $E_{R2,max} = 0.465$ and $E_{R4,max} = 0.513$. For setup 2 this is an overestimation of the ultimate recovery of 0.81% and for setup 4 an underestimation of 0.41%, when compared to the correct values from the SMB calculation. Figure 5.13 shows the RCs for setups 2 and 4 using the estimates for $E_{R,max}$ from Equation 5.38 and the scaling by Equation 5.37. If the scaling is correct, then the curves should match.

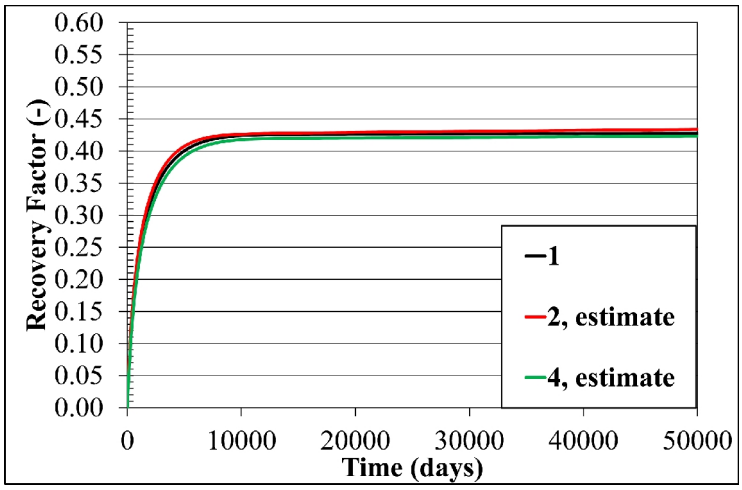

Figure 5.13: Recovery curves for setup 1 and the adjusted curves for setups 2 and 4 with estimated ultimate recovery.

Water Filled Fracture

To show the effect for water filled fractures, 6 SMB setups have been created, which are listed in Table 5.2. The matrix blocks have a dimension of 10x10x10 m, an isotropic permeability of 1 mD and fractures on all sides. PVT data set no.2 and the rock data set no. 1 from Section 4.1 is used. Naturally, the density difference between water and oil maximal at bubble point pressure.

Table 5.2: SMB setups for water drive

#	$P_{fracture}$ [bar]	ρ_o [kg/m^3]	ρ_g [kg/m^3]	$\rho_o - \rho_g$ [kg/m^3]	μ_o	B_o	$E_{r,max}$	S_{or}
1	155.1	700.0	1084.0	-384.0	0.482	1.259	0.150	0.697
2	200.0	735.4	1084.1	-348.7	0.548	1.199	0.130	0.714
3	250.0	776.7	1084.2	-307.5	0.632	1.135	0.113	0.728
4	280.0	802.6	1084.3	-281.7	0.688	1.099	0.104	0.735
5	120.0	717.1	1083.8	-366.8	0.554	1.198	0.139	0.706
6	80.0	738.8	1083.8	-345.0	0.660	1.129	0.128	0.715

Figure 5.14 shows the calculated RCs for the 6 setups. It can be seen that the highest recovery is reached when the calculation takes place at bubble point, where also the gravitational driving force is the highest.

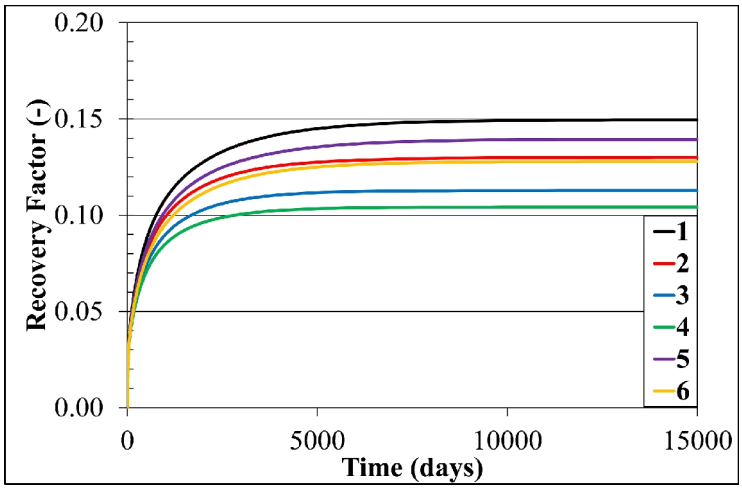

Figure 5.14: Recovery curves for setups 1-6

The RCs can be adjusted using Equation 5.37, using the determined endpoints from the SMB calculation. The results show that also for waterdrive it is possible do determine a factor to correct the RC, as can be seen in Figure 5.15.

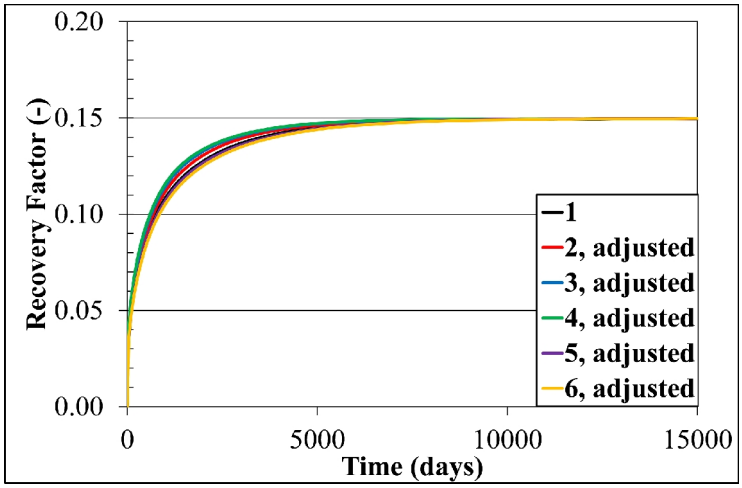

Figure 5.15: Recovery curves for setups 2-6 adjusted to setup 1.

For the estimation of the ultimate recovery in case of waterdrive, two linear equations are needed. One is needed for when the oil is undersaturated, where the gravitational driving force increases with decreasing pressure. The second for when the oil is below bubble point pressure and the gravitational driving force decreases with decreasing pressure. This can be explained by the relatively constant water density and shape of the function $B_o(p)$ (see Figure 4.1 right).

Setup 3, calculated at 250 bar, is selected for the function above bubble point and setup 5 (120 bar) for the one below bubble point. Using Equation 5.38 the estimated endpoints are $E_{R2,max}$ = 0.132, $E_{R4,max}$ = 0.101 and $E_{R6,max}$ = 0.128. For setup 2 this is an overestimation of the ultimate recovery factor of 0.22%, for setup 4 an underestimation of 0.29% and for setup 6 an underestimation of 0.04%. The difference for setup 4 is the highest, which results in a not

perfectly matched RC when adjusted using this ultimate recovery factor (Figure 5.16).

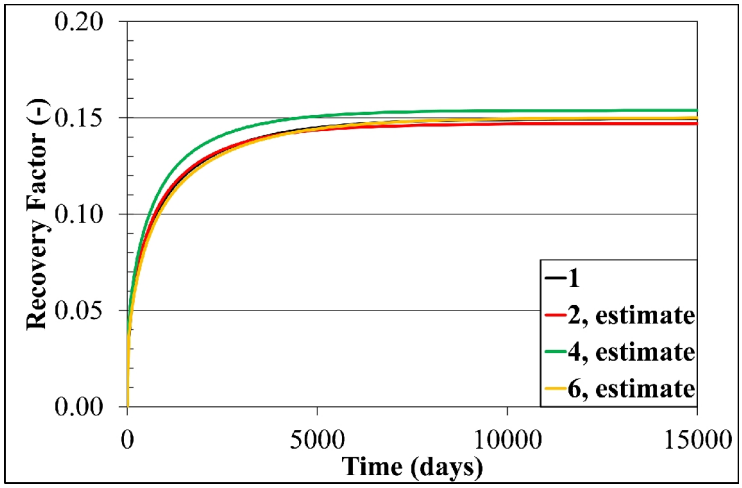

Figure 5.16: Recovery curves for setups 2,4 and 6 adjusted to setup 1 with estimated ultimate recovery.

Suggestion

This correction is only necessary when a negative oil-water capillary pressure exists or when a gas-fluid capillary pressure curve is used. Otherwise the saturation endpoints are strictly determined by the used relative permeability curves and the endpoint scaling with regard to the gravity drainage force is not necessary.

For gas drive one correction factor should be determined at the expected minimum pressure at which the RC will be applied. As this factor is a function of pressure, linear interpolation between the determined value and a value of 1 at bubble point gives the required correction factor.

For water drive, two correction factors should be determined at the expected highest and lowest pressure at which the RC will be applied. One should be above bubble point and one below bubble point. If the system is never expected to go below bubble point, the second linear interpolation and extrapolation function is not required.

5.4.2.2 Changing Oil Formation Volume Factor

When the pressure during the recovery process changes, also the oil formation volume factor B_o will change. When both the actual oil saturation and B_o are defined as a function of time then the recovery factor E_R can be written as

$$E_R(t) = 1 - \frac{S_o(t)B_{oi}}{B_o(t)S_{oi}}. \tag{5.39}$$

When considering only one point in time, at which the ultimate recovery $E_{R,max}$ is reached, then S_o will be the residual oil saturation S_{or} and B_o is a function of pressure:

$$E_{R,\,max}(p) \;=\; 1 - \frac{S_{or} B_o(p_i)}{B_o(p) S_{oi}}, \tag{5.40}$$

where p_i is the initial pressure. The input RC calculated at reference condition b is calculated at constant pressure. Therefore Equation 5.40 can be rewritten as

$$E_{Rb,\,max} \;=\; 1 - \frac{S_{or}}{S_{oi}} \tag{5.41}$$

for the input curve, since $B_o(p)$ is always the same as B_{oi}. When the constant pressure RC is used the endpoint has to be scaled by building the ratio:

$$\frac{E_{R,\,max}(p)}{E_{Rb,\,max}} \;=\; \frac{1 - \dfrac{S_{or} B_o(p_i)}{B_o(p) S_{oi}}}{1 - \dfrac{S_{or}}{S_{oi}}} \tag{5.42}$$

an rearranging it to get Equation 5.43:

$$E_{R,\,max}(p) \;=\; E_{Rb,\,max}\left(\frac{1 - \dfrac{S_{or} B_o(p_i)}{B_o(p) S_{oi}}}{1 - \dfrac{S_{or}}{S_{oi}}} \right) \tag{5.43}$$

Using this equation the endpoint of the constant pressure RC can be scaled for cases when the pressure is changing. It should be noted that in Equation 5.43 all variables except for $B_o(p_i)$ and $B_o(p)$ are considered constant.

In case of water drive in a three-phase system the expected residual oil saturation is different than the one calculated for the input RC. The amount of water that displaces the oil in the matrix is determined by the balance of gravitational and capillary forces. How to account for changing gravitational forces has already been discussed in the previous section. The capillary forces between water and oil are a function of the water saturation and do not change with pressure or the presence of gas in the matrix. Therefore, after the mobile gas has left the matrix block, the residual oil saturation can be approximated by:

$$S_{orm} \;=\; S_{or} - S_{gc}, \tag{5.44}$$

where S_{gc} is the critical gas saturation. Inserting this in Equation 5.43 gives:

$$E_{R,\,max}(p) = E_{Rb,\,max}\left(\frac{1-\frac{S_{orm}B_o(p_i)}{B_o(p)S_{oi}}}{1-\frac{S_{or}}{S_{oi}}}\right). \tag{5.45}$$

5.4.3 Considering Permeability Anisotropy

After scaling of the input RC with regard to pressure dependent variables and absolute permeability, the handling of varying permeability anisotropies remains. Commonly, the ratio between vertical to horizontal permeability k_v/k_h is used for quantifying anisotropy.

In contrast to the scaling of the increment for different values of absolute permeabilities, the situation for strongly differing anisotropy ratios is more complex. To show the effect of anisotropy, six SMB calculations with an identical effective permeability of 2 mD but anisotropy ratios varying between 0.01 and 8.0 are performed. The calculation is done at bubble point pressure and the displacing phase is water. The results can be seen in Figure 5.17.

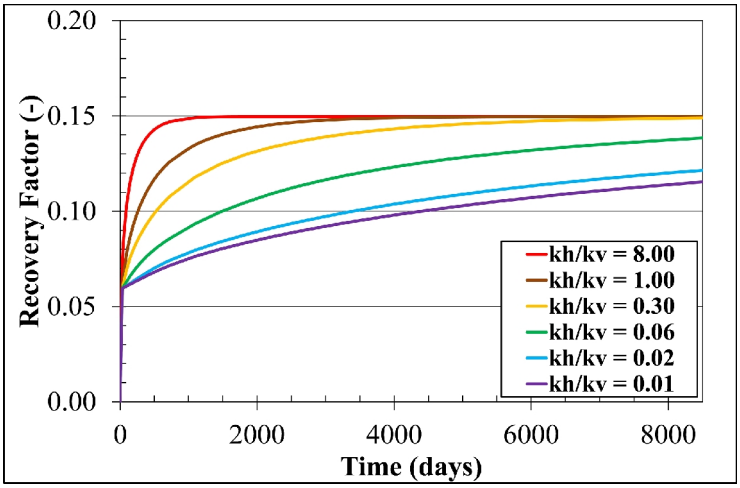

Figure 5.17: Influence of permeability anisotropy on the oil RC

All SMB setups are trending to the same asymptotic value. Up to a recovery factor of 0.06, the curves are nearly identical. This can be explained by spontaneous imbibition into matrix block surface near regions. After this immediate water imbibition, the RC speeds depend on the permeability anisotropy. This is not simply a linear relationship, because the varying anisotropy causes different a saturation distribution within the matrix block. This significantly influences the gravitational and capillary driving force. This results in a complex effect, which cannot be easily described as a function of the form $RF = f(\mathrm{k_h/k_v})$.

The solution is to provide input RCs for a given range of anisotropy ratios. For example, if the anisotropy ratio varies between 1.00 and 0.10, four input RCs representing successive ratio intervals of 0.25 could be created. For this the RC region concept can be applied, which was

already introduced by Amiry (2014). This assigns RCs on a gridblock basis. Therefore, no scaling for permeability anisotropy is applied, rather an adequate definition of RC regions is suggested.

Chapter 6

Verification of the Recovery Curve Method

In lack of experimental evidences, assessing the applicability of mass transfer methods between fracture and matrix can only be done by comparing the results of dual continuum and fine grid SMB calculations. A comprehensive evaluation can be accomplished with a dual porosity column model where the matrix is either represented by a single cell or finely gridded. If the results are similar the transfer model is applicable. In this chapter the RCM, as described in Chapter 5, is verified.

6.1 The Column Model

A homogenous column model with 12 layers serves as a basis for three numerical experiments. Every layer has a lateral dimension of 10x10 m and a height of 10 m. The top and the bottom layer are single porosity, where only the fracture domain exists. The other 10 layers in between consist of both matrix and fracture domain.

The matrix has a porosity of 20.0% and an isotropic permeability between 0.2 mD and 1.0 mD, depending on the setup. The fracture has a vertical permeability of 1000 mD and a porosity of 5%. The top and bottom cell have well perforations (Well 1 and Well 2), used for operating the column model. The matrix cells are numbered top-to-bottom from 1 to 10. PVT data, SCAL data, initial oil-water contact, oil production and water or gas injection rates vary with each setup.

The two utilized approaches for modeling the described column are the creation of a DCM and a single continuum (SCM) model using finely gridded SMBs. Figure 6.1 illustrates the conceptual model, but for practical reasons only 4 layers are shown. For the SCM at every time step the SMB is calculated on a quarter model with the boundary condition defined by the fracture cell of the column model.

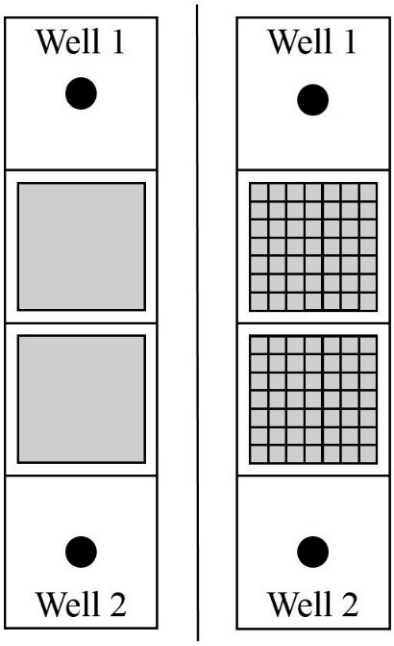

Figure 6.1: Conceptual column model in a dual continuum formulation (left) and with finely gridded matrix block (right)

6.2 PVT Data and Rock Functions

Two setups of PVT data and two sets of rock functions are used. All data sets are taken from real field cases but the owners of this propriety data do not permit the name of the reservoirs to be published. PVT no. 1 and ROCK data no. 2 are taken from the one reservoir and PVT no. 2 and ROCK data no. 1 are taken from another reservoir. Therefore, in the setups PVT no. 1 will used combined with ROCK no. 2 and PVT no. 2 with ROCK no.1. The two PVT data sets have already been used in Section 4.1 and are shown there.

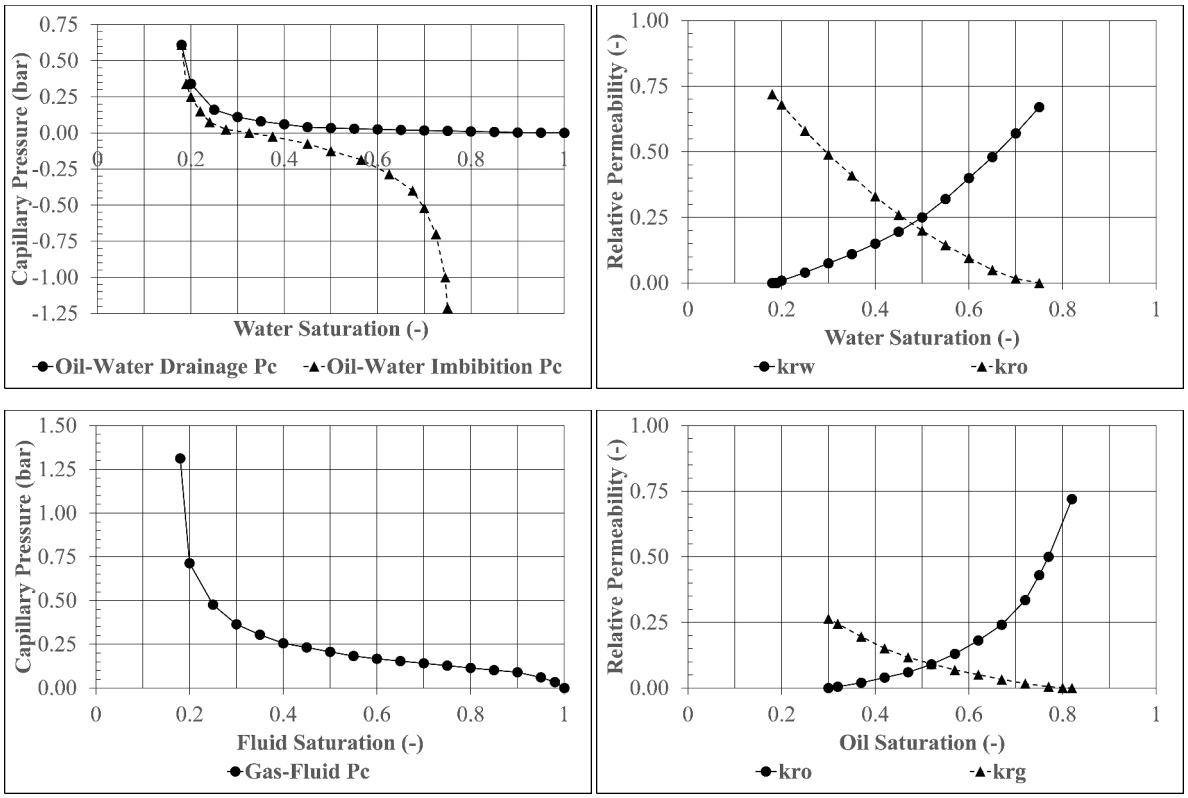

Figure 6.2: Capillary pressure and relative permeability functions of data set no.1

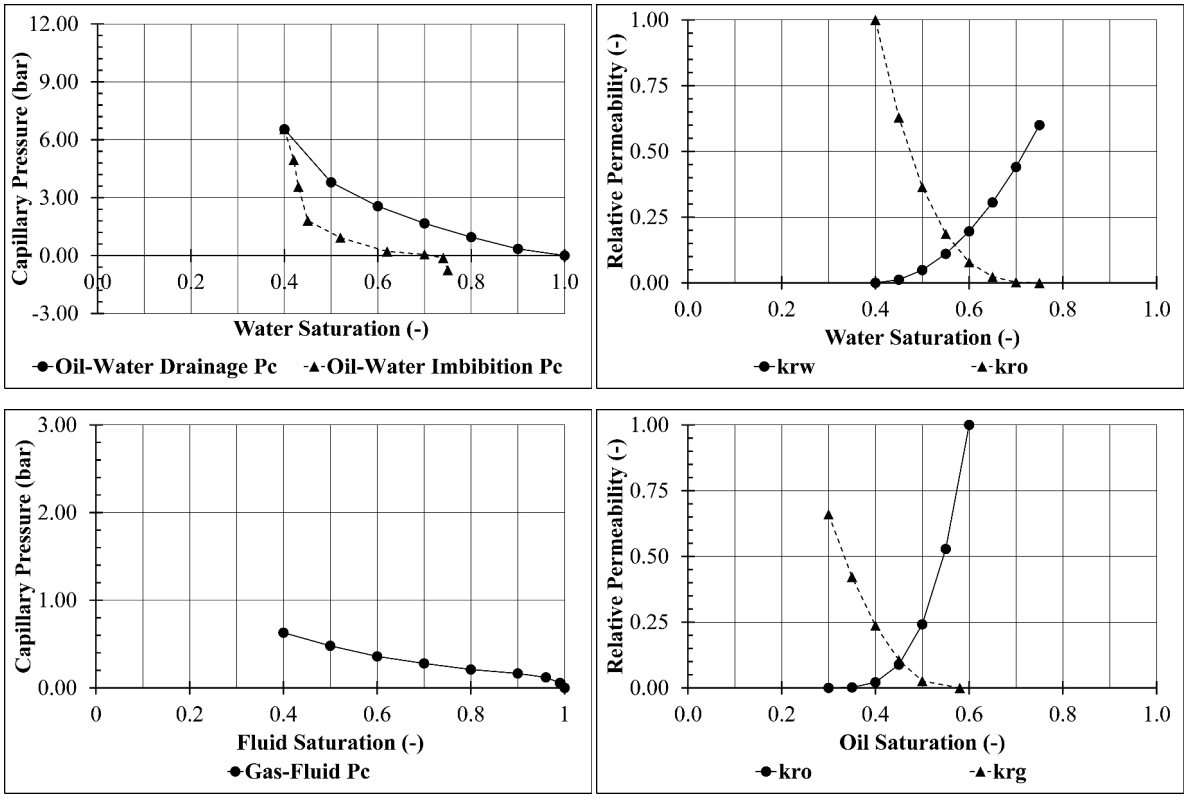

Figure 6.3: Capillary pressure and relative permeability functions of data set no.2

6.3 Experimental Setups

6.3.1 Summary

Six setups, listed in Table 6.1, are created. They vary in type of drive mechanism, PVT data, ROCK data, initial pressure, pressure drop during the calculation, days of calculation, matrix permeability and number of mobile phases.

Each setup is calculated using the SCM, the DCM with RCs and, for comparison, the Kazemi et al. (1976) transfer equation with the Gilman and Kazemi (1988) gravity drainage model. To show the effect of the increment and endpoint scaling factors, which are described in Section 5.4, all setups are calculated with

a.) $E_{R,max}$ and increment scaling
b.) only increment scaling and
c.) without and scaling of the RC.

Table 6.1: Column model setups

Setup	PVT sno.	ROCK sno.	P_{avr} init. [bara]	P_{avr} end [bara]	Drive Mechanism	Days of calculation	k [mD]	mobile phases
1	2	1	184	183	water	6574	1.0	2
2	2	1	140	123	gas	5113	0.2	2
3	2	1	160	142	water	6209	1.0	3
4	1	2	330	327	water	10957	0.5	2
5	1	2	200	166	gas	18262	1.0	2
6	1	2	283	248	water	6209	1.0	3

For the RC option the input curves are created with SMB calculations at bubble point pressure. The dimensions, permeability, PVT and ROCK data is the same as in the corresponding dual continuum matrix blocks. The RC were also calculated for pressures above and below bubble point, to correct the ultimate recovery for different pressures as described in Section 5.4.2.1. $E_{R,max}$ and the parameters required for scaling the input RC can be seen in Table 6.2. For all setups also the oil resaturation curves are created.

Table 6.2: Input RC parameters and correction factors

Setup	$E_{R,max}$ for $P = P_b$	$E_{R,max}$ for $P < P_b$	$E_{R,max}$ for $P > P_b$	μ_o [cP]	B_o [rm^3/sm^3]
1	0.1496	-	0.1341 @190bar	0.482	1.259
2	0.4792	0.4893 @115bar	-	0.482	1.259
3	0.1496	0.1440 @135bar	0.1451 @165bar	0.482	1.259
4	0.5316	-	0.5299 @340bar	0.510	1.695
5	0.2541	0.2769 @160bar	-	0.510	1.695
6	0.5471	0.5446 @240bar	0.5466 @290bar	0.510	1.695

The saturation initialization for setups with water injection (no. 1, 3, 4 and 6) is as shown in Figure 6.4.
The initial saturations are:

- Matrix: $S_w = S_{wi}$, $S_o = 1\text{-}S_{wi}$ and $S_g = 0$
- Fracture and cell containing Well 1: $S_w = S_g = 0$ and $S_o = 1$
- Cell containing Well 2: $S_w = 1$, $S_g = S_o = 0$

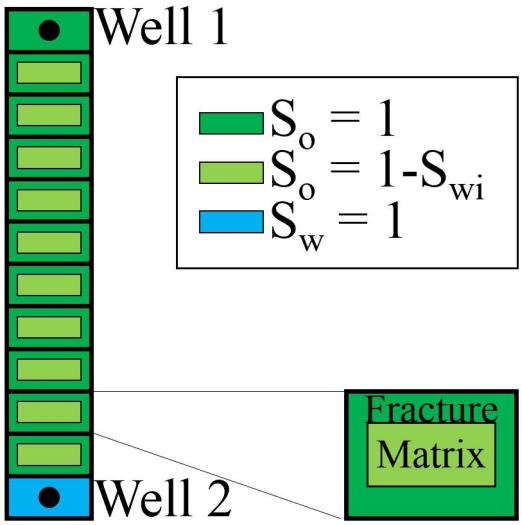

Figure 6.4: Initial saturations in the column for setups 1, 3, 4 and 6

The saturation initialization for setups with gas injection (no. 2 and 5) is as shown in Figure 6.5.
The initial saturations are:

- Matrix: $S_w = S_{wi}$, $S_o = 1\text{-}S_{wi}$ and $S_g = 0$
- Fracture and cells containing Well 1 & 2: $S_w = S_g = 0$ and $S_o = 1$

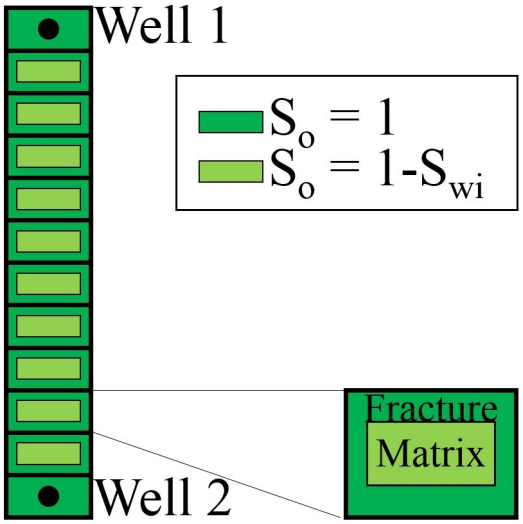

Figure 6.5: Initial saturations in the column for setups 2 and 5.

6.3.2 Setup 1

Setup 1 exhibits waterdrive at a nearly constant pressure of 184 bar. This is 29 bar above the bubble point pressure of the used PVT data set no. 2, therefore it is assured that the oil is undersaturated throughout the calculation and only 2 mobile phases exist. The matrix permeability is 1 mD and SCAL data set no. 1 is used.

Well 1 is an oil production well with a constant liquid production rate of 1.0 sm^3/day. It produces from the beginning until day 608 and is shut in afterwards. Well 2 is a water injection well operating at a constant bottom hole pressure of 188.8 bar, which is also shut in after 608 days. The overall duration of the calculation is 6574 days.

6.3.3 Setup 2

Setup 2 tests gasdrive in combination with expansion. PVT table 2 with a bubble point pressure of 155 bar and the oil-wet SCAL data set no.1 are used. Initially, the average pressure in the column model is to 140 bar and the fracture is filled with oil, as shown in Figure 6.5, and the oil is fully saturated. The matrix permeability is 0.2 mD.

Well 1 is a gas injection well, which starts injecting at day 32 with a constant injection rate of 190 sm^3/day. At the same time Well 2 starts producing oil at a rate of 1.0 sm^3/day. On day 455, shortly before gas breakthrough at Well 2, Well 1 is converted into a gas production well and is assigned a constant production rate of 10 sm^3/day. At the same time the oil production rate at Well 2 is reduced to 0.05 sm^3/day. On day 1247 both wells are then shut-in. The overall duration of the calculation is 5113 days.

6.3.4 Setup 3

In setup 3 waterdrive in combination with expansion is tested. PVT table 2 with a bubble point pressure of 155 bar and the oil-wet SCAL data set no.1 are used. During the calculation the pressure drops below the bubble point and three mobile phases will be present. Initially, the average pressure in the column model is 160 bar and every cell is above bubble point and undersaturated. The matrix permeability is, as in setup 1, 1 mD.

Well 1 is an oil producer, which starts producing immediately with a production rate of 0.8 sm^3/day. Well 2 is a water injection well and is controlled by a defined bottom hole pressure. At the beginning the injection pressure is 163.3 bar and is stepwise dropped by 0.2 bar each month. After 2372 both wells are shut-in. At this time the injection pressure dropped already to 147.9 bar. The overall duration of the calculation is 6209 days.

6.3.5 Setup 4

Setup 4 tests waterdrive at a nearly constant pressure of 330 bar, like setup 1. However, it uses different PVT and SCAL data and has a lower matrix permeability. The pressure is 53 bar above the bubble point pressure of the used PVT data set no. 1, therefore the oil is undersaturated throughout the calculation and only 2 mobile phases exist. The matrix permeability is 0.5 mD and SCAL data set no. 2 is used.

Well 1 is an oil production well with a constant liquid production rate of 1.0 sm^3/day. Well 2 is a water injector with a constant bottom hole pressure of 333.2 bar. Both wells are shut-in after 415 days. The overall duration of the calculation is 10957 days.

6.3.6 Setup 5

Setup 5 tests gasdrive in combination with expansion, like setup 2. However, it uses different PVT and SCAL data and has a higher matrix permeability. PVT table 1 with a bubble point pressure of 276.8 bar and the water-wet SCAL data set no.2 are used. Initially, the average pressure in the column model is to 200 bar and the fracture is filled with oil, as shown in Figure 6.5, and the oil is fully saturated. The matrix permeability is 1.0 mD.

Well 1 is a gas injection well, which starts injecting at day 32 with a constant injection rate of 215 sm^3/day. At the same time Well 2 starts producing oil at a rate of 1.0 sm^3/day. On day 334, shortly before gas breakthrough at Well 2, Well 1 is converted into a gas production well and is assigned a constant production rate of 10 sm^3/day. At the same time the oil production rate at Well 2 is reduced to 0.05 sm^3/day. On day 1247 both wells are then shut-in. The overall duration of the calculation is 18262 days.

6.3.7 Setup 6

Like setup 3, setup 6 tests waterdrive in combination with expansion. However, it uses different PVT and SCAL data. PVT table 1 with a bubble point pressure of 276.8 bar and the water-wet SCAL data set no. 2 are used. During the calculation the pressure drops below the bubble point and three mobile phases will be present. Initially, the average pressure in the column model is 283 bar and every cell is above bubble point and undersaturated. The matrix permeability is 1 mD.

Well 1 is an oil producer, which starts producing immediately with a production rate of 0.8 sm^3/day. Well 2 is a water injection well and is controlled by a defined bottom hole pressure. At the beginning the injection pressure is 286.3 bar and is stepwise dropped by 0.3 bar each month. After 3469 both wells are shut-in. At this time the injection pressure dropped already to 252.7 bar. The overall duration of the calculation is 6209 days.

6.4 Results

6.4.1 Summary

Setups 1 to 3 show that the RC is appropriate for modeling the matrix-fracture mass transfer. The TF overpredicts the speed of recovery as well as the ultimate recovery for these setups. For the waterdrive setups, which use the oil-wet rock data, only the scaling of $E_{R,max}$ is significant and for gasdrive only the scaling of the increment has an influence.

For setups 4 to 6, which use water-wet rock data, all transfer models show acceptable results for the maximum recovery factor. For gasdrive, the TF overpredicts the speed of recovery significantly, whereas all RC scaling options give accurate results. In case of waterdrive, all transfer models give acceptable results. Generally, the scaling options only have a minor influence, but the mixture of increment and $E_{R,max}$ scaling gives the most correct results.

In the following sections a detailed description and visualization of the results can be seen.

6.4.2 Setup 1

The cumulative oil and water production and the average pressure of the column model for the Single Continuum Model (SCM), the transfer function (TF) and the recovery curve method (RC) can be seen in Figure 6.6. Oil is produced from the top of the column and water is injected with constant pressure at the bottom of the column. The hydrocarbon-weighted average pressure decreases as the oil is displaced in the lower parts of the column, where the pressure is

higher. The constant liquid production rate results in a constant slope of the cumulative oil production curve, until water is produced. Water breakthrough at Well 1 happens later, when the TF is used. This can also be seen in Figure 6.7 to Figure 6.11, where a time lag of the start of waterdrive when using the TF compared to SCM/RC exists, which increases upwards in the column. This is because the estimated oil recovery is much faster when using the TF and more water enters the matrix.

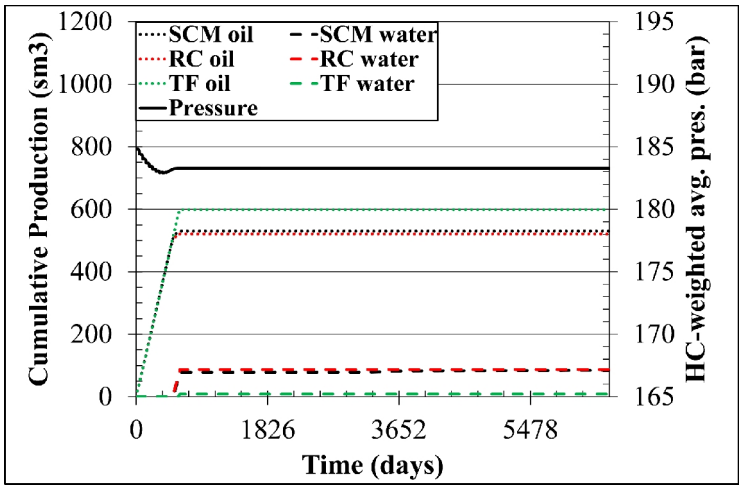

Figure 6.6: Setup 1: Average pressure and cumulative oil and water production when using the RCM, the TF and the SCM.

In the top matrix cell 1 (Figure 6.7, left) the time lag between the start of waterdrive when using the TF is most expressed. The start of waterdrive can be identified by the sudden change of slope, when the recovery mechanism changes. Additionally, oil resaturation occurs in cell 1 after the production is stopped but oil is still displaced from the matrix cells. As the mobile oil and water phase separate in the fracture, oil starts filling the fracture column again beginning from the top. After the oil saturation is high enough also in the fracture neighbor of matrix cell 1, oil will re-enter the matrix.

Generally, Figure 6.7 to Figure 6.11 show a very good agreement between the SCM and the RC results. The speed of recovery as well as the ultimate recovery at the end of the calculation is similar. The TF overpredicts both speed of recovery and the asymptote of the recovery factor. The reason for the difference will be discussed and explained in detail in Section 6.5.

The results show also a slight increase in $E_{R,max}$ from the bottom to the top, with the exception of cell 1, where oil resaturation occurs and the asymptote is not approached. This is also observable for the RC and the TF. This can be explained by the fact that the pressure is higher at the bottom of the column than at the top of the column, leading to a decreasing $E_{R,max}$ in the bottom cells, as shown in Section 5.4.2.1. The TF includes the changing densities at different pressures and the RC also corrects for this automatically with the defined $E_{R,max}$ for a higher pressure (see Table 6.2).

Table 6.3 shows the maximum recovery factors for all matrix cells and all calculation setups (SCM, RC (a) with $E_{R,max}$ and increment scaling, RC (b) with increment scaling, RC (c) without

scaling and TF). It is evident that the RC method is more accurate in predicting the ultimate recovery than the TF. It can also be seen that for the SCM, RC (a) and TF the recovery factor increases upwards, where the pressure is lower. For RC (b) and RC (c), although still more accurate than the TF, this is not the case, as the $E_{R,max}$ scaling is not applied.

Table 6.3: Maximum recovery factors for Setup 1

	Maximum Recovery Factor $E_{R,max}$ (-)				
Matrix Cell	**SCM**	**RC (a)**	**RC (b)**	**RC (c)**	**TF**
1	0.123	0.124	0.129	0.131	0.143
2	0.140	0.136	0.137	0.138	0.180
3	0.139	0.136	0.137	0.138	0.180
4	0.139	0.136	0.137	0.138	0.179
5	0.138	0.135	0.137	0.138	0.178
6	0.137	0.135	0.137	0.138	0.177
7	0.136	0.134	0.137	0.138	0.177
8	0.136	0.134	0.137	0.138	0.176
9	0.135	0.133	0.137	0.138	0.175
10	0.134	0.133	0.137	0.137	0.175

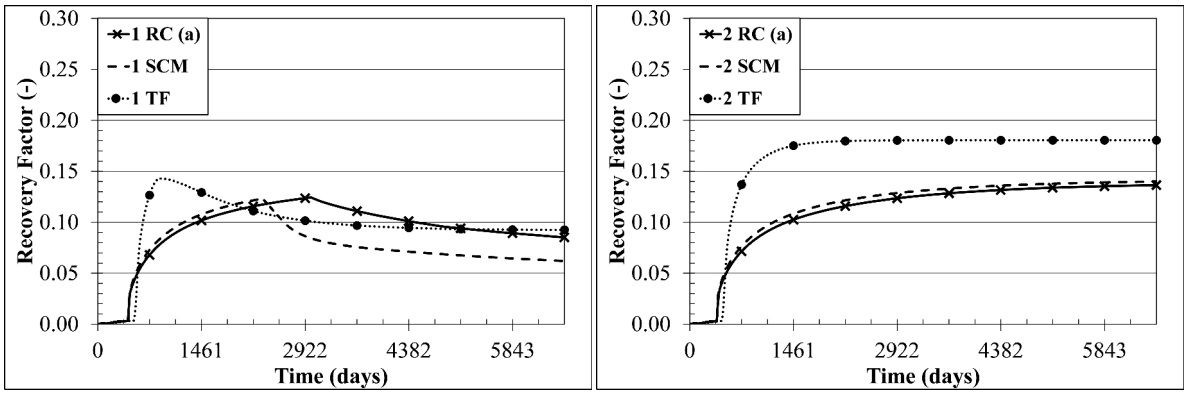

Figure 6.7: Recovery curves for matrix cells 1 and 2 when using the RC method with scaling (RC (a)), the SCM and the TF.

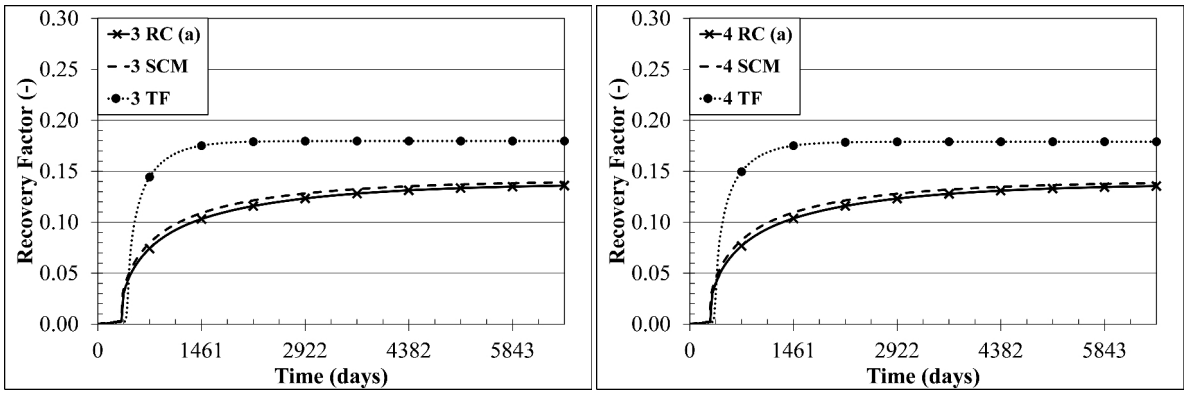

Figure 6.8: Recovery curves for matrix cells 3 and 4 when using the RC method with scaling (RC (a)), the SCM and the TF.

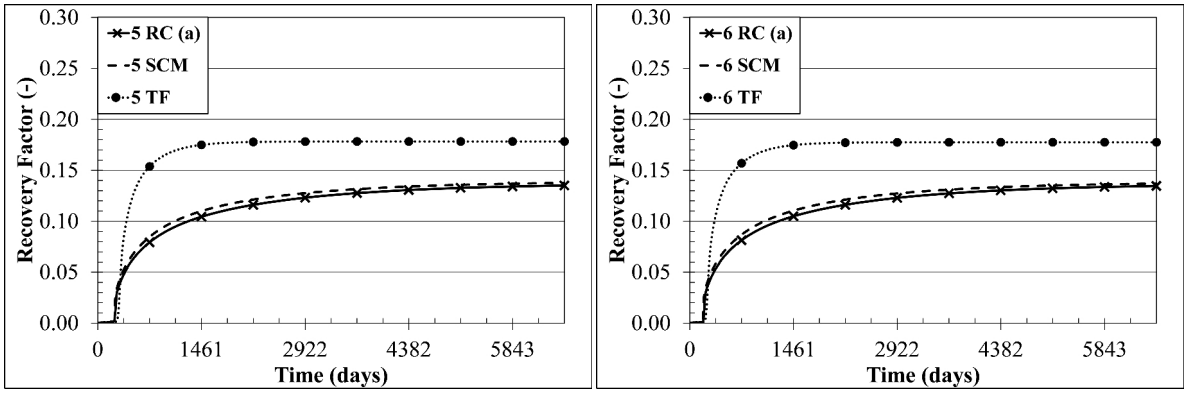

Figure 6.9: Recovery curves for matrix cells 5 and 6 when using the RC method with scaling (RC (a)), the SCM and the TF.

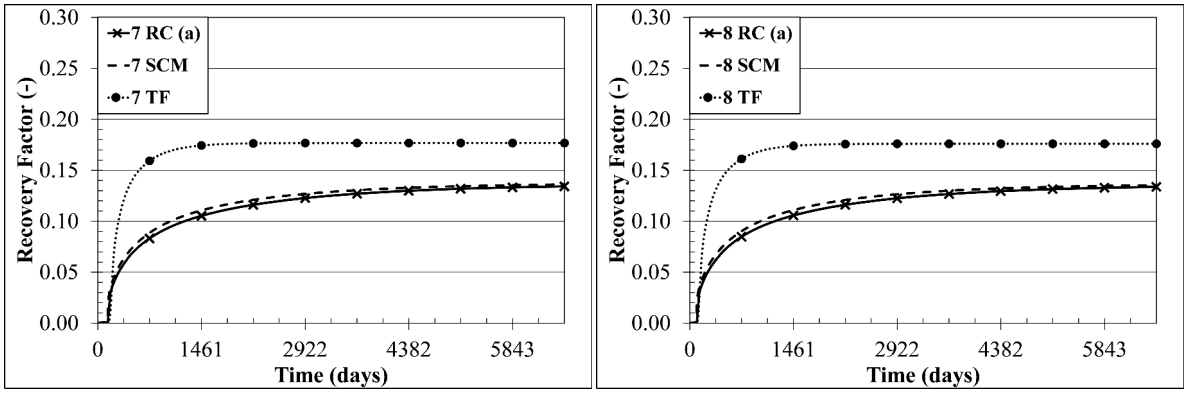

Figure 6.10: Recovery curves for matrix cells 7 and 8 when using the RC method with scaling (RC (a)), the SCM and the TF.

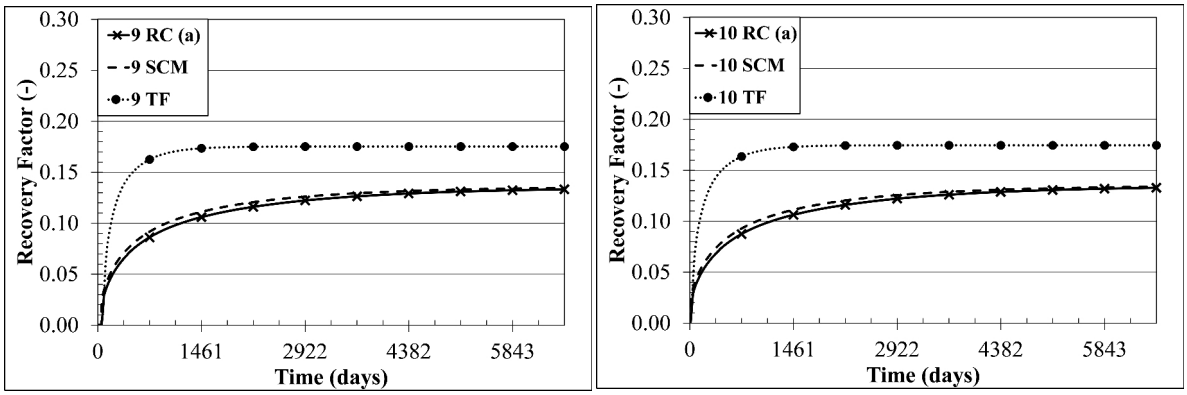

Figure 6.11: Recovery curves for matrix cells 9 and 10 when using the RC method with scaling (RC (a)), the SCM and the TF.

The saturation distribution of the SCM in the matrix can be exactly reproduced with the RC, but not with the RF. At day 362 (Figure 6.12) the matrix water saturation is already clearly higher for the TF in the lower parts of the matrix column. Both SCM and RC exhibit very similar saturation values. At the end of the calculation (Figure 6.13) all three calculations show an relatively constant water saturation in the matrix, except for the matrix cell 1, where oil resaturation occurred. However, for both SCM and RC the maximum oil saturation is 0.29, whereas the one for the TF is 0.32.

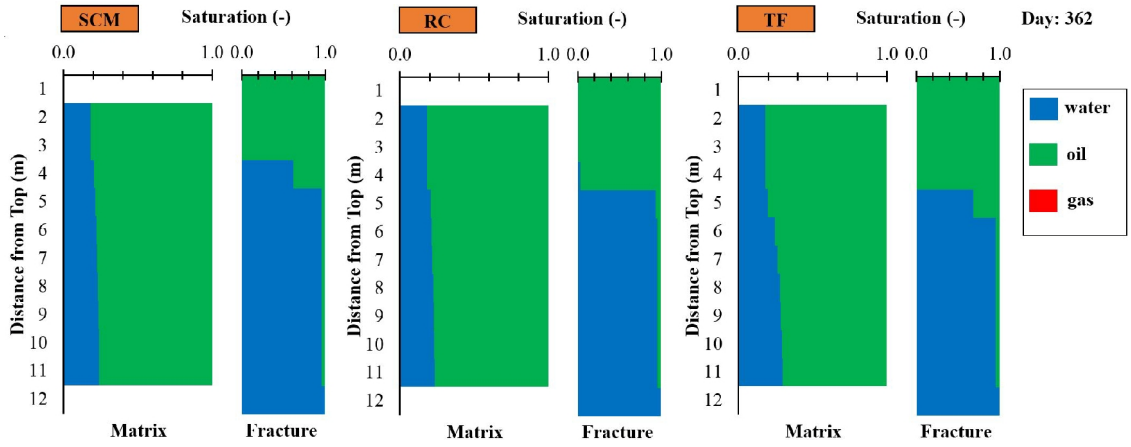

Figure 6.12: Saturation in the matrix and fracture for the SCM, RC and TF on day 362

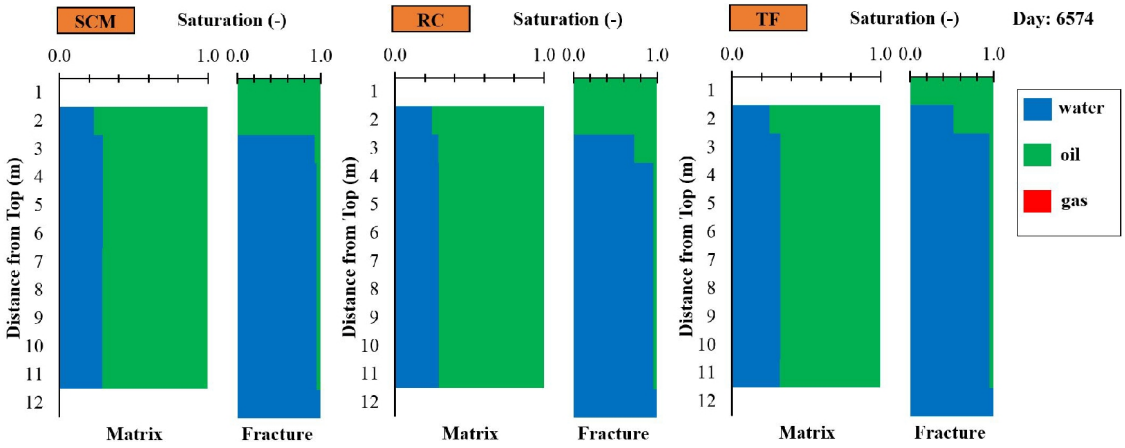

Figure 6.13: Saturation in the matrix and fracture for the SCM, RC and TF on day 6574

6.4.3 Setup 2

The cumulative oil and gas production as well as the HC-weighted average pressure can be seen in Figure 6.14. For setup 2 the cumulative oil and gas production is identical for the SCM, TF and RC. This is due to the fact that the gas did not break through at the oil producer Well 2 and because the pressure is identical for all setups, the produced solution gas is identical.

The average pressure in the column drops from 140 bar to 123 bar within the first 1247 days of calculation, which is an average pressure decline rate of 0.014 bar/day or 4.98 bar/year.

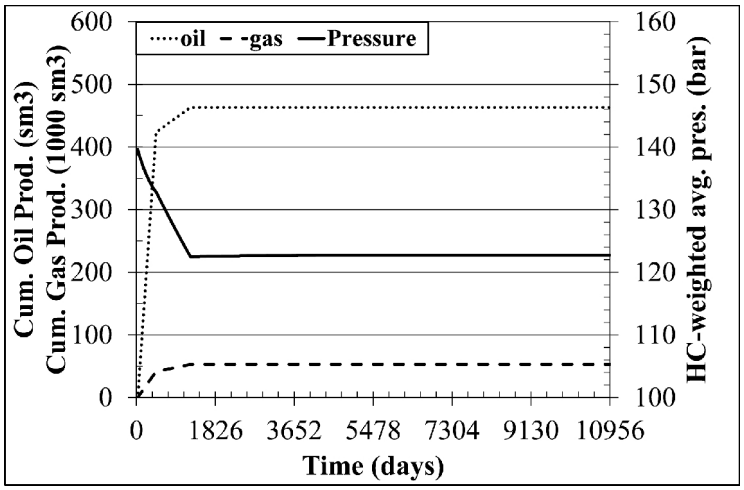

Figure 6.14: Setup 2: Average pressure and cumulative oil and gas production.

Figure 6.15 to Figure 6.19 show the recovery curves for all 10 matrix blocks. For the SCM and the RC, gasdrive occurs in cells 1 - 9, oil resaturation in cells 6 - 9 and purely expansion in cell 10. For the TF gasdrive only occurs for cells 1 - 7 and oil resaturation for cell 5 - 7, with cells 8 - 10 only under expansion drive.

For cells 1 - 5 the RC reproduces the SCM results accurately. The TF overpredicts the speed of recovery and the maximum recovery factor at the end of the calculation. For the TF, this results in a higher amount of oil in the fracture. In the fracture the mobile phases separate and oil resaturation occurs also in cell 5 for the TF, but not for the RC and SCM. The time when oil resaturation starts is matched accurately for the RC, as evident in cells 6, 7, 8 and 9.

An overview over the maximum recovery factors for all matrix cells and all calculation setups (SCM, RC (a) with $E_{R,max}$ and increment scaling, RC (b) with increment scaling, RC (c) without scaling and TF) can be seen in Table 6.4. It should be noted, that here the maximum achieved recovery factors are shown, and not the recovery factors at the end of calculation, which would be different for the matrix blocks where oil resaturation occurs. For setup 2 it is evident, that all RC variants reproduce the results of the SCM more accurately than the TF. Among the RC variants, RC (a) and RC (b) achieve the best results, whereas RC (c) overpredicts the maximum recovery factor slightly. In this example the increment scaling of the RC clearly has more influence on the results than the scaling of $E_{R,max}$.

Table 6.4: Maximum recovery factors for Setup 2

	Maximum Recovery Factor $E_{R,max}$ (-)				
Matrix Cell	**SCM**	**RC (a)**	**RC (b)**	**RC (c)**	**TF**
1	0.331	0.323	0.323	0.352	0.425
2	0.330	0.322	0.330	0.352	0.424
3	0.329	0.321	0.329	0.352	0.424
4	0.329	0.320	0.328	0.351	0.423
5	0.328	0.319	0.327	0.351	0.354
6	0.269	0.236	0.235	0.234	0.219
7	0.170	0.163	0.163	0.164	0.089
8	0.114	0.113	0.113	0.114	0.023
9	0.073	0.061	0.060	0.058	0.022
10	0.061	0.041	0.041	0.041	0.022

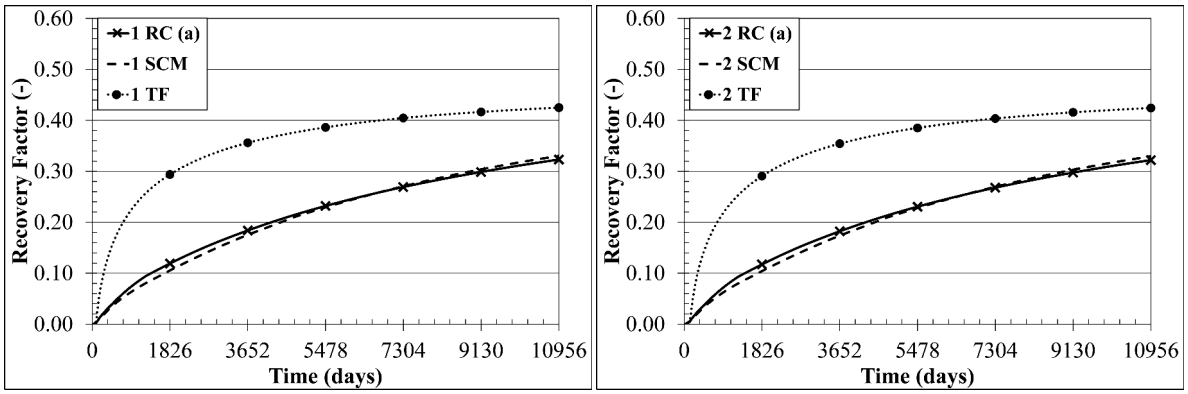

Figure 6.15: Recovery curves for matrix cells 1and 2 when using the RC method with scaling (RC (a)), the SCM and the TF.

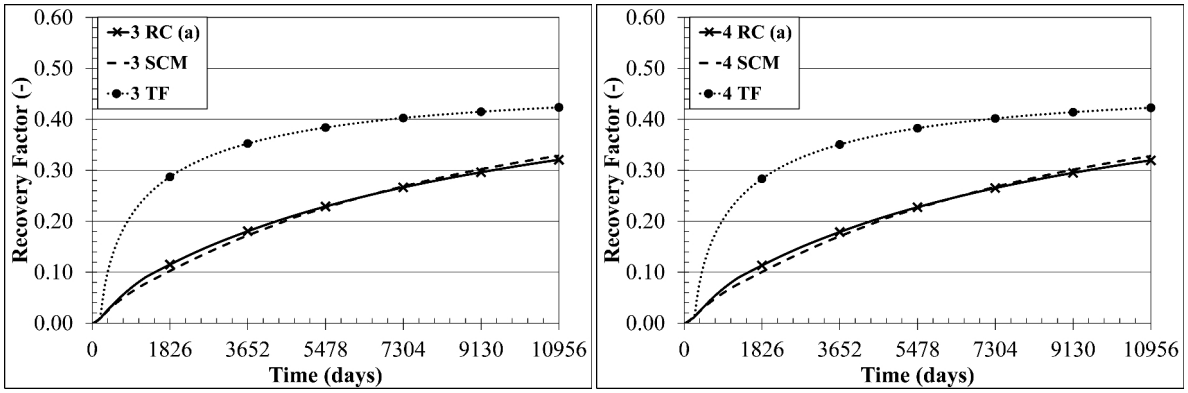

Figure 6.16: Recovery curves for matrix cells 3 and 4 when using the RC method with scaling (RC (a)), the SCM and the TF.

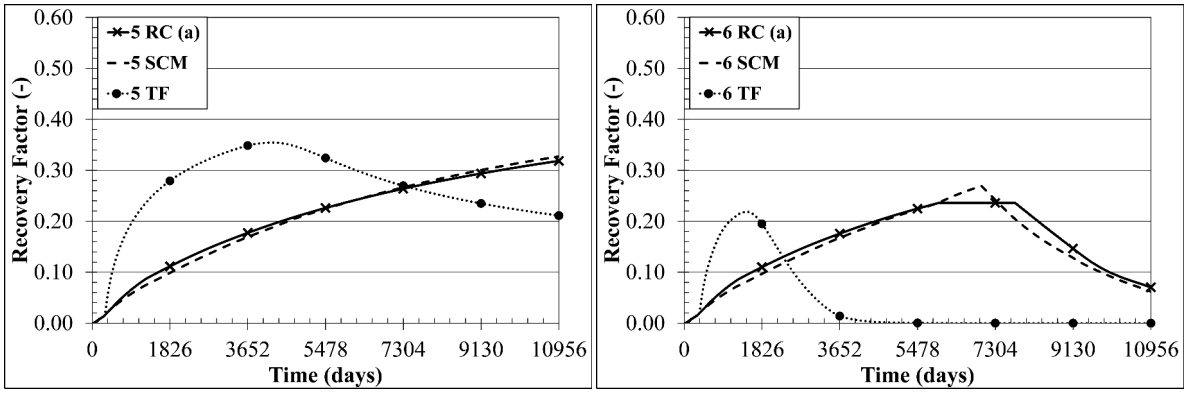

Figure 6.17: Recovery curves for matrix cells 5and 6 when using the RC method with scaling (RC (a)), the SCM and the TF.

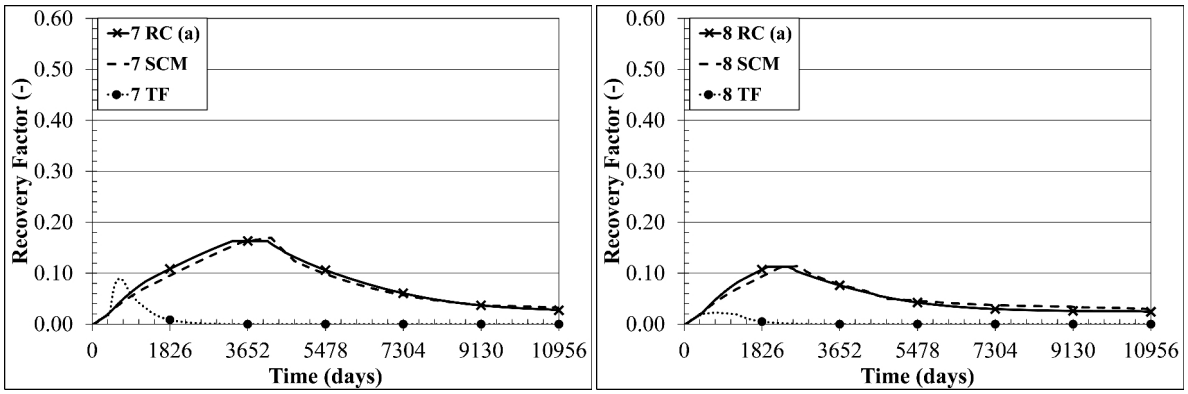

Figure 6.18: Recovery curves for matrix cells 7 and 8 when using the RC method with scaling (RC (a)), the SCM and the TF.

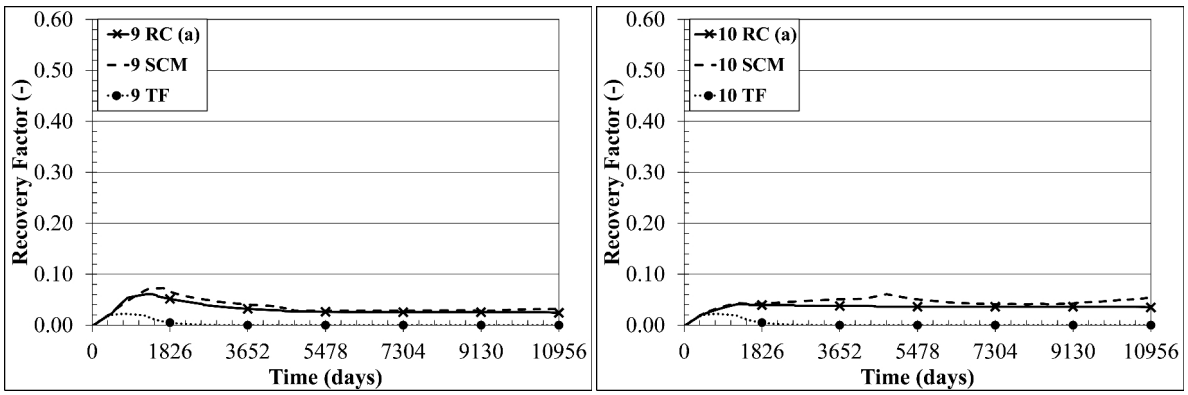

Figure 6.19: Recovery curves for matrix cells 9 and 10 when using the RC method with scaling (RC (a)), the SCM and the TF.

6.4.4 Setup 3

The cumulative oil and water production and the average pressure of the column model for the Single Continuum Model (SCM), the transfer function (TF) and the recovery curve method (RC) can be seen in Figure 6.20. Oil is produced from the top of the column and water is injected with a stepwise declining pressure at the bottom of the column. The pressure is reduced by 0.2 bar each month, but at the beginning of the calculation the HC-weighted average pressure shows a steeper decline. This is for the same reason as discussed for setup 1: Water displaced oil from the bottom of the model, where the pressure is higher and therefore the HC-weighted pressure is reduced. In the first 2372 days the pressure drops from 160 to 142 bar, which is a decline rate of 0.008 bar/day or 2.77 bar/year.

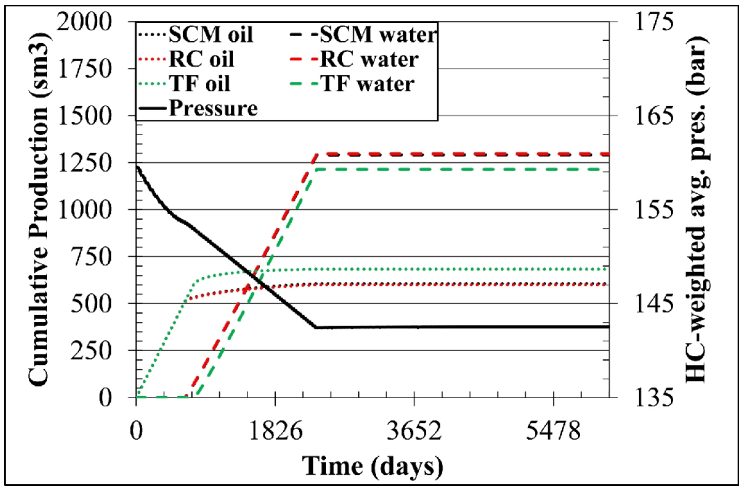

Figure 6.20: Setup 3: Average pressure and cumulative oil and water production when using the recovery curve method, the TF and the SCM.

Figure 6.21 to Figure 6.25 show the calculated RCs for setup 3. It can be seen that all matrix cells show a period of expansion followed by waterdrive. The change in drive mechanism can be identified by the sudden change in slope of the curve. As waterdrive starts when the water saturation in the fracture adjacent to a matrix cell is filled with water, the WOC movement can be identified. The WOC movement is identical for the SCM and the RC. When using the TF the WOC is moving upwards at a slower pace, as marked by the delayed start of waterdrive. Naturally, for the top blocks this effect is more evident than for the lower ones.

$E_{R,max}$ when using the TF is around 0.20, which is significantly higher than when using the RC or for the SCM, where $E_{R,max}$ is around 0.15. Also here the effect at the top matrix cell 1 $E_{R,max}$ is lower than for cell 10 can be observed in all calculations. The final recovery factors of cell 01 are 0.146 for the SCM, 0.149 for the RC and 0.196 for the TF. At the bottom cell they are 0.166 for the SCM, 0.167 for the RC and 0.205 for the TF. This shows that the RC can handle the different pressure history of the individual cells and predict the final recovery factor very accurately. The reason for the difference in the ultimate recovery factor between the TF and the SCM/RC will be discussed and explained in detail in Section 6.5.

An overview over the maximum recovery factors for all matrix cells and all calculation setups (SCM, RC (a) with $E_{R,max}$ and increment scaling, RC (b) with increment scaling, RC (c) without scaling and TF) can be seen in Table 6.5. It is evident that all RC option give more accurate results than the TF, but the change of the maximum recovery factors with depth is not modeled for RC (b) and RC (c).

Table 6.5: Maximum recovery factors for Setup 3

	Maximum Recovery Factor $E_{R,max}$ (-)				
Matrix Cell	**SCM**	**RC (a)**	**RC (b)**	**RC (c)**	**TF**
1	0.146	0.150	0.149	0.149	0.197
2	0.150	0.150	0.147	0.148	0.200
3	0.151	0.154	0.149	0.150	0.202
4	0.154	0.155	0.148	0.148	0.204
5	0.156	0.159	0.150	0.150	0.205
6	0.157	0.161	0.150	0.150	0.206
7	0.160	0.162	0.149	0.149	0.206
8	0.161	0.165	0.150	0.150	0.206
9	0.164	0.166	0.149	0.149	0.206
10	0.166	0.168	0.150	0.150	0.196

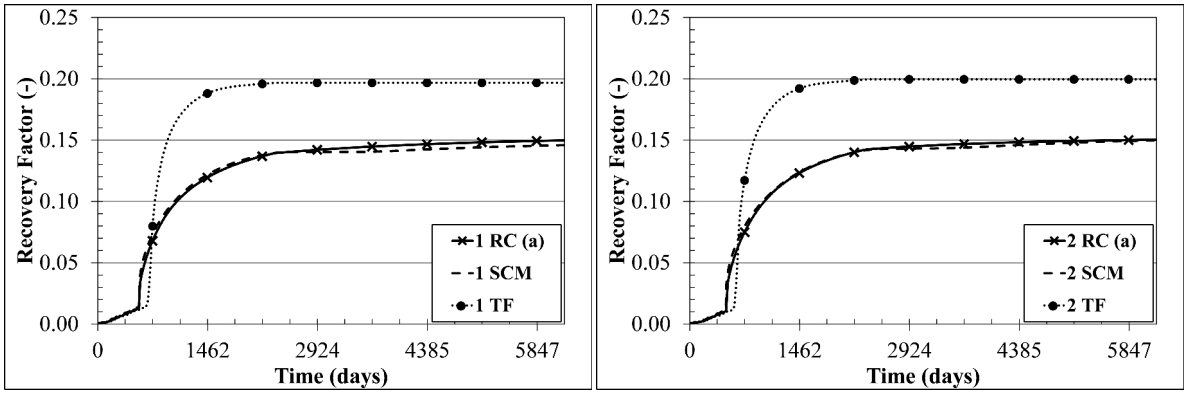

Figure 6.21: Recovery curves for matrix cells 1 and 2 when using the RC method with scaling (RC (a)), the SCM and the TF.

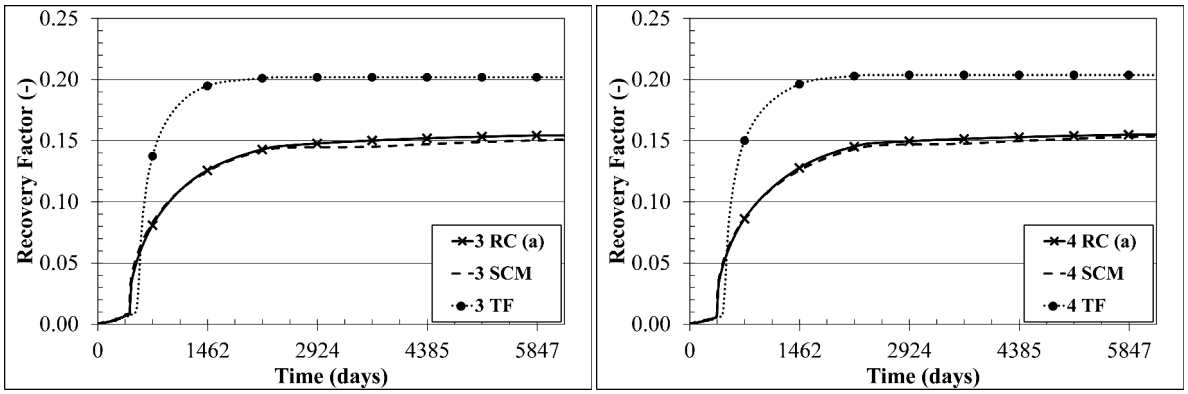

Figure 6.22: Recovery curves for matrix cells 3 and 4 when using the RC method with scaling (RC (a)), the SCM and the TF.

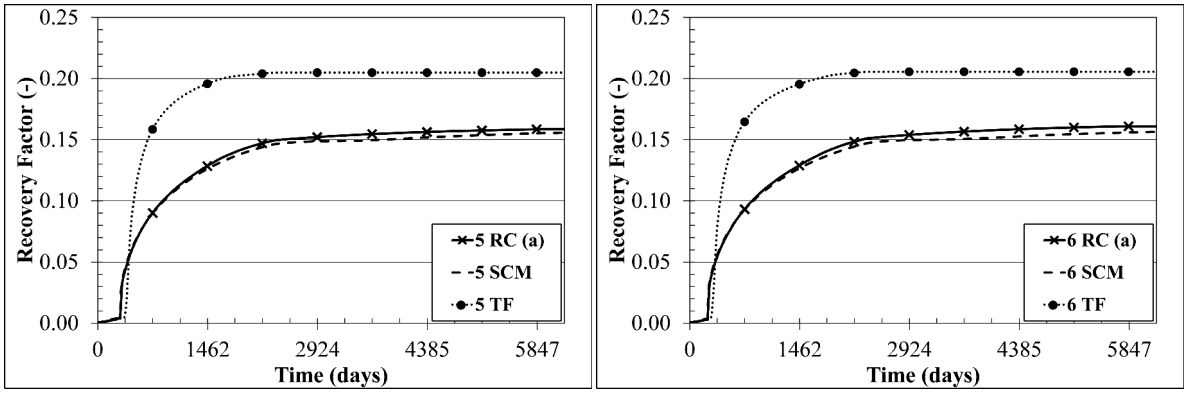

Figure 6.23: Recovery curves for matrix cells 5 and 6 when using the RC method with scaling (RC (a)), the SCM and the TF.

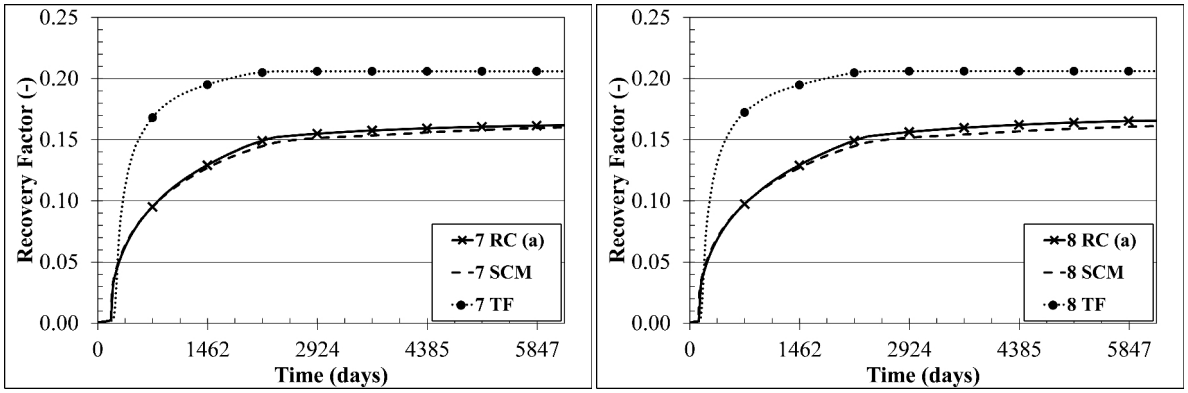

Figure 6.24: Recovery curves for matrix cells 7 and 8 when using the RC method with scaling (RC (a)), the SCM and the TF.

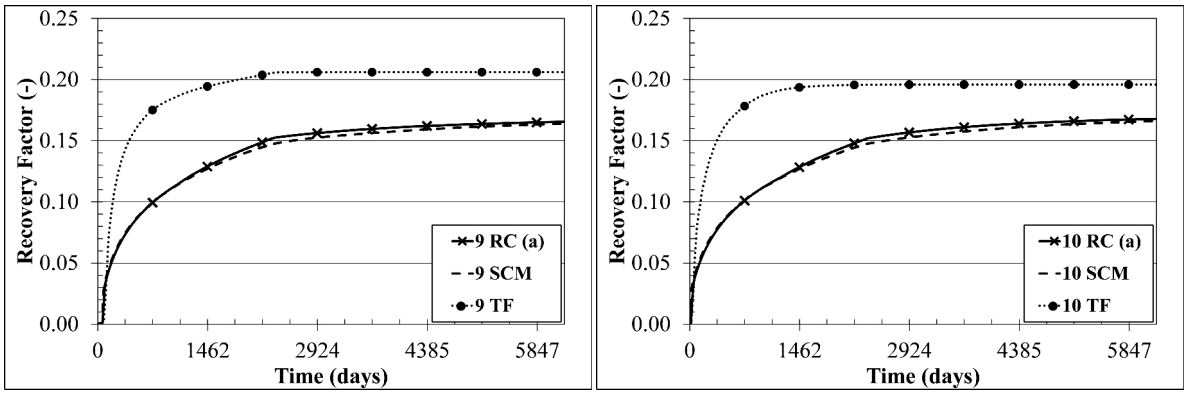

Figure 6.25: Recovery curves for matrix cells 9 and 10 when using the RC method with scaling (RC (a)), the SCM and the TF.

6.4.5 Setup 4

The cumulative oil production and the average pressure of the column model for the Single Continuum Model (SCM), the transfer function (TF) and the recovery curve method (RC) can be seen in Figure 6.26. The oil production is identical for all calculations, as the water did not break through at Well 1. Oil is produced from the top of the column and water is injected with a constant pressure at the bottom of the column. The average HC-weighted pressure declining in the beginning, because oil is displaced in the bottom of the column, where the pressure is higher. This is the same effect as described for setup 1.

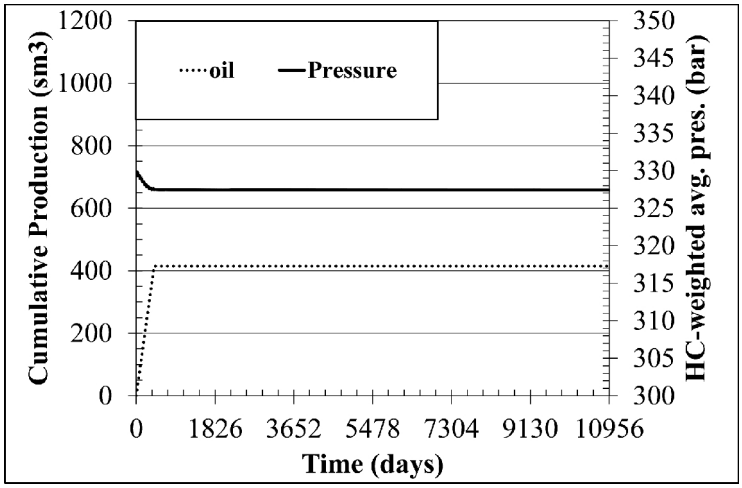

Figure 6.26: Setup 4: Average pressure and cumulative oil production.

Figure 6.27 to Figure 6.31 show the RCs for all 10 matrix blocks. Waterdrive occurs in cells 3 - 10. It can be seen that both the RC and the TF match the results of the SCM well. The TF slightly underpredicts the speed of recovery up to a recovery factor of 0.45, but the deviation from the SCM is only minimal.

An overview over the maximum recovery factors for all matrix cells and all calculation setups (SCM, RC (a) with $E_{R,max}$ and increment scaling, RC (b) with increment scaling, RC (c) without scaling and TF) can be seen in Table 6.6. For setup 4, using the water-wet SCAL data, all tested transfer models accurately predict $E_{R,max}$.

.

Table 6.6: Maximum recovery factors for Setup 4

	Maximum Recovery Factor $E_{R,max}$ (-)				
Matrix Cell	**SCM**	**RC (a)**	**RC (b)**	**RC (c)**	**TF**
1	0.001	0.001	0.001	0.001	0.001
2	0.001	0.001	0.001	0.001	0.015
3	0.297	0.327	0.323	0.321	0.312
4	0.426	0.430	0.429	0.429	0.399
5	0.497	0.503	0.502	0.503	0.471
6	0.512	0.511	0.512	0.513	0.508
7	0.512	0.511	0.512	0.514	0.508
8	0.512	0.511	0.512	0.514	0.508
9	0.512	0.511	0.512	0.514	0.508
10	0.512	0.511	0.512	0.514	0.508

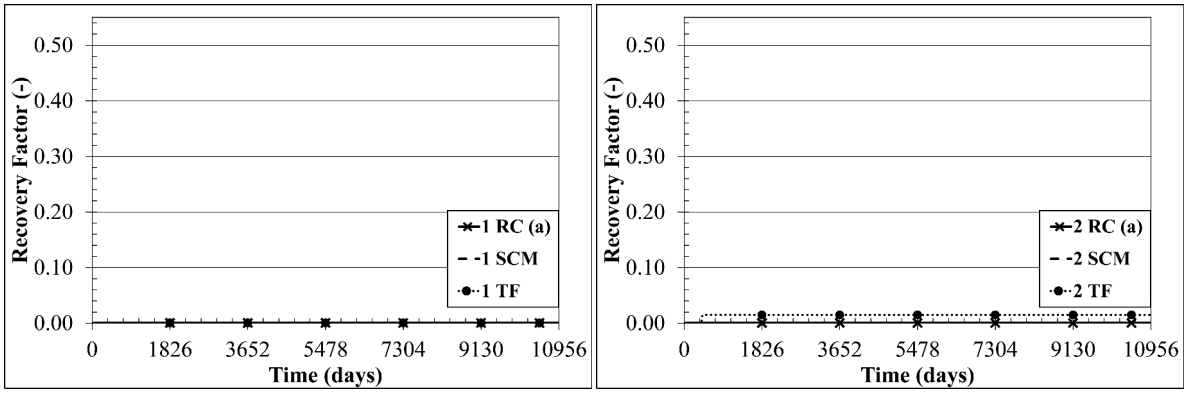

Figure 6.27: Recovery curves for matrix cells 1 and 2 when using the RC method with scaling (RC (a)), the SCM and the TF.

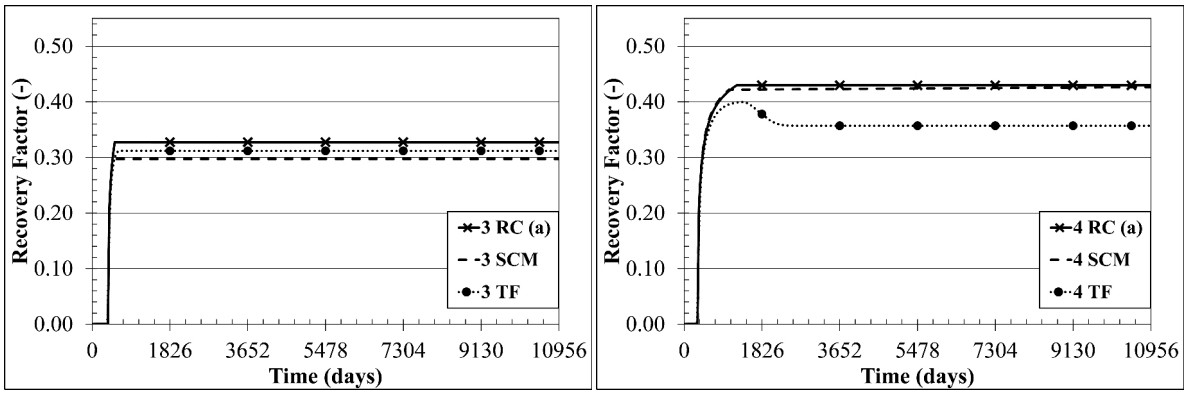

Figure 6.28: Recovery curves for matrix cells 3 and 4 when using the RC method with scaling (RC (a)), the SCM and the TF.

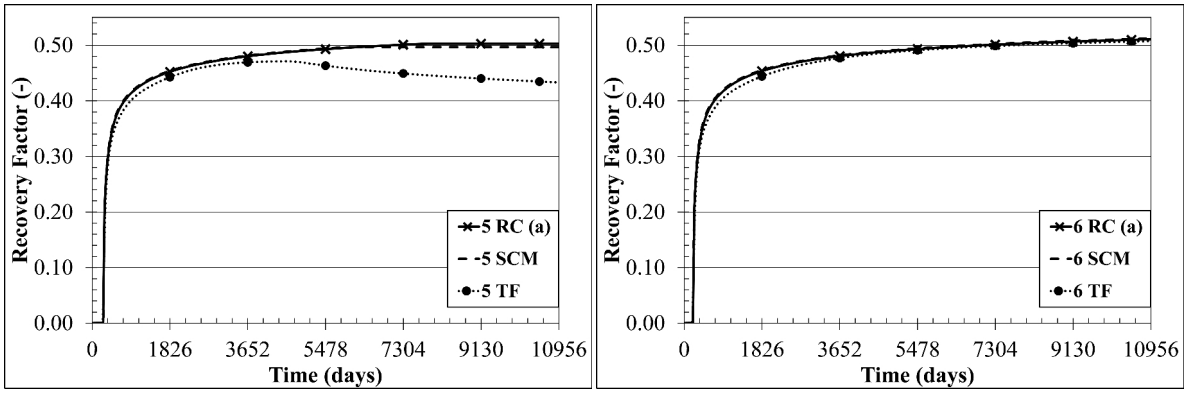

Figure 6.29: Recovery curves for matrix cells 5 and 6 when using the RC method with scaling (RC (a)), the SCM and the TF.

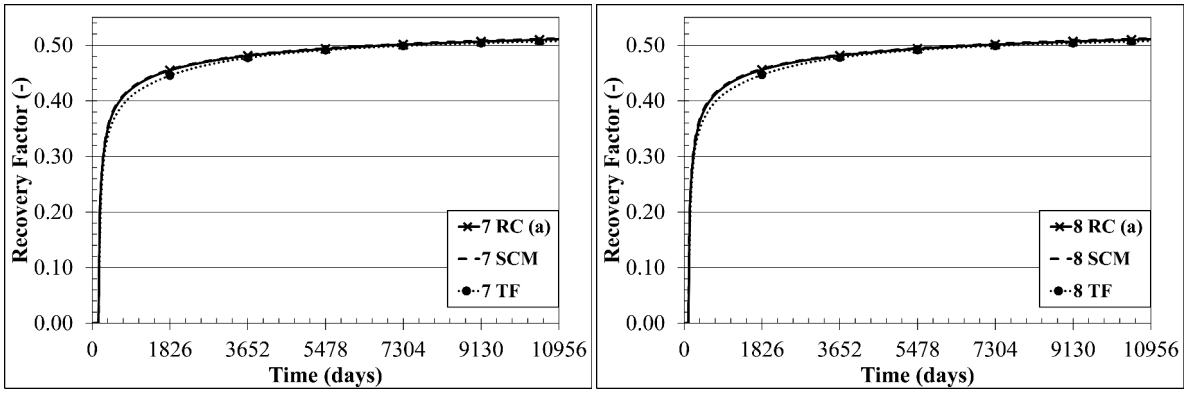

Figure 6.30: Recovery curves for matrix cells 7 and 8 when using the RC method with scaling (RC (a)), the SCM and the TF.

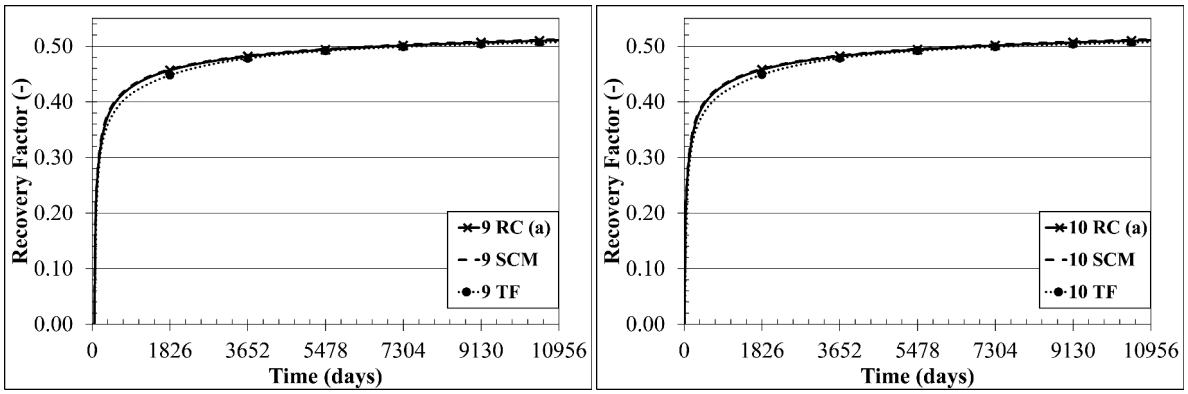

Figure 6.31: Recovery curves for matrix cells 9 and 10 when using the RC method with scaling (RC (a)), the SCM and the TF.

6.4.6 Setup 5

The cumulative oil and gas production as well as the HC-weighted average pressure can be seen in Figure 6.32. For setup 5 the cumulative oil and gas production is identical for the SCM, TF and RC. This is due to the fact that the gas did not break through at the oil producer Well 2 and because the pressure is identical for all setups, the produced solution gas is identical.

The average pressure in the column drops from 200 bar to 166 bar within the first 1247 days of calculation, which is an average pressure decline rate of 0.027 bar/day or 9.95 bar/year.

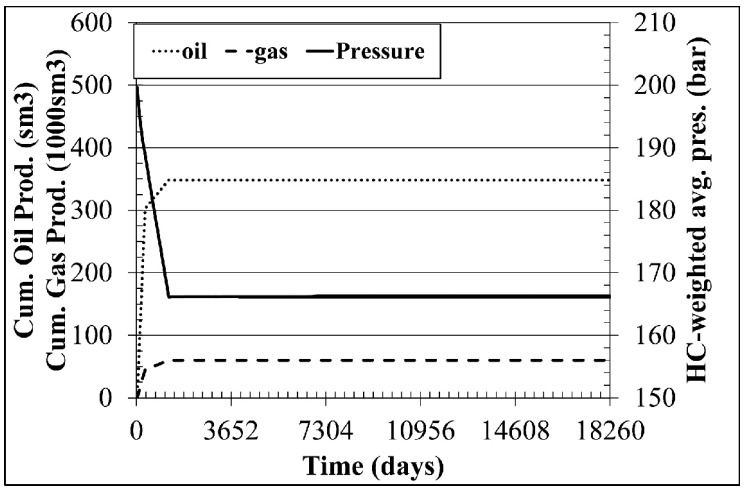

Figure 6.32: Setup 5:Average pressure and cumulative oil and gas production.

Table 6.7 shows the maximum recovery factors for all matrix cells and all calculation setups (SCM, RC (a) with $E_{R,max}$ and increment scaling, RC (b) with increment scaling, RC (c) without scaling and TF). RC (a) matches the SCM results most accurately. Matrix cells 1-6 have a similar $E_{R,max}$ for all calculation modes. Matrix cell 7 is matched more accurately by all three RC modes, the TF exhibits a lower $E_{R,max}$ for cell 7. Also in matrix cell 8 discrepancies occur

due to the different phase contact movement between the calculation modes.

Figure 6.33 to Figure 6.37 show the RCs for all 10 matrix blocks. Matrix cells 1-8 experience gasdrive in the SCM and RC. For the TF no gasdrive occurs in matrix cell 8, since the oil-gas contact never reached the depth of this cell.

Matrix cells 1-6 exhibit expansion followed by gasdrive and no oil resaturation. It can be seen that the RC matches the results of the SCM accurately. The calculated $E_{R,max}$ is underpredicted by roughly 0.002, which is insignificant. The TF overpredicts the speed of oil recovery. $E_{R,max}$ is also overpredicted by approximately 0.01.

Matrix cell 7 also underground oil resaturation, which can be seen in all calculations. In cell 7 the maximum recovery factor when using the RC is by 0.01 higher than for the SCM. The begin of oil-resaturation is delayed. But once oil resaturation also starts for the RC the slope of the decrease in RF is similar to the SCM.

Matrix cells 8 only has a very short time of gasdrive and cells 9 and 10 undergo expansion only.

Table 6.7: Maximum recovery factors for Setup 5

	Maximum Recovery Factor $E_{R,max}$ (-)				
Matrix Cell	**SCM**	**RC (a)**	**RC (b)**	**RC (c)**	**TF**
1	0.257	0.255	0.240	0.246	0.266
2	0.257	0.255	0.240	0.246	0.266
3	0.256	0.254	0.240	0.246	0.265
4	0.256	0.253	0.240	0.246	0.265
5	0.256	0.253	0.240	0.246	0.264
6	0.256	0.252	0.239	0.246	0.264
7	0.190	0.200	0.203	0.202	0.092
8	0.100	0.051	0.077	0.052	0.024
9	0.059	0.066	0.066	0.066	0.024
10	0.059	0.066	0.066	0.066	0.024

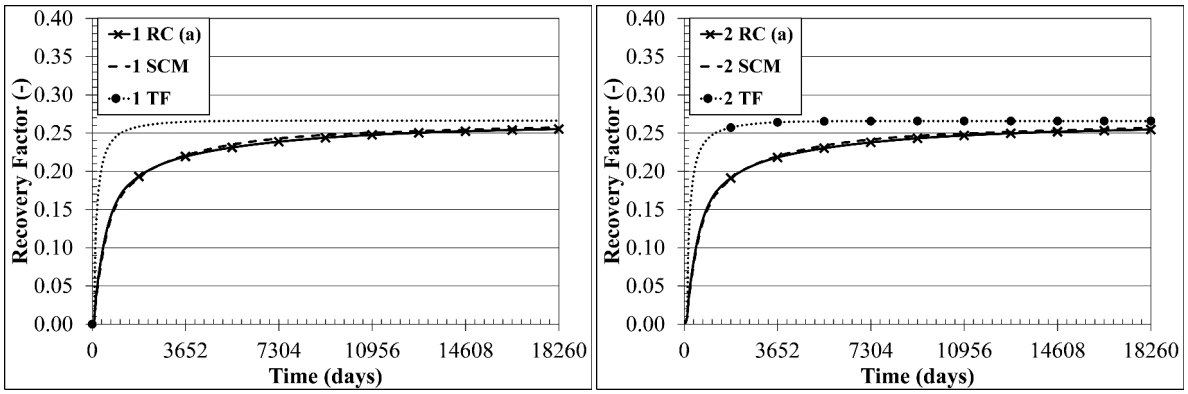

Figure 6.33: Recovery curves for matrix cells 1 and 2 when using the RC method with scaling (RC (a)), the SCM and the TF.

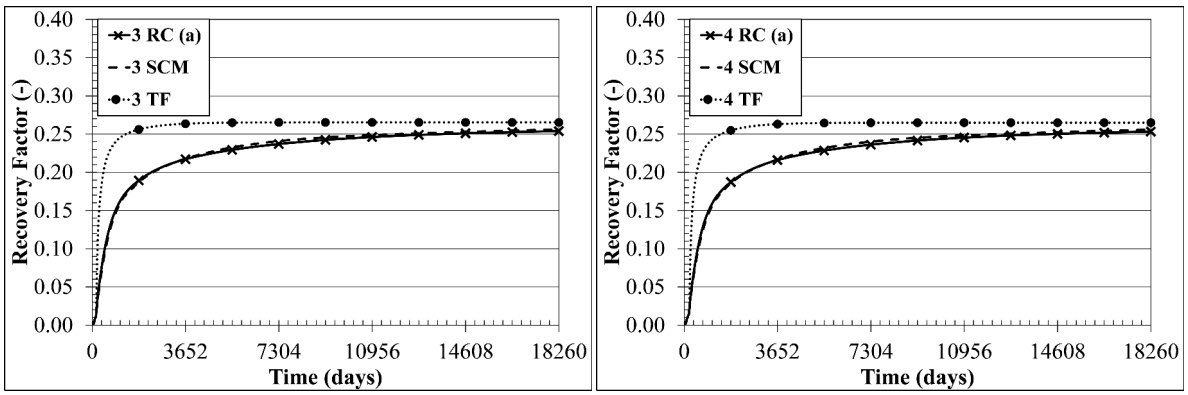

Figure 6.34: Recovery curves for matrix cells 3 and 4 when using the RC method with scaling (RC (a)), the SCM and the TF.

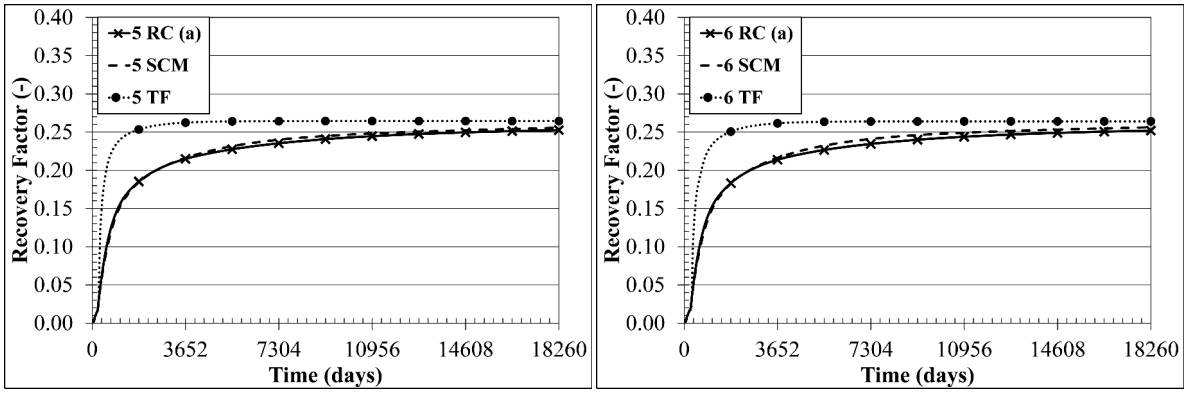

Figure 6.35: Recovery curves for matrix cells 5 and 6 when using the RC method with scaling (RC (a)), the SCM and the TF.

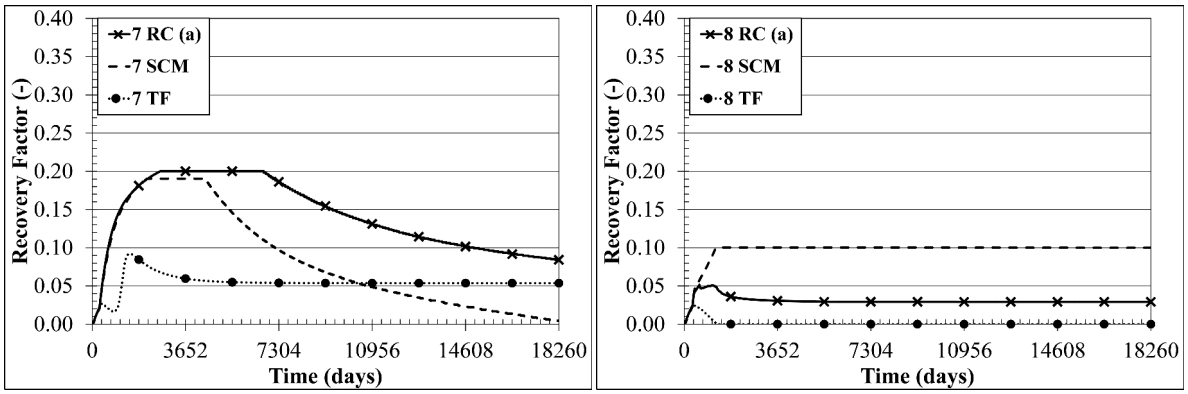

Figure 6.36: Recovery curves for matrix cells 7 and 8 when using the RC method with scaling (RC (a)), the SCM and the TF.

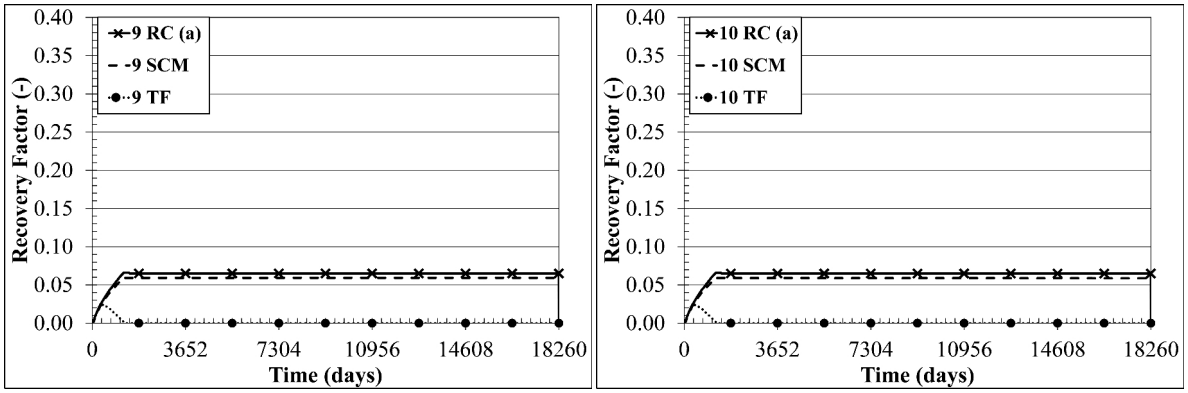

Figure 6.37: Recovery curves for matrix cells 9 and 10 when using the RC method with scaling (RC (a)), the SCM and the TF.

6.4.7 Setup 6

The cumulative oil and water production as well as the HC-weighted average pressure can be seen in Figure 6.38. For setup 6 the cumulative oil and water production is identical for the SCM, TF and RC. Oil is produced from the top of the column and water is injected with a stepwise declining pressure at the bottom of the column. The pressure is reduced by 0.3 bar each month, but at the beginning of the calculation the HC-weighted average pressure shows a steeper decline. This is for the same reason as discussed for setup 1: Water displaced oil from the bottom of the model, where the pressure is higher and therefore the HC-weighted pressure is reduced. The average pressure in the column drops from 283 bar to 248 bar within the first 3469 days of calculation, which is an average pressure decline rate of 0.01 bar/day or 3.68 bar/year.

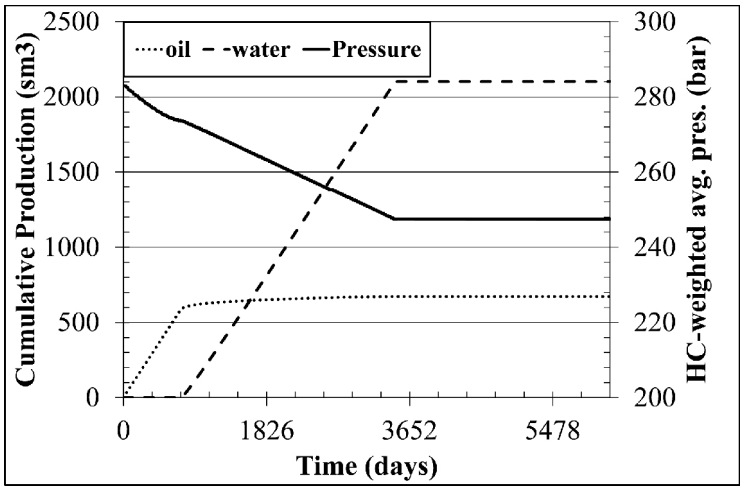

Figure 6.38: Setup 6: Average pressure and cumulative oil and water production.

An overview over the maximum recovery factors for all matrix cells and all calculation setups (SCM, RC (a) with $E_{R,max}$ and increment scaling, RC (b) with increment scaling, RC (c) without scaling and TF) can be seen in Table 6.8. All transfer models achieve a similar result, with RC (a) being the closest to the SCM.

Figure 6.39 to Figure 6.43 shows the RCs for the SCM, RC (a) and the TF. The TF slightly underpredicts the speed of oil recovery in the early phases of waterdrive up to RF values of 0.45

.

Table 6.8: Maximum recovery factors for Setup 6

	Maximum Recovery Factor $E_{R,max}$ (-)				
Matrix Cell	**SCM**	**RC (a)**	**RC (b)**	**RC (c)**	**TF**
1	0.523	0.526	0.514	0.514	0.515
2	0.521	0.527	0.514	0.514	0.516
3	0.526	0.527	0.515	0.515	0.516
4	0.527	0.527	0.515	0.515	0.517
5	0.522	0.527	0.516	0.515	0.517
6	0.529	0.527	0.516	0.515	0.518
7	0.529	0.528	0.517	0.516	0.519
8	0.523	0.528	0.517	0.516	0.519
9	0.532	0.528	0.517	0.516	0.519
10	0.529	0.527	0.517	0.516	0.519

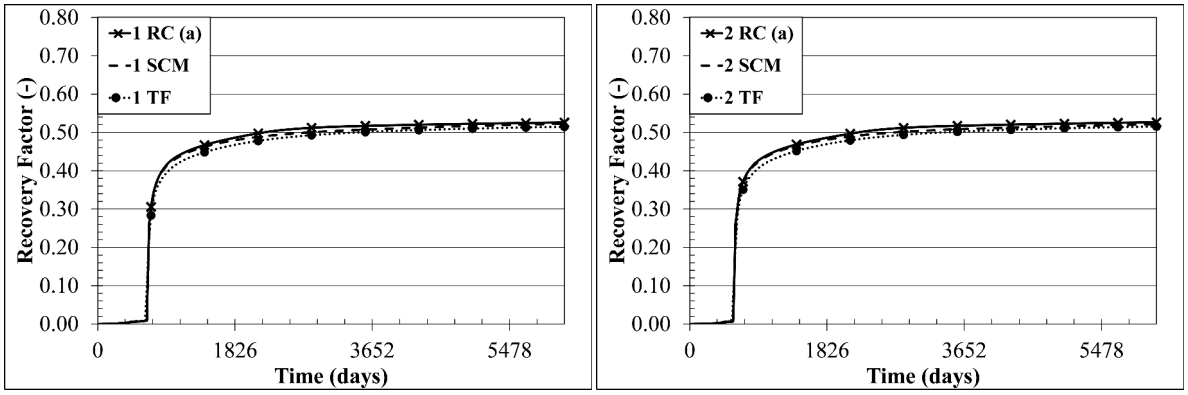

Figure 6.39: Recovery curves for matrix cells 1 and 2 when using the RC method with scaling (RC (a)), the SCM and the TF.

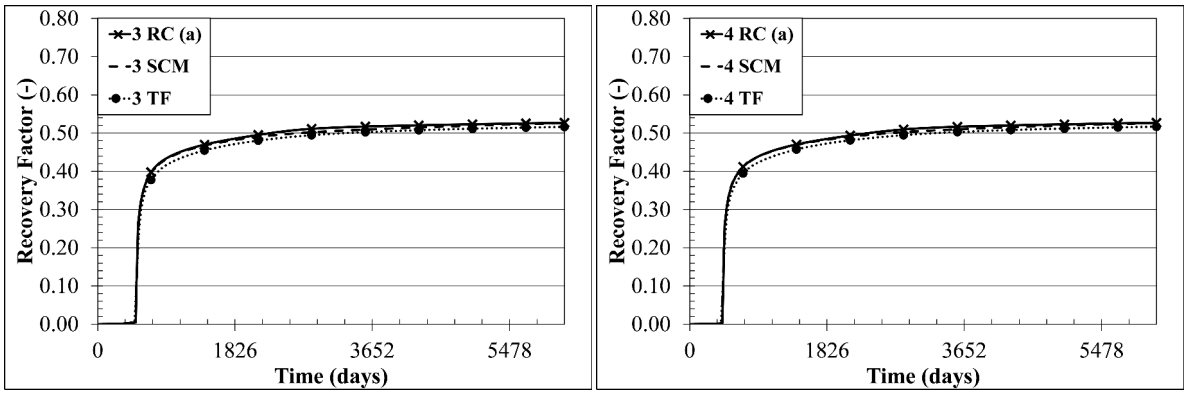

Figure 6.40: Recovery curves for matrix cells 3 and 4 when using the RC method with scaling (RC (a)), the SCM and the TF.

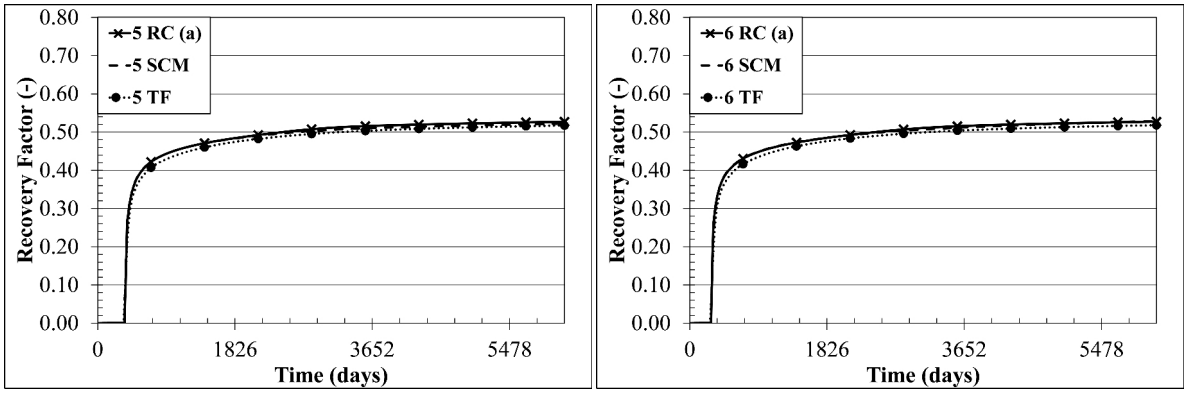

Figure 6.41: Recovery curves for matrix cells 5 and 6 when using the RC method with scaling (RC (a)), the SCM and the TF.

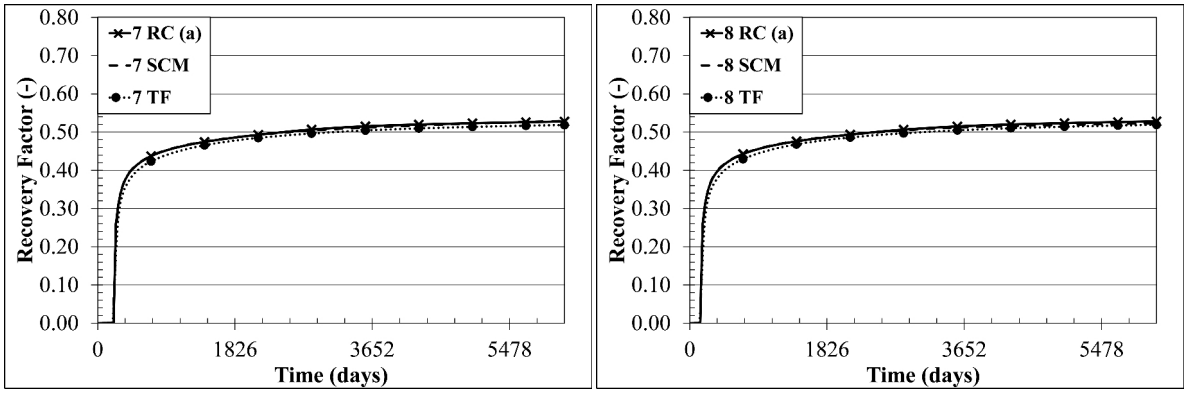

Figure 6.42: Recovery curves for matrix cells 7 and 8 when using the RC method with scaling (RC (a)), the SCM and the TF.

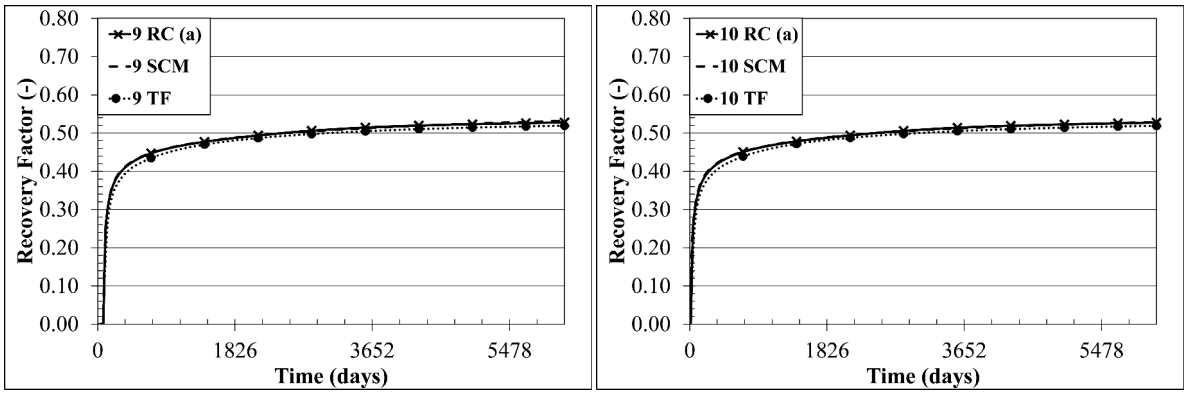

Figure 6.43: Recovery curves for matrix cells 9 and 10 when using the RC method with scaling (RC (a)), the SCM and the TF.

6.5 Explanation of the Difference in $E_{R,max}$ between TF and SCM/RC

Setups 1 and 3 show significant differences in the estimation of the maximum recovery factor between the SCM/RC and the TF. These setups are waterdrive and the SCAL data of an oil-wet rock is used.

The maximum achievable matrix recovery factor is defined by the equilibrium between capillary and gravitational forces. In the calculation some model for determining the forces have to be found. The capillary forces are well defined by the capillary pressure (P_c) function. The SCM considers it for all small cells of the SMB individually, which means the P_c is not constant in matrix. The RC considers these non-uniform P_c also because it is already defined with the input RC. The TF determines the P_c based on the average matrix saturation and does not consider the variation within the matrix blocks.

For the gravitational forces the SCM inherently considers them because both matrix and fracture are finely gridded. When the RC is used, the gravitational forces are already included in the input RC and only slightly adjusted for changing pressures. In the TF a mathematical model for the gravitational forces is used, which is based on average matrix and fracture properties (average saturation and pressure). Various gravity drainage models exist, but all use average properties of the matrix.

When the TF is used, the ultimate recovery factor can easily determined by writing the balance of forces:

$$\Phi_{wm} - \Phi_{wf} = p_{om} - p_{of} - P_{cwom} + P_{cwof} + P_{hwom} - P_{hwof} \tag{6.1}$$

where the subscript *f* denotes the fracture and *m* the matrix. P_{cwo} is the water-oil capillary pressure, P_{hwo} the hydrostatic pressure difference and po the average oil pressure. In the fracture (P_{cwof}) is assumed to be 0. When using the PVT data set 1 the individual forces and the resulting difference can be seen in Figure 6.44. In this figure the net hydrostatic pressure, P_{hwof}-P_{hwom}, the imbibition capillary pressure and the resulting net potential, Φ_{wf}-Φ_{wm}, is shown. It is assumed that the pressure in the matrix and fracture is identical. It can be seen that the average water saturation *Sw* at the equilibrium of the forces is 0.33, which is equivalent to an ultimate recovery factor of 0.18. This value for $E_{R,max}$ is also reproduced with the numerical calculation in setup 1.

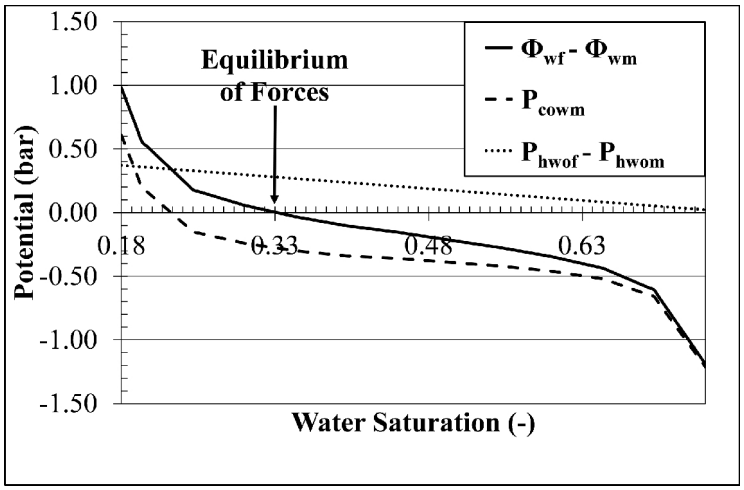

Figure 6.44: Equilibrium of forces for waterdrive when using the TF

In the SMB calculation, the saturation is not uniform. At ultimate recovery the equilibrium between gravitational and capillary forces will result in a vertical saturation distribution, as shown in Figure 6.45. At the top of the SMB the water saturation is lower and at the bottom higher than the average saturation determined for the DCM. Averaging the saturation of the SMB results in a water saturation that is lower than the one of the DCM using the TF. For the SMB the average Sw is 0.29, which is equivalent to an ultimate recovery factor of 0.13.

Figure 6.46 show the vertical distribution of the matrix, fracture and capillary pressure in the SMB. It can be clearly seen that in equilibrium, the average matrix pressure is lower than the average fracture pressure. The difference between the two pressures is exactly the capillary pressure, determined for the saturation at the specific depth.

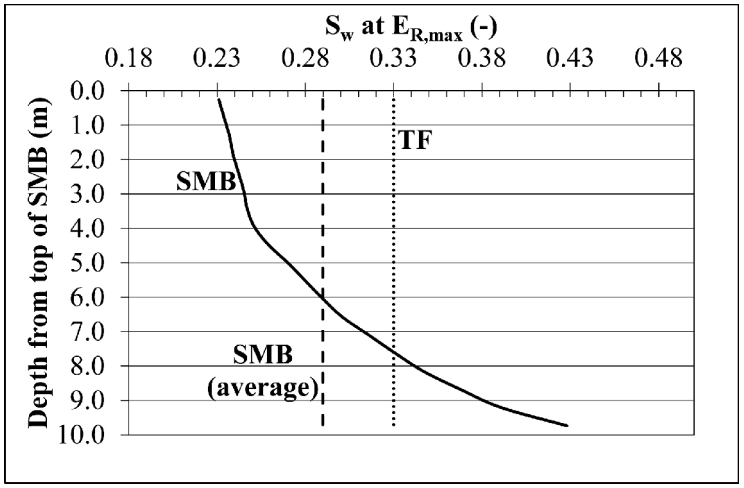

Figure 6.45: Water saturation in the matrix block after waterdrive at ultimate recovery.

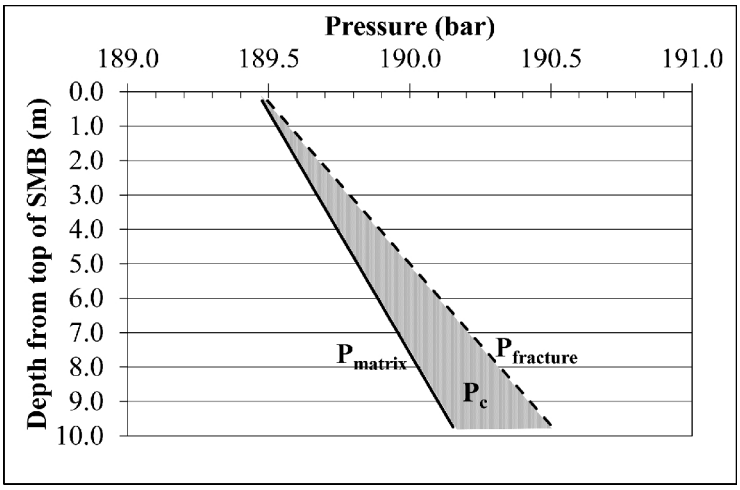

Figure 6.46: Vertical matrix, fracture and capillary pressure distribution of the SMB after waterdrive at ultimate recovery.

It can be concluded, that when the TF is used, the determination of the capillary pressure based on average saturations together with the used gravity drainage model is not able to accurately predict the final average water saturation in the SMB after waterdrive. Therefore, e.g. in setup 1 the $E_{R,max}$ predicted by the TF is higher than the on calculated by the fine grid SMB model.

For the water-wet SCAL data this effect is not observed, e.g. in setup 4. This can be explained by the fact that the equilibrium between capillary and gravitational forces occurs already very near to the residual oil saturation after waterdrive based on the relative permeability input data. Nearly the entire recovery process occurs with a positive oil-water capillary pressure, resulting in spontaneous imbibition of oil up to a water saturation of roughly 0.71. Since only a very small part of the imbibition capillary pressure curve is in the negative (from $S_w = 0.71$ to $S_w = 0.75$) the vertical distribution of the water saturation within the SMB is nearly homogeneous. Therefore, the oil recovery when using the water-wet SCAL data, is dominated by capillary forces and the gravitational forces have only little influence on the final recovery.

Generally, the RC can be used independently of the wettability of the rock, since the information about the capillary and gravitational forces as well as their variation within the SMB are already included in the input RC. When the TF is used, only average properties can be considered and the results will also depend on the chosen gravity drainage model.

6.6 Influence of Recovery Curve Scaling

All setups have been calculated with three modes for the RCM, to show the influence of the in Chapter 5 introduced scaling options. The variance are RC (a), RC (b) and RC (c), where the letter in the brackets denotes the type of scaling used:

a.) $E_{R,max}$ and increment scaling
b.) only increment scaling and
c.) without and scaling of the RC.

To highlight the differences, also an error-plot will be shown, where on the vertical axis the absolute error in RF between the SCM and the other models will be shown. If the error is positive, the transfer model overpredicts the RF at this point in time, if it is negative the RF is underpredicted. The TF results and errors are also shown, but will not be discussed in this section. They are included to illustrate the magnitude of error, when the TF is used, compared to the RCM options.

Figure 6.47 shows the RC for all calculation setups (left) and the error in recovery factor (right) for setup 1, in which waterdrive occurs. It can be seen that only the scaling of $E_{R,max}$ has a significant influence on the RC. RC (b) and RC (c) produce identical result. In this case the calculation is at a pressure, which is 30 bar above bubble point pressure, at which the input RC is calculated. As shown in Section 5.4.2.1, the gravitational force is lower at this higher pressure, which is not considered by RC (a) or RC (b). As the pressure remains nearly constant during the calculation, the scaling of $E_{R,max}$ due to gravitational forces it the only significant scaling option.

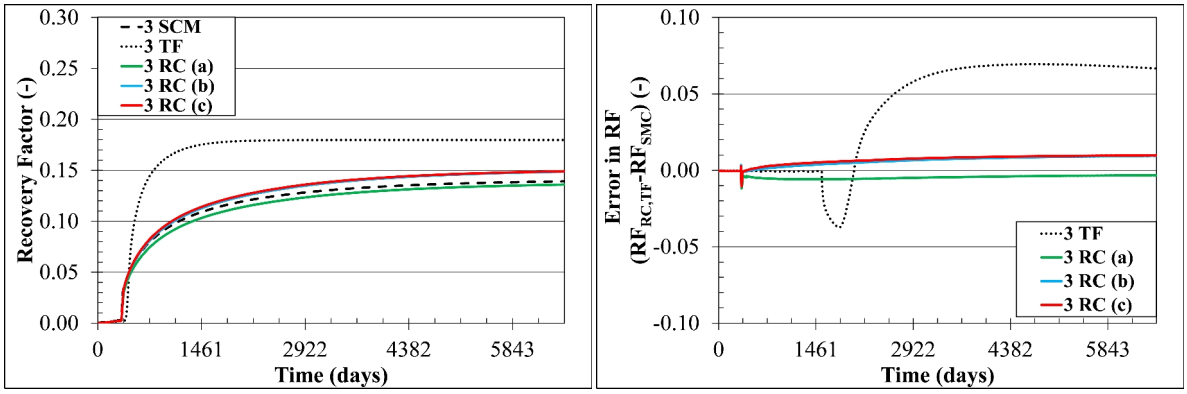

Figure 6.47: Setup 1: Recovery factor and error in recovery factor for cell 3.

Figure 6.48 and Figure 6.49 show the RCs (left) and the error in recovery factor (right) for cells 2 and 7 setup 2, in which expansion and gasdrive occurs. For both matrix cells RC (a) and RC (b) match well and RC (c) overpredicts the speed of recovery. This means that in this case only the increment scaling option is significant and the scaling of $E_{R,max}$ is not. The start of oil resaturation in cell 7 is also exactly matched by RC (a) and RC (b). Because of the overprediction of the speed of oil recovery, oil resaturation starts earlier in case that the input RC is not scaled.

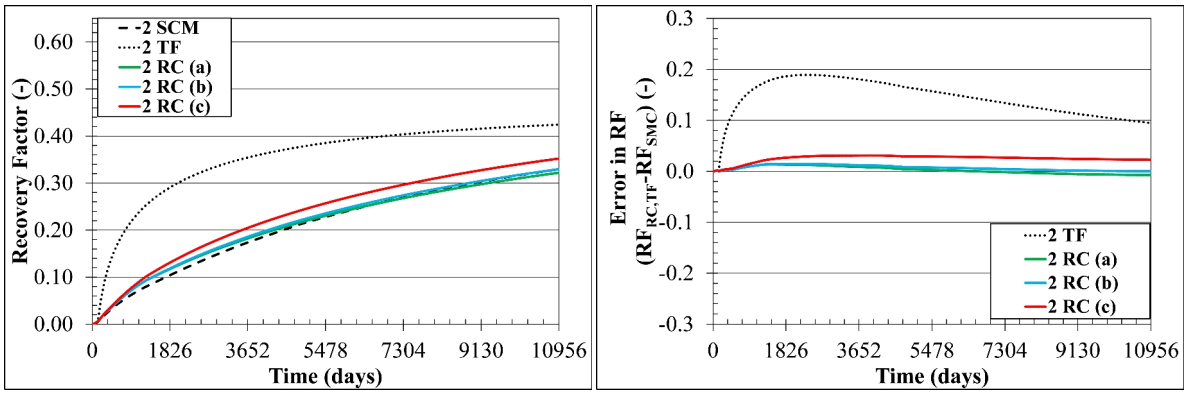

Figure 6.48: Setup 2: Recovery factor and error in recovery factor for cell 2

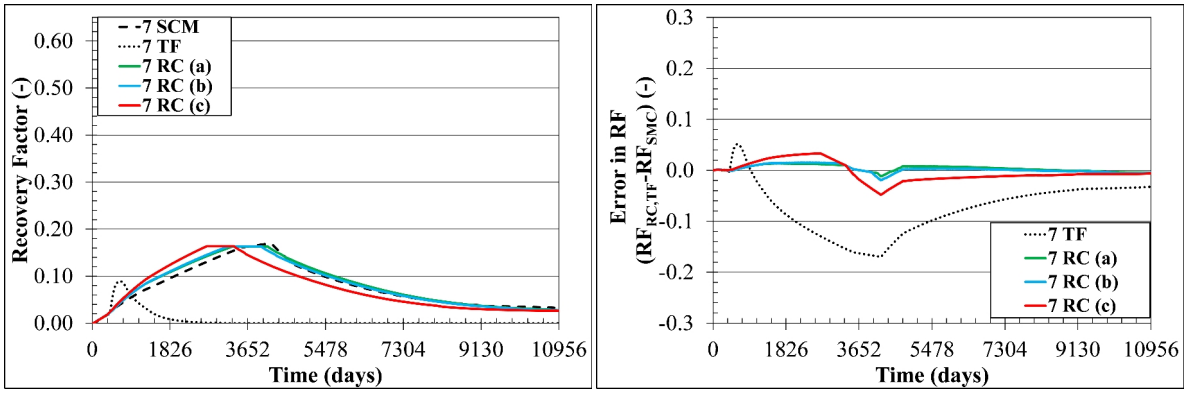

Figure 6.49: Setup 2: Recovery factor and error in recovery factor for cell 7, with oil resaturation.

Figure 6.50 shows the RCs (left) and error in recovery factor (right) for cell 10 of setup 3, in which expansion and waterdrive occurs. In this example RC (a) matches accurately, whereas both RC (b) and RC (c) are identical and underpredict the final recovery. In setup 3 the pressure drops below bubble point, which means that a scaling of the final recovery factor is necessary with regard to the change of $B_{o,}$ gravitational driving force and residual oil saturation. The residual oil saturation changes because of the presence of a critical gas saturation in the matrix. All of these factors are considered in RC (a), which therefore shows the best match.

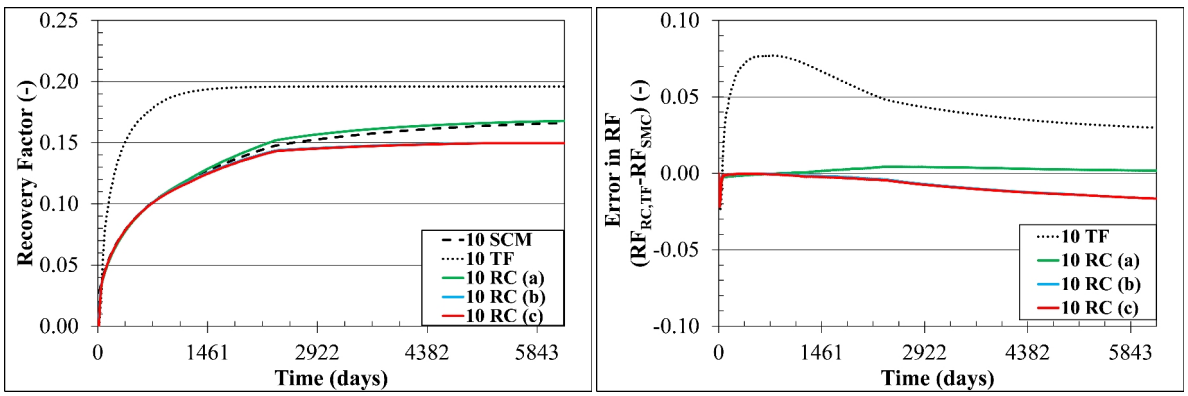

Figure 6.50: Setup 3: Recovery factor and error in recovery factor for cell 10.

Figure 6.51 shows the RCs (left) and error in recovery factor (right) for cell 10 of setup 4, in which waterdrive occurs. In this example the matrix is strongly water-wet. All RC scaling options give very similar result. In the error plot it can be seen that RC (a) and RC (b) have a slightly lower error, so increment scaling has a minor influence. An influence of $E_{R,max}$ scaling cannot be identified. The reason why also the result of the TF is very accurate in this instance is explained already in Section 6.5.

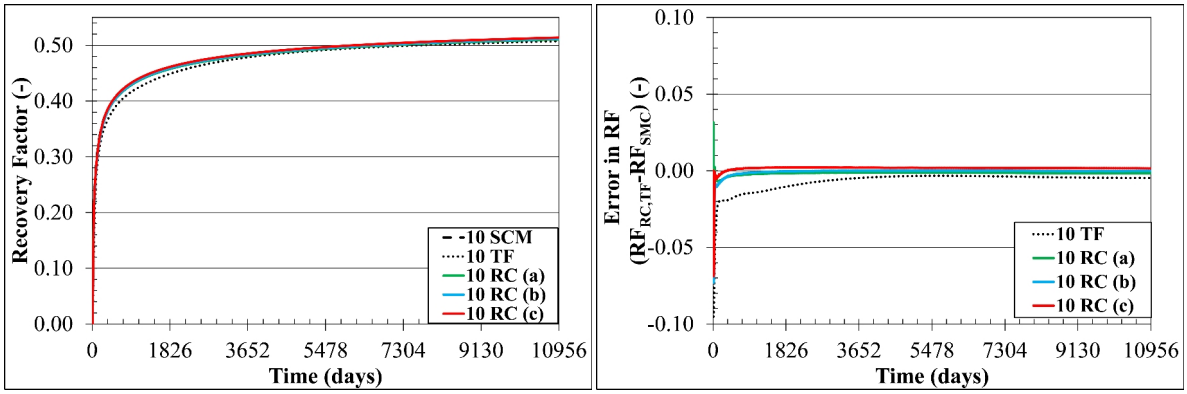

Figure 6.51: Setup 4: Recovery factor and error in recovery factor for cell 10.

Figure 6.52 shows the RCs (left) and error in recovery factor (right) for cell 3 of setup 5, in which expansion and gasdrive occurs. For this setup it can be seen that all three RC scaling options give different results. In the early time RC (a) and RC (c) are very similar but at RF values of about 0.23 also these curves separate. The lowest error occurs for RC (a), which means both increment and $E_{R,max}$ scaling are significant for setup 5.

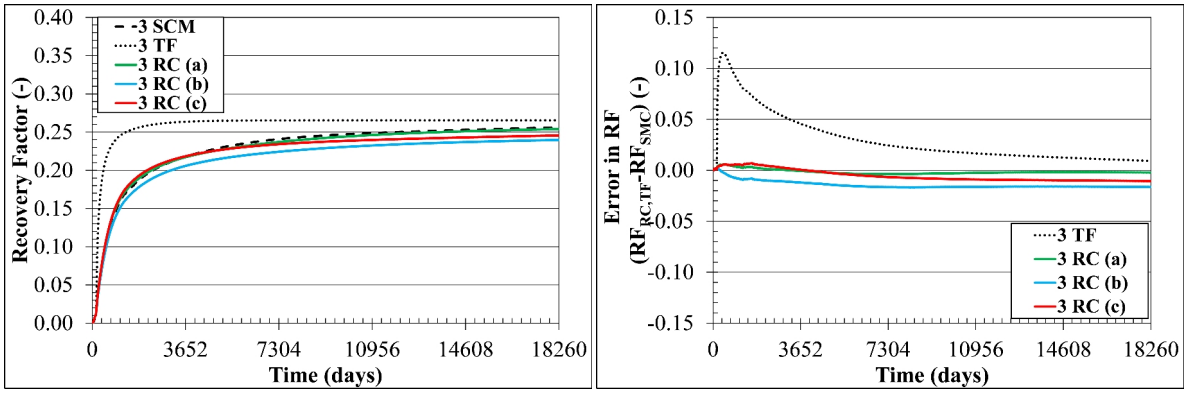

Figure 6.52: Setup 5: Recovery factor and error in recovery factor for cell 3.

Figure 6.53 and Figure 6.54 show the recovery factors (left) and the errors in recovery factor (right) for matrix cells 5 and 10 of setup 6, in which expansion and waterdrive occurs. In this setup the matrix is strongly water-wet and therefore also the TF gives a good estimate of $E_{R,max}$. All RC scaling options give a very low error, with RC (a) being the best fit. RC (b) and RC (c) are nearly identical, which means that the increment scaling option does not have an influence in this setup.

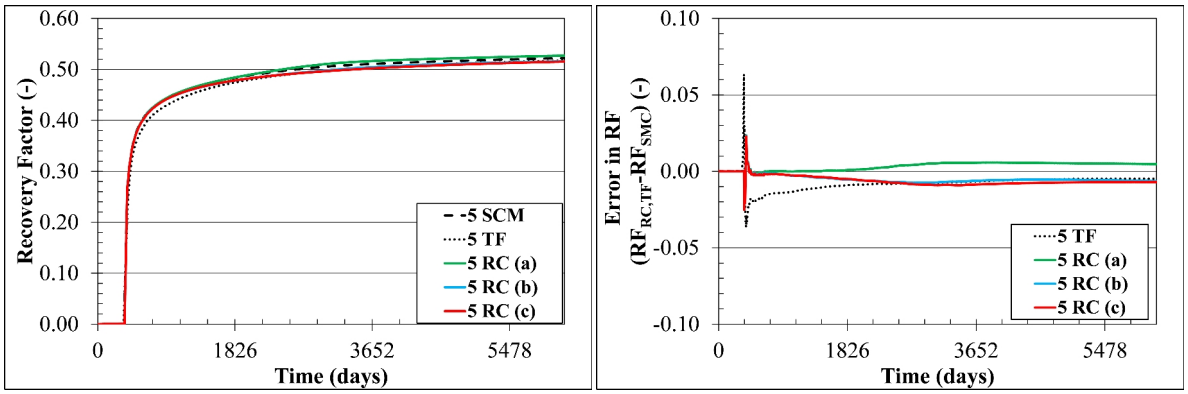

Figure 6.53: Setup 6: Recovery factor and error in recovery factor for cell 5.

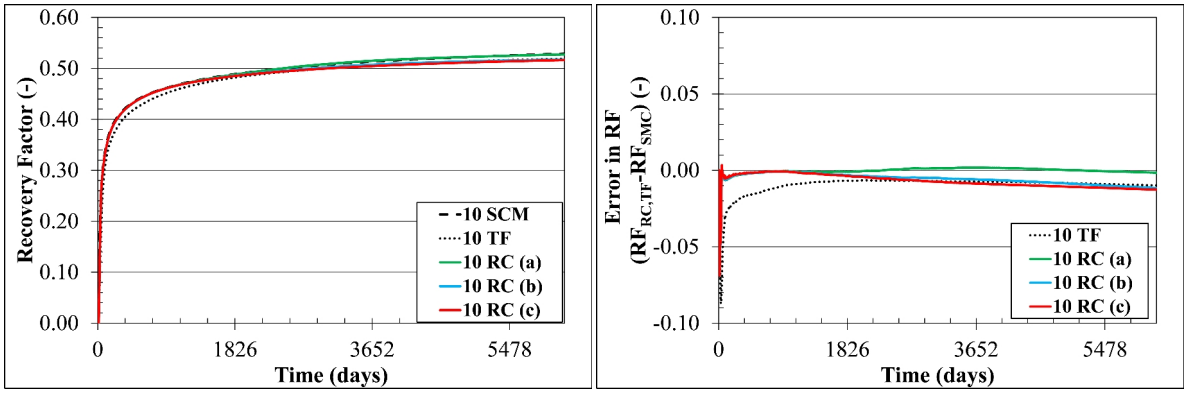

Figure 6.54: Setup 6: Recovery factor and error in recovery factor for cell 10.

6.7 Discussion

The RCM shows correct results for all setups, but the accuracy of the TF results depends strongly on the wettability of the rock and the drive mechanism. The TF cannot account for a non-uniform saturation distribution within the matrix block. The RCM has all this information already included in the input RC, because it was obtained with fine grid SMB calculation.

Setups 2 and 5 experience gravity drainage with gas filled fractures. Su et al. (2013) showed that if multiple matrix blocks in a column are immediately surrounded by gas filled fractures, most of the oil does not come out at the sides of the matrix blocks but moves vertically to the neighboring matrix block. The oil then enters the fracture at the gas oil contact. As this behavior is not modeled in conventional transfer function and also not in the RCM, this could lead to an overestimation of the oil recovery from matrix blocks within a single simulation cell. It should be noted that in the applied Warren-Root approach, all matrix blocks within a cell have the same fracture boundary condition. Also in strict dual-porosity formulation, flow between neighboring matrix cells is not allowed.

Chapter 7

Full Field Application

In this chapter the applicability of the herein presented RCM on a realistic full field model of a NFR is demonstrated. The influence of the RC scaling as well as a comparison between the RCM and a conventional TF matrix-fracture mass transfer model are presented. A realistic comparison of the transfer approaches can be done by operating the field model for a given production scenario and monitoring the phase contact movement within the reservoir and thereby checking the feasibility of the scenario. If all transfer models are applicable, they should produce the same phase contact movement for a specific production plan. If this is not the case, choosing a non-accurate transfer model would result in a non-optimized development plan.

The reservoir model, which was modified in some respects, is derived from a full field study that included a history match using a classical transfer function for the matrix-fracture mass transfer. This synthetic model still shows the same characteristics as the original one and is therefore suitable for demonstration of the RCM. The same model was also used by Brand, Mittermeir and Heinemann (2017) for the demonstration of a RC workflow, which utilizes a RCM without the herein presented scaling options.

The concept is to utilize the history matched real field case and treating it as a green field, where only the structure, the static reservoir parameters and the initial dynamic data are kept from original model. The real oil production rate is modified and taken as a target oil rate for the production scenario. This specific production plan is calculated using the before mentioned different matrix-fracture transfer models. The impact of the transfer models on the feasibility of the production scenario is then analyzed. This way it can be determined if all transfer approaches are equally suited for prediction or not.

7.1 Reservoir Model

The reservoir is a NFR, modeled as a dual porosity-dual permeability one. The structure of the reservoir and the position of the 44 introduced wells can be seen in Figure 7.1. The initial OWC is 945 m SS in average. The distance between this and the crest is 455 m.

The average permeability and porosity are listed in Table 7.1. The matrix porosity and permeability were modeled by stochastic simulation. The average permeability in lateral and vertical direction is equal but the variances of the permeability distributions are not. The minimum vertical permeability is 0.0 mD, whereas the minimum lateral permeability is 1 mD. A uniform facture porosity (ϕ=0.0045) and permeability (k_h=750 mD, k_v=100 mD) was assumed over the entire reservoir.

Table 7.1: Average permeability and porosity for matrix and fracture

	Unit	**Matrix (geostatistical distribution)**	**Fracture (uniform distribution)**
Average lateral permeability	mD	2.23	750
Average vertical permeability	mD	1.92	100
Average Porosity	-	0.17	0.0045

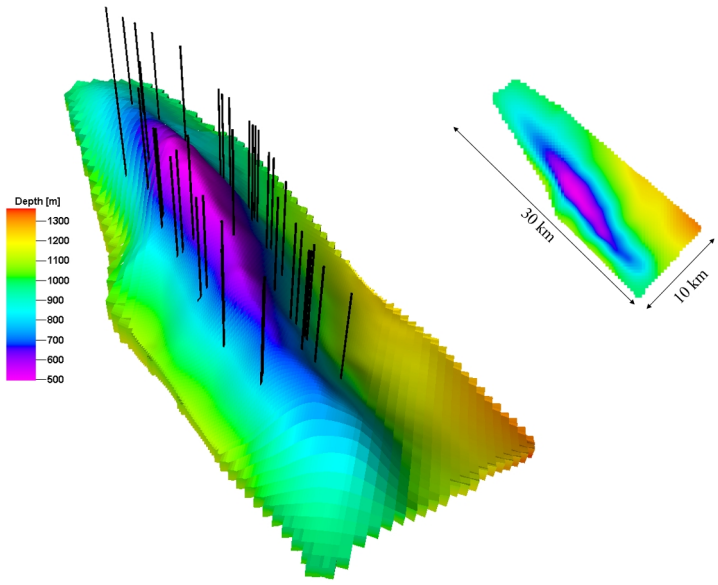

Figure 7.1: Top depth of the reservoir with proposed well locations

7.1.1 The Grid

The model has a refined grid to 100x100 m in x- and y-directions in the region where the wells are located. The resulting grid model is shown in Figure 7.2. The total number of grid cells is 140 x 167 x 14 = 327,320, from which 201,740 are active. The cell parameters resulted from upscaling of a geocellular model.

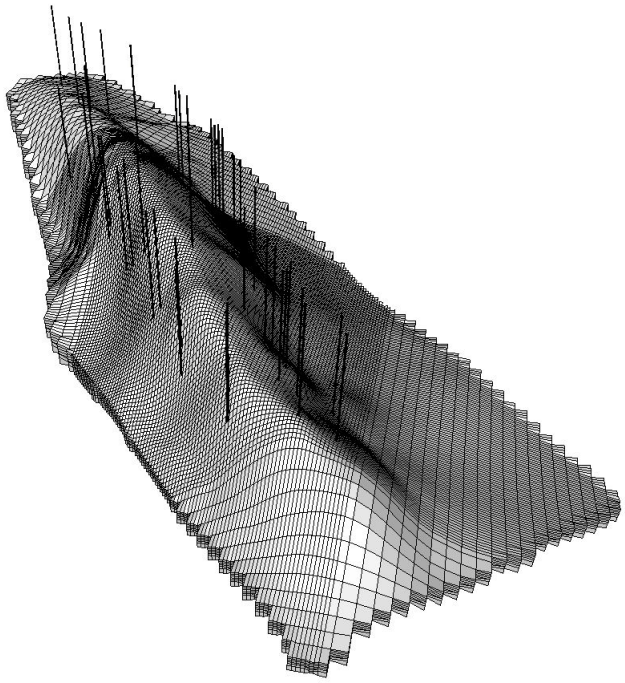

Figure 7.2: Simulation grid

7.1.2 PVT and SCAL Data

The reservoir is modeled with black-oil fluid description. PVT data set no.2, which was shown and described in Section 4.1 is used because of the similarity to the original PVT data of the full field model. The SCAL data set no. 1 of Section 6.2 is used for the matrix. This is data of an oil wet rock. The fracture is modeled with straight line relative permeability curves and zero capillary pressure. The model was initialized with drainage, the depletion with the imbibition capillary pressure function.

7.1.3 Initialization

The grid model was initialized assuming capillary-gravitational equilibrium. The water saturation in the matrix cells resulted from the drainage capillary function. Complete phase separation was assumed in the fracture, which means that above the OWC S_{wi}=0 and below that $S_{oi} = 0$.

7.1.4 Boundaries

The outer boundary is built by 4 segments, two in the North and two in the South, as shown in Figure 7.3.

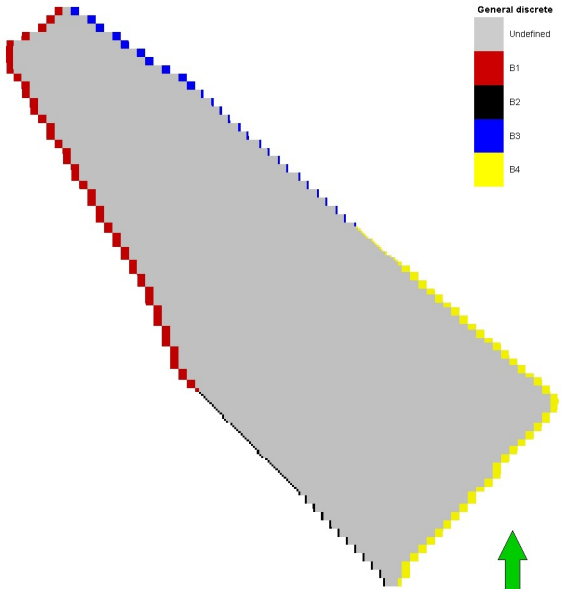

Figure 7.3: Model boundary definition

Fetkovich aquifer models with the following values are used for the parameters maximum encroachable water (W_{ei}) and aquifer productivity index J_w:

- B1: W_{ei} = 7.06602E+07 [rm3], J_w = 24.8 [(rm3/d)/bar]
- B2: W_{ei} = 8.07545E+07 [rm3], J_w = 24.8 [(rm3/d)/bar]
- B3: W_{ei} = 7.06602E+07 [rm3], J_w = 24.8 [(rm3/d)/bar]
- B4: W_{ei} = 8.07545E+07 [rm3], J_w = 24.8 [(rm3/d)/bar]

The parameters have been determined using the Target Pressure Method (TPM), which was already introduced by Pichelbauer (2003) and improved by Mittermeir, Pichelbauer and Heinemann (2004), based desired target pressures. The procedure of how to determine target pressure for the TPM is not be further discussed here, but could be found in the before mentioned publications or in Mittermeir et al. (2016).

7.1.5 Wells

44 wells are introduced into the reservoir and a target oil rate is assigned to them. The target reservoir oil production rate can be seen in Figure 7.4. It should be noted, that this is not the real field case oil production rate, but was modified. The distribution of the overall oil production to the wells is done according to the real field case. As more and more wells are drilled, the peak oil production is desired to occur approximately 18000 days after production start.

The location of the wells can be seen in Figure 7.1. When a GOR of 200 sm3/sm3 is reached, the worst offending perforation is squeezed. This is done to avoid and undesirable high gas production. The bottom hole flowing pressure is calculated using the Dupuit equation.

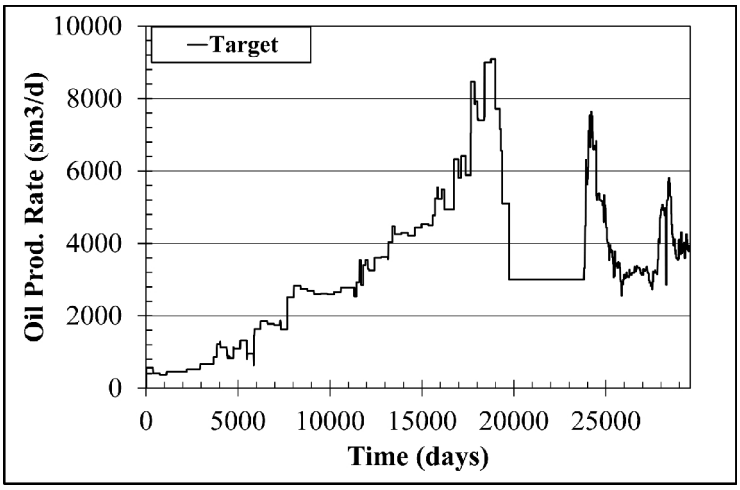

Figure 7.4: Target oil production rate

7.2 Matrix-Fracture Mass Transfer

To show the effect of the increment and endpoint scaling factors, which are described in Section 5.4, all setups are calculated using the RCM with

a.) $E_{R,max}$ and increment scaling: RC (a)
b.) no scaling: RC (b)

Additionally, the Kazemi et al. (1976) transfer function (TF) with the Gilman and Kazemi (1988) gravity drainage model is used for comparing it with the RCM results.

7.3 Results and Discussion

As shown in Figure 7.5 (left), the target field oil production rate cannot be achieved for the case RC (a), for the other two variants it is possible. When scaling of the RC is considered, not enough oil is available at the planned open perforations. This means, that to fulfill the production scenario, wells and/or perforations have to be moved or added. When the pressure dependence is neglected for the RCM, this issue would not be recognized. Similarly, also the TF shows not issue with achieving the target oil production rate.

The average HC-weighted reservoir pressure (Figure 7.5 right), is very similar for all

calculation options. This is not surprising, as the same aquifer model is used for all three cases and the overall cumulative produced reservoir volume differs only slightly.

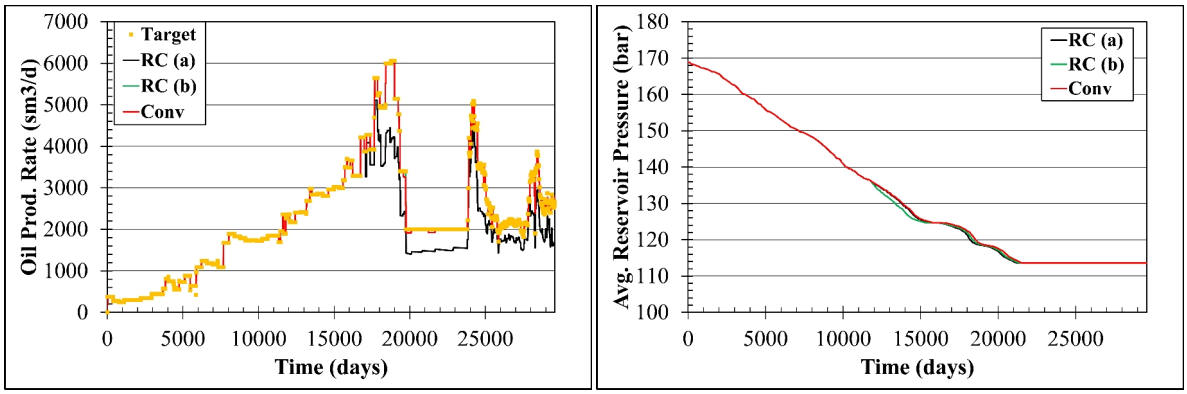

Figure 7.5: Oil production rate (left) and average reservoir pressure (right)

The field water production rate (Figure 7.6 left) exhibits an earlier massive increase for RC (a) compared to the other two scenarios. Starting approximately at day 25000 the water production rate is then lower for RC (a).

Naturally, the field water cut (Figure 7.6 right) shows a similar behavior as the water production rate. However, because the oil production rate is lower for setup RC (a), the water cut is higher relative to the other setups.

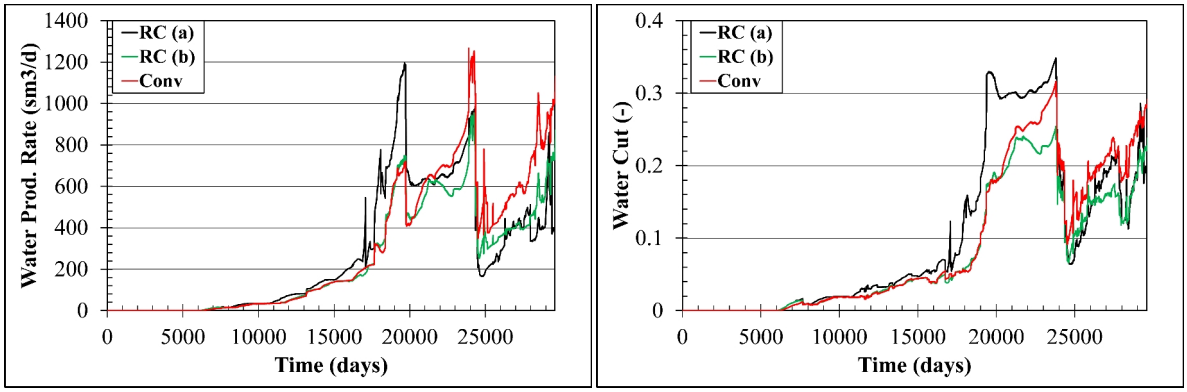

Figure 7.6: Water production rate (left) and water cut (right)

The field gas production rate (Figure 7.7 left) is similar for all setups, with the lowest gas production in RC (a). This is due to the oil production being lower and therefore the produced solution gas is less. This can be seen in Figure 7.7 (right), where the GOR is very similar for all setups. Gas breakthrough happens slightly earlier for RC (a), followed by RC (b). The TF predicts the latest gas breakthroughs at the wells. This causes the worst offending perforation to be squeezed at different times for all cases. At the end the GOR is constant, since no free gas is produced anymore and the solution gas ratio remains constant due to the constant pressure.

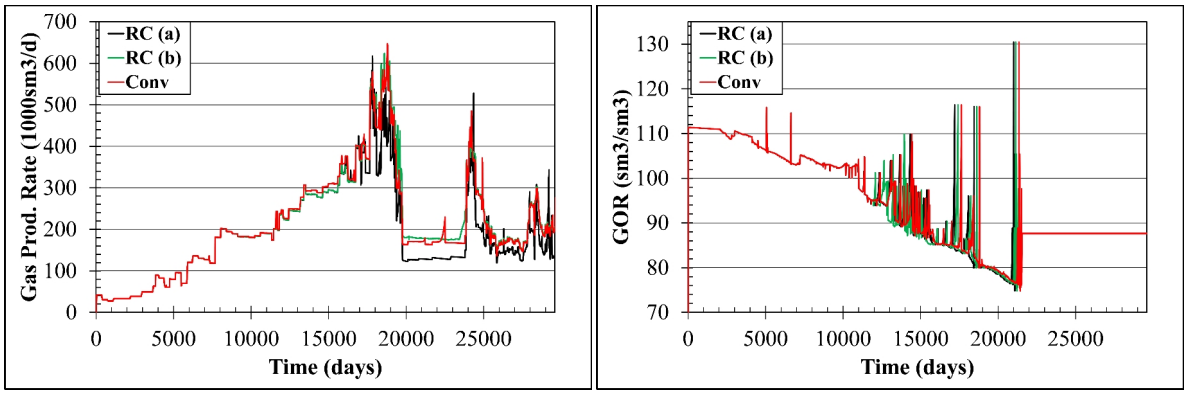

Figure 7.7: Gas production rate (left) and GOR (right)

The different results for the oil, gas and water production can be explained by the oil-water contact (OWC) (Figure 7.8 left) and oil-gas contact (OGC) (Figure 7.8 right) movement.

The OWC movement can be divided into four phases. The first phase lasts until day 8000 and for all models the contact movement is nearly identical. This can be explained by spontaneous imbibition and a dominance of the capillary driving force. The second phase then lasts roughly until day 18000, where a peak in the OWC can be observed. During this period for RC (a) the contact is advancing the fastest and for the TF the slowest. In this period already some matrix blocks are already nearly oil depleted and the balance between gravitational and capillary forces is important. This balance is best captured with the RCM and the speed of recovery and the ultimate recovery is also adjusted for RC (a). The TF overpredicts the oil recovery of the matrix blocks under water displacement. Phase three then lasts until day 24000, where the constant production ends. During this phase oil resaturation of previously water flooded zones occurs. RC (a) shows the strongest oil resaturation. This is due to the fact that for RC (a) more matrix blocks are already surrounded by water, due to the higher OWC. Therefore, many matrix cells transfer oil to the fracture continuum and cause a fast receding OWC. The TF exhibits no oil resaturation, as the phase contact remains constant is this period. This is because in the preceding phases the matrix recovery was overestimated. The fourth and last period shows a relatively parallel movement of the OWC for all transfer models. RC (a) again shows the steepest increase of the OWC in the beginning of the phase, as already previously water flooded zones are flooded again.

The OGC movement shows that both RC (b) and the TF overestimate the speed of oil recovery from the matrix through gas flooding. For both of these cases the OGC advances slower than for RC (a). This shows that for gasdrive, the scaling of the RC has a significant influence on the results.

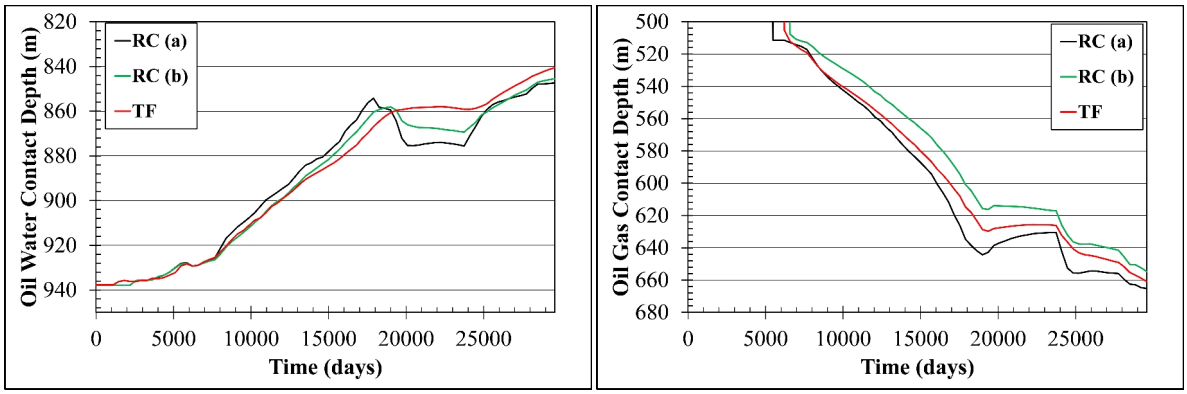

Figure 7.8: OWC (left) and GOC (right) movement

Chapter 8

Conclusion

The objective of this dissertation was the development of a generalized RCM for modeling the matrix-fracture mass transfer of naturally fractured petroleum reservoirs. For this also an assessment of the applicability of currently available methods based on TF was required. Therefore, in the following paragraphs the conclusions are split into the assessment of the available transfer functions, the verification of the herein presented RCM and the possibility of implementing this new method into a reservoir simulator and applying it to a full field model.

8.1 Applicability of available transfer functions

- Extensive literature review showed that no transfer equation is experimentally validated on a full scale matrix block, considering all potential drive mechanisms. Thus, as utilized in this work, fine grid SMB calculation is the best option for testing transfer models.

- Based on numerous numerical SMB calculations, it can be concluded that the KGE (1992) shape factor definition is applicable for single-phase expansion and solution gas drive as long as the matrix permeability is not extremely low. For permeabilities < 10^{-6} D the duration of the transient period becomes so long that it cannot be neglected. For higher permeabilities it can be seen that the transient period is very short and almost immediately a pseudo-steady state pressure regime is present, which is a requirement for using a constant shape factor.

- Generally, the transfer function with its constant shape factor is not applicable. It varies with time and for different recovery processes.

- The Reiss, Bossie-Codreanu and Lefebvre Du Prey (1973) approach is also shown to not be generally applicable. It may be deployed when the depletion of matrix blocks is strongly capillary dominated and other drive mechanisms or oil resaturation can be neglected. By matching the exponential function to early time behavior the later time cannot be reasonably described and vice versa. In the case of single phase expansion followed by solution gas drive neither an early nor late time match could be achieved,

therefore the exponential function cannot be used at all for this drive mechanisms.

8.2 Verification of the Recovery Curve Method

- The investigations on the dual porosity column model prove that the Recovery Curve Method (RCM), based on the concept of Heinemann (2004), gives more accurate results than the transfer function by Kazemi et al. (1976) using the Gilman and Kazemi (1988) gravity drainage model.
- The RCM is applicable to waterdrive and gasdrive for oil-wet and water-wet rock data. This was shown by the experiments using two types of rock data with different wettability. The error in the RF estimation when using the TF is strongly dependent on the rock-data used, the RCM is equally suitable for both used rock data sets.
- The most accurate results are gained by using both scaling of the increment, which was already shown by Gharsalla (2015) and Heinemann and Mittermeir (2016), and scaling of the estimated ultimate recovery factor.
- Oil resaturation curves can be used to model the re-imbibition of oil after waterdrive or gasdrive, as shown in setups 1, 2 and 5.
- Significant errors in the estimation of the ultimate recovery factor can occur especially for oil-wet rock data, where the balance between gravitational and capillary forces is strongly influenced by the non-uniformity of the saturation distribution within matrix blocks.
- The average pressure within a matrix block can be slightly lower than the one of the surrounding fracture. The difference between the pressures is exactly the capillary pressure for a given matrix saturation.

8.3 Applicability to Full Field Models

- The herein presented RCM is proven to be applicable on a full scale reservoir model.
- Scaling of the input RCs has a strong influence on the results for the calculated full field case. Optimizing of a production plan without considering the scaling of the RCs or even using a transfer equation would lead to a non-optimized production plan.
- Optimizing a Field Development Plan without utilizing a correct matrix-fracture mass transfer model can lead to unexpected water or gas breakthroughs at wells, potentially under- or overdimensioning well- and surface production equipment.

Chapter 9

References

Abushaikha, A.S. and Gosselin, O.R. 2008. Matrix-Fracture Transfer Function in Dual-Media Flow Simulation: Review, Comparison and Validation. Presented at the Europec/EAGE Conference and Exhibition, Rome, Italy, 9-12 June. SPE-113890-MS. https://doi.org/10.2118/113890-MS

Abushaikha, A.S. and Gosselin, O.R. 2009. SubFace Matrix-Fracture Transfer Function: Improved Model of Gravity Drainage/Imbibition. Presented at the EUROPEC/EAGE Conference and Exhibition, Amsterdam, The Netherlands, 8-11 June. SPE-121244-MS. https://doi.org/10.2118/121244-MS

Aguilera, R. 1980. Naturally Fractured Reservoirs, 2nd edition, Tulsa, Oklahoma, Usa: Penn Well Books

Amiry, M.T. 2014. *Modeling Flow Behavior in Naturally Fractured Reservoirs*. PhD Thesis, Montanuniversität Leoben, Leoben, Austria (February 2014)

Aronofsky, J.S., Masse, L., and Natanson, S.G. 1958. A Model for the Mechanism of Oil Recovery from the Porous Matrix Due to Water Invasion in Fractured Reservoirs. Trans. *AIME* **213**: 17-19. SPE-932-G

Barenblatt, G.I., Zheltov, I. P. and Kochina, I.N. 1960. Basic concepts on the theory of seepage of homogeneous liquids in fissured rocks. *Prikladnaya Matematika i Mekhanika* **24** (5): 852-864

Barker, J.A. 1985. Block-Geometry Functions Characterizing Transport in Densely Fissured Media. *Journal of Hydrology* **77** (1-4): 263-279. http://dx.doi.org/10.1016/0022-1694(85)90211-2

Bashiri, A. and Kasiri, N. 2011. Revisit Material Balance Equation for Naturally Fractured Reservoirs. Presented at the Nigeria Annual International Conference and Exhibition, Abuja, Nigeria, 30 July - 3 August. SPE-150803-MS. https://doi.org/10.2118/150803-MS

Bayon, Y.M., Cordelier, Ph.R. and Nectoux, A. 2002. A New Methodology To Match Heavy-Oil Long-Core Primary Depletion Experiments. Presented at the SPE/DOE Improved

Oil Recovery Symposium, Tulsa, Oklahoma, April 13-17. http://dx.doi.org/10.2118/75133-MS

Bourbiaux, B.J. and Kalaydijan, F.J. 1990. Experimental Study of Cocurrent and Countercurrent Flows in Natural Porous Media. *SPE Res Eng* **5** (3): 361-368. SPE-18283-PA. http://dx.doi.org/10.2118/18283-PA

Brand, J., Mittermeir, G.M. and Heinemann, G. 2017. A Recovery Curve Method Based Workflow for Reserves Estimation of Naturally Fractured Reservoirs - A Case Study. Presented at the SPE Abu Dhabi International Petroleum Exhibition & Conference, Abu Dhabi, UAE, 13-16 November. SPE-188418-MS. https://doi.org/10.2118/188418-MS

Chang, M.M. 1993. Deriving the shape factor of a fractured rock matrix. Technical Report NIPER-696, National Institute for Petroleum and Energy Research, Bartlesville, Oklahoma.

Coats, K.H. 1989. Implicit Compositional Simulation of Single-Porosity and Dual-Porosity Reservoirs. Presented at the SPE Symposium on Reservoir Simulation, Houston, Texas, 6-8 February. SPE-18427-MS. http://dx.doi.org/10.2118/18427-MS

Di Donato, G., Lu, H., Tavassoli, Z. and Blunt, M.J. 2007. Multirate-Transfer Dual-Porosity Modeling of Gravity Drainage and Imbibition. *SPE J.* **12** (1): 77-88. SPE-93144-PA. http://dx.doi.org/10.2118/93144-PA

Fu, Y., Yang, Y.-K. and Deo, M. 2005. Three-Dimensional, Three-Phase Discrete-Fracture Reservoir Simulator Based on Control Volume Finite Element (CVFE) Formulation. Presented at the SPE Reservoir Simulation Symposium, The Woodlands, Texas, 31 Jan -2 Feb. SPE-93282-MS. https://doi.org/10.2118/93292-MS

Geiger, S., Huangfu, Q., Reid, F., Matthai, S.K., Coumou, D., Belayneh, M., Fricke, C. and Schmid, K.S. 2009. Massively Parallel Sector Scale Discrete Fracture and Matrix Simulations. Presented at the SPE Reservoir Simulation Symposium, The Woodlands, Texas, 2-4 February. SPE-118924-MS. https://doi.org/10.2118/118924-MS

Gerke, H.H. and van Genuchten, M.Th. 1996. Macroscopic Representation of Structural Geometry for Simulating Water and Solute Movement in Dual-Porosity Media. *Advances in Water Resources* **19** (6): 343-357. http://dx.doi.org/10.1016/0309-1708(96)00012-7

Ghaedi, M., Masihi, M., Heinemann, Z.E. and Ghazanfari, M.H. 2014. Evaluation and Uncertainty Quantification of Matrix-Fracture Interaction by History Matching. Presented at the 8th International Chemical Engineering Congress & Exhibition, Kish, Iran, 24-27 February.

Ghaedi, M., Masihi, M., Heinemann, Z.E. and Ghazanfari, M.H. 2015. Application of the Recovery Curve Method for evaluation of matrix-fracture interactions. *Journal of Natural Gas Science and Engineering* **22**: 447-458. https://doi.org/10.1016/j.jngse.2014.12.029

Gharsalla M.M. 2015. *Application of the Recovery Curve Method to Petroleum Reservoir Material Balance*. PhD Thesis, Montanuniversität Leoben, Leoben, Austria (April 2014).

Gilman, J.R. and Kazemi, H. 1983. Improvements in Simulation of Naturally Fractured Reservoirs. *SPE J.* **23** (4): 695-707. SPE-10511-PA. https://doi.org/10.2118/10511-PA

Gilman, J.R. 2003. Practical Aspects of Simulation of Fractured Reservoirs. Presented at the Seventh International Forum on Reservoir Simulation, Baden-Baden, Germany, 23-27 June

Gilman, J.R. and Kazemi, H. 1988. Improved Calculations for Viscous and Gravity Displacement in Matrix Blocks in Dual-Porosity Simulators. *Journal of Petroleum Technology* **40** (1): 60-60. SPE-16010-PA. https://doi.org/10.2118/16010-PA

Hamon, G. and Vidal, J. 1986. Scaling-Up the Capillary Imbibition Process From Laboratory Experiments on Homogeneous and Heterogeneous Samples. Presented at the European Petroleum Conference, London, United Kingdom, October 20-2. http://dx.doi.org/10.2118/15852-MS

Hassler, G.L. and Brunner, E. 1945. Measurement of Capillary Pressures in Small Core Samples. *Trans. AIME* **160** (1): 114-123. SPE-945114-G. http://dx.doi.org/10.2118/945114-G

Heinemann, Z.E. 2004. *Using Recovery Curves in Modeling Natural Fractured Hydrocarbon Reservoirs*. Proposal for a PhD Research Project at the Montanuniversität Leoben, Austria (March 2004)

Heinemann, Z. E. and Mittermeir, G. M. 2012. Derivation of the Kazemi-Gilman-Elsharkawy Generalized Dual Porosity Shape Factor. *Transport in Porous Media* **91** (1): 123-132. http://dx.doi.org/10.1007/s11242-011-9836-4

Heinemann, Z.E. and Mittermeir, G.M. 2014. Naturally Fractured Reservoir Engineering, PHDG Textbook, Volume 5.

Heinemann, Z.E. 2015. Naturally Fractured Reservoirs (Lecture PowerPoint Slides)

Heinemann, Z.E. and Mittermeir, G.M. 2016. Generally Applicable Method For Calculation Of The Matrix-fracture Fluid Transfer Rates. Presented at the SPE Europec, Vienna, Austria, 30 May - 2 June. SPE-180121-MS. http://dx.doi.org/10.2118/180121-MS

Hirasaki, G.J. 1980. Scaling Of Non-Equilibrium Phenomena In Surfactant Flooding. Presented at the SPE/DOE Enhanced Oil Recovery Symposium, Tulsa, Oklahoma, 20-23 April. SPE-8841-MS. http://dx.doi.org/10.2118/8841-MS

Hoteit, H. and Firoozabadi, A. 2004. Compositional Modeling of Fractured Reservoirs Without Transfer Functions by the Discontinuous Galerkin and Mixed Methods. *SPE J.* **11** (3): 341-352. SPE-90277-PA. https://doi.org/10.2118/90277-PA

Karimi-Fard, M., Durlofsky, L.J. and Aziz, K. 2004. An Efficient Discrete-Fracture Model Applicable for General- Reservoir Simulators. *SPE J.* **9** (2): 227-236. SPE-88812-PA. https://doi.org/10.2118/88812-PA

Karimi-Fard, M. and Firoozabadi, A. 2003. Numerical Simulation of Water Injection in Fractured Media using the Discrete-Fractured Model and the Galerkin Method. *SPE Res Eval & Eng* **6** (2): 117-126. SPE-83633-PA. https://doi.org/10.2118/83633-PA

Kazemi, H., Merrill, L.S., Porterfield, K.L. and Zeman, P.R. 1976. Numerical Simulation of Water-Oil Flow in Naturally Fractured Reservoirs. *SPE J.* **16** (6): 317-326. SPE-5719-PA. http://dx.doi.org/10.2118/5719-PA

Kazemi, H. and Merrill, L.S. 1979. Numerical Simulation of Water Imbibition in Fractured Cores. *SPE J.* **19** (3): 175-182. SPE-6895-PA. http://dx.doi.org/10.2118/6895-PA

Kazemi, H., Gilman, J.R. and Elsharkawy, A.M. 1992. Analytical and Numerical Solution of Oil Recovery from Fractured Reservoirs Using Empirical Transfer Functions. *SPE Res Eng* **7** (2): 219-227. SPE-19849-PA. http://dx.doi.org/10.2118/19849-PA

Kazemi, H. and Gilman, J. R. 1993. *Multiphase Flow in Fractured Petroleum Reservoirs*. In Flow and Contaminant Transport in Fractured Rock, Edited by J. Bear, CF. Tsang, and G. de Marsily, Chapter 6, 267-323. San Diego, CA: Academic Press

Kleppe, J. and Morse, R.A. 1974. Oil Production from Fractured Reservoirs by Water Displacement. Presented at the 49th Annual Fall Meeting of the SPE-AIME, Houston, Texas, October 6-9. SPE-5084-MS. http://dx.doi.org/10.2118/5084-MS

Kyte, J.R. 1970. A Centrifuge Method To Predict Matrix-Block Recovery in Fractured Reservoirs. *SPE J.* **10** (2): 165-170. SPE-2729-PA. http://dx.doi.org/10.2118/2729-PA

Le Guen, S.S. and Kovscek, A.R. 2006. Nonequilibrium Effects During Spontaneous Imbibition. *Transport in Porous Media* **63** (1): 127-146. http://dx.doi.org/doi:10.1007/s11242-005-3327-4

Lewandowska, J., Szymkiewicz, A., Burzynski, K. and Vauclin, M. 2004. Modeling of unsaturated water flow in double-porosity soil by the homogenization approach. *Adv. Water Res.* **27**, 283–296. http://dx.doi.org/10.1016/j.advwatres.2003.12.004

Li, H., Putra, E., Schechter, D.S. and Grigg, R.B. 2000. Experimental Investigation of CO2 Gravity Drainage in a Fractured System. Presented at the SPE Asia Pacific Oil and Gas Conference and Exhibition, Brisbane, Australia, 16-18 October. SPE-64510-MS. http://dx.doi.org/10.2118/64510-MS

Li, L. and Lee, S.H. 2008. Efficient Field-Scale Simulation of Black Oil in a Naturally Fractured Reservoir Through Discrete Fracture Networks and Homogenized Media. *SPE Res Eval & Eng* **11** (4): 750-758. SPE-103901-PA. https://doi.org/10.2118/103901-PA

Lim, K.T. and Aziz, K. 1995. Matrix-fracture transfer shape factors for dual-porosity simulators. *Journal of Petroleum Science and Engineering* **13** (3-4): 169-178. http://dx.doi.org/10.1016/0920-4105(95)00010-F

Mattax, C.C. and Kyte, J.R. 1962. Imbibition Oil Recovery from Fractured, Water-Drive

Reservoirs. *SPE J.* **2** (2): 177-84 SPE-187-PA. http://dx.doi.org/10.2118/187-PA

McNaughton, D.A. and Garb, F.A. 1975. Finding and Evaluating Petroleum Accumulations in Fractured Reservoir Rock, Volume 13: Matthew Bender & Company

Mittermeir, G.M., Pichelbauer, J. and Heinemann, Z.E. 2004. Automated Determination of Aquifer properties from Field Production Data. Presented at the 9th European Conference on Mathematics of Oil recovery, Cannes, France, 30 August - 2 September.

Mittermeir, G.M. 2006. *Performance Prediction of Naturally Fractured Reservoirs Using Simulation Models on Different Scales*. PhD Thesis, Montanuniversität Leoben, Leoben, Austria (March 2006)

Mittermeir, G.M. 2015. Material-Balance Method for Dual-Porosity Reservoirs With Recovery Curves to Model the Matrix/Fracture Transfer. *SPE Res Eval & Eng* **18** (2): 171-186. SPE-174082-PA. http://dx.doi.org/10.2118/174082-PA

Mittermeir, G.M., Steiner, C. Gharsalla, M.M. and Heinemann, Z.E. 2016. Verification of Geological Models With One Single Simulation Run. Presented at the SPE Europec featured at 78th EAGE Conference and Exhibition, Vienna, Austria, 30 May-2 June. SPE-180122-MS. https://doi.org/10.2118/180122-MS

Moinfar, A. Varavei, A., Sepehrnoori, K. and Johns, R.T. 2014. Development of an Efficient Embedded Discrete Fracture Model for 3D Compositional Reservoir Simulation in Fractured Reservoirs. *SPE J.* **19** (2): 289-303. SPE-154246-PA. https://doi.org/10.2118/154246-PA

Morel, D.C., Lomer, J-F., Morineau, Y.M. and Putz, A.G. 1992. Mobility of Hydrocarbon Liquids in Gas Condensate Reservoirs: Interpretation of Depletion Laboratory Experiments. Presented at the SPE Annual Technical Conference and Exhibition, Washington, D.C., 4-7 October. SPE-24939-MS. http://dx.doi.org/10.2118/24939-MS

Morrow, N.R., Ma, S., Zhou, X. and Zhang, X. 1994. Characterization of Wettability From Spontaneous Imbibition Measurements. Presented at the Annual Technical Meeting, Calgary, Alberta, June 12 - 15. PETSOC-94-47. http://dx.doi.org/10.2118/94-47

Naimi-Tajdar, R., Sepehrnoori, K. and Delshad, M. 2007. Matrix Subgridding and Its Effects in Dual Porosity Simulators. Presented at the International Petroleum Technology Conference, Dubai, U.A.E., 4-6 December. IPTC-11195-MS. https://doi.org/10.2523/IPTC-11195-MS

Nelson, R.A. 1992. An Approach to Evaluating Fractured Reservoirs. *J Pet Technol* **34** (9): 2167-2170. SPE-10331-PA. https://doi.org/10.2118/10331-PA

Penuela, G., Idrobo, E.A., Ordonez, A., Medina, C.E. and Meza, N.S. 2001. A New Material-Balance Equation for Naturally Fractured Reservoirs Using a Dual-System Approach. Presented at the SPE Western Regional Meeting, Bakersfield, California, 26-30 March. SPE-68831-MS. https://doi.org/10.2118/68831-MS

Pichelbauer, J. 2003. A new method of aquifer matching in reservoir simulation. Dissertation,

Montanuniversität Leoben, Leoben, Austria (March 2003)

Pirker, B. 2008. *A New Approach For Modeling Dual Porosity Reservoirs Using Recovery Curves.* PhD Thesis, Montanuniversität Leoben, Leoben, Austria (November 2008)

Pooladi-Darvish, M. and Firoozabadi, A. 2000. Experiments and Modelling of Water Injection in Water-wet Fractured Porous Media. *J Can Pet Technol* **39** (3): 31 - 42. http://dx.doi.org/10.2118/98-55

Pruess K. and Narasimhan T.N. 1985. A Practical Method for Modeling Fluid and Heat Flow in Fractured Porous Media. *SPE J.* **25** (1): 14-26. SPE-10509-PA. http://dx.doi.org/10.2118/10509-PA

Quandalle, P. and Sabathier, J.C. 1989. Typical Features of a Multi Reservoir Simulator. *SPE Res Eng* **4** (4): 475-480. SPE-16007-PA. https://doi.org/10.2118/16007-PA

Rangel-German, E.R. and Kovscek, A.R. 2000. Matrix-Fracture Interaction In Single Matrix Blocks. Proceedings of the Twenty-Fifth Workshop on Geothermal Reservoir Engineering Stanford University, Stanford, California, 24-26 January

Rangel-German, E.R. and Kovscek, A.R. 2002. Experimental and analytical study of multidimensional imbibition in fracture porous media. *Journal of Petroleum Science and Engineering* **36** (1-2): 45-60. http://dx.doi.org/10.1016/S0920-4105(02)00250-4

Rangel-German E.R. and Kovscek A.R. 2003. Time-Dependent Matrix-Fracture Shape Factors for Partially and Completely Immersed Fractures. Presented at the SPE ATCE, Denver, Colorado, USA, 5-8 Oct. SPE-84411-MS. http://dx.doi.org/10.2118/84411-MS

Reiss L.H., Bossie Codreanu D. and Lefebvre du Prey E.J. 1973. Flow in Fissured Reservoirs. Presented at the SPE European Meeting, London, UK, 2-3 April. SPE-4343-MS. https://doi.org/10.2118/4343-MS

Sahni, A., Gadelle, F., Kumar, M., Kovscek, A.R. and Tomutsa, L. 2001. Experiments and Analysis of Heavy Oil Solution Gas Drive. Presented at the SPE Annual Technical Conference and Exhibition, New Orleans, Louisiana, 30 September-3 October. SPE-71498-MS. http://dx.doi.org/10.2118/71498-MS

Saidi, A.M. 1983. Simulation of Naturally Fractured Reservoirs. Presented at the SPE Reservoir Simulation Symposium, San Francisco, California, 15-18 November. SPE-12270-MS. https://doi.org/10.2118/12270-MS

Sandoval Merchan, P.A., Calderon Carillo, Z.H. and Ordonez, A. 2009. The New, Generalized Material Balance Equation for Naturally Fractured Reservoirs. Presented at the Latin American and Caribbean Petroleum Engineering Conference, Cartagena de Indias, Colombia, 31 May-3 June. SPE-122395-MS.https://doi.org/10.2118/122395-MS

Steiner, C. and Mittermeir, G.M. 2017. Applicability of the shape-factor concept for naturally fractured reservoirs and an alternative approach. *Journal of Petroleum Science and*

Engineering **154**: 60-75. https://doi.org/10.1016/j.petrol.2017.04.009

Su, S., Gosselin, O.R., Parvizi, H. and Giddins, M.A. Dynamic Matrix-Fracture Transfer Behavior in Dual-Porosity Models. Presented at the EAGE Annual Conference & Exhibition incorporating SPE Europec, London, UK, 10-13 June. SPE-164855-MS. https://doi.org/10.2118/164855-MS

Tarner, J. 1944. How Different Size Gas Caps and Pressure Maintenance Programs Affect Amount of Recoverable Oil. *Oil Weekly* **144** (June 12): 32-34

Thomas L.K., Dixon T.N. and Pierson R.G. 1983. Fractured Reservoir Simulation. *SPE J.* **23** (1): 42-54. SPE-9305-PA. http://dx.doi.org/10.2118/9305-PA

Ueda, Y., Murata, S., Watanabe, Y. and Funatsu, K. 1989. Investigation of the Shape Factor Used in the Dual-Porosity Reservoir Simulator. Presented at the SPE Asia-Pacific Conference, Sydney, Australia, 13-15 September. SPE 19469-MS. http://dx.doi.org/10.2118/SPE-19469-MS

Warren, J.E. and Root, P.J. 1963. The Behavior of Naturally Fractured Reservoirs. *SPE J.* **3** (3): 245-255. SPE-426-PA. http://dx.doi.org/10.2118/426-PA

Wu, Y.S. and Pruess, K. 1988. A Multiple-Porosity Method for Simulation of Naturally Fractured Petroleum Reservoirs. *SPE Res Eng* **3** (1): 327-336. SPE-15129-PA. https://doi.org/10.2118/15129-PA

Zhang, X., Morrow, N.R. and Ma, S. 1996. Experimental Verification of a Modified Scaling Group for Spontaneous Imbibition. *SPE Res Eng* **11** (4): 280-285. SPE-30762-PA. http://dx.doi.org/10.2118/30762-PA

Zhoue, X., Morrow, N.R., Ma, S. 2000. Interrelationship of Wettability, Initial Water Saturation, Aging Time, and Oil Recovery by Spontaneous Imbibition and Waterflooding. *SPE J.* **5** (2): 199-207. SPE-62507-PA. http://dx.doi.org/10.2118/62507-PA

Zimmerman, R.W., Chen, G., Hadgu, T. and Bodvarsson, G.S. 1993. A numerical dual-porosity model with semianalytical treatment of fracture/matrix flow. *Water Resources Research* **29** (7): 2127-2137. http://dx.doi.org/10.1029/93WR00749

Chapter 10

Nomenclature and Abbreviations

Symbols

A	-	area, [m²]
B	-	formation volume factor, [-]
B_{cmf}	-	matrix-fracture mass transfer from recovery curve, [kmol/day]
d	-	distance, [m]
D	-	specific mole density, [kmol/m³]
E_R	-	recovery efficiency/factor, [-]
k	-	permeability, [mD]
L	-	length, [m]
m	-	gas cap factor, [-]
$\vec{n}$	-	unit normal vector, [-]
N	-	original oil in place, [sm³]
N	-	number of fracture sets, [-]
N_P	-	cumulative oil production, [sm³]
$OOIP$	-	Original Oil In Place, [kmol]]
P_c	-	capillary pressure, [bar]
P_h	-	gravitational head pressure, [bar]
p	-	pressure, [bar]
q	-	flow rate, [m³/day]
q_p^{mf}	-	matrix fracture mass transfer term, [kg/s/m³]
q_{cmf}	-	matrix fracture mass transfer for component c, [m³/s]
R_s	-	solution gas-oil ratio, [sm³/sm³]
S	-	phase saturation, [-]
t	-	time [days]
$\vec{u}$	-	filtration velocity, [m/day]
V	-	volume, [m³]
W_e	-	cumulative water encroachment, [sm³]
W_P	-	cumulative water production, [sm³]
x_{pc}	-	mole fraction of component c in phase p, [-]

Greek Symbols

α	-	recovery curve scaling factor, [-]
β–	time-scaling factor, [-]	
δ_{mf}	-	matrix-fracture transmissivity, [m³]
λ	-	correlation factor, [-]
λ	-	mobility, [1/cp]
μ	-	viscosity, [cp]
ρ	-	density, [kg/m³]
σ	-	shape factor, [1/m2]
ϕ	–	porosity, [-]
Φ	-	potential, [bar]
δ_{mf}	-	matrix-fracture transmissivity, [m³]
τ_{mf}	-	matrix-fracture transmissibility, [m³]

Subscripts

a	-	absolute
adj	-	adjusted
b	-	bubblepoint/ reference condition for recovery curve
c	-	component
eff	-	effective
f	-	fracture
g	-	gas
h	-	horizontal
i	-	initial conditions
k	-	grid cell index no.
m	-	matrix
max	-	maximum/ultimate
o	-	oil
p	-	phase
r	-	relative
t	-	total
v	-	virtual
v	-	vertical
w	-	water
x,y,z	-	coordinate directions

Superscripts

fm	-	fracture-to-matrix (direction)
g	-	gas recovery curve
mf	-	matrix-to-fracture (direction)
n	-	old time level
n+1	-	new time level
o	-	oil resaturation curve
p	-	phase of recovery curve

r - residual
w - water recovery curve

Abbreviations

DFM - Discrete Fractured Models
DFN - Discrete Fracture Network
DCM - Dual Continuum Modeling
EDFM- Embedded Discrete Fracture Modeling
GOC - Gas Oil Contact
GOR - Gas Oil Ratio
KGE - Kazemi, Gilman and Elsharkawy
MB - Material Balance
MINC - Multiple Interacting Continua
NFR - Naturally Fractured Reservoir
OOIP - Original Oil In Place
OWC - Oil Water Contact
PVT - Pressure-Volume-Temperature
RC - Recovery Curve
RCM - Recovery Curve Method
RF - Recovery Factor
SCAL - Special Core Analysis
SCM - Single Continuum Model
SF - Shape Factor
SMB - Single Matrix Block
TF - Transfer Function